Escola de Camins
Escola Tècnica Superior d'Enginyeria de Camins, Canals i Ports
UPC BARCELONATECH

TREBALL FINAL DE MÀSTER

A continuous-discontinuous model to simulate crack branching in quasi-brittle failure

Treball realitzat per:
Jordi Feliu Fabà

Dirigit per:
Antonio Rodríguez Ferran

Màster en:
Enginyeria de Camins, Canals i Ports

Barcelona, 22 de juny de 2016

Departament d'Enginyeria Civil i Ambiental

Abstract

A continuous-discontinuous model to simulate crack branching in quasi-brittle failure

Jordi Feliu-Fabà

Branched cracks in quasi-brittle failure are present in materials used in civil engineering, such as rocks and concrete. For instance, crack branching is a common phenomenon in dynamic crack propagation. Here, a continuous-discontinuous strategy for quasi-static simulation of crack branching in quasi-brittle materials is presented.

Traditionally, two different approaches have been used for the numerical simulation of quasi-brittle failure: damage mechanics and fracture mechanics. In damage mechanics, degradation is described by an internal variable —damage, D— that produces local modifications to the stiffness, accounting for strain softening. Damage growth is described by means of continuous models. In contrast, fracture mechanics explicitly introduces a crack by means of discontinuous models that allow to obtain a discontinuous displacement field.

In this work a continuous-discontinuous approach, which merges both theories, is used. Damage inception and evolution is described by a non-local continuous model, which regularises softening and controls strain localisation. Once the damage field reaches a critical damage value the discontinuous model is activated and a crack is introduced by means of the eXtended Finite Element Method (X-FEM). Then the non-local continuous model is coupled with the discontinuous model to capture damage evolution and crack propagation.

The goal of this thesis is to extend the continuous-discontinuous formulation for crack propagation to crack branching. Our main concern is to (a) find the appropriate nodal enrichment by means of X-FEM that allows to simulate crack branching and (b) include this enrichment in a continuous-discontinuous model such as the one described above.

First, we propose an alternative nodal enrichment by means of the X-FEM to represent displacement discontinuities in a branched crack. We illustrate the capabilities of this new enrichment by carrying out several two-dimensional elastic numerical tests.

Second, we present the continuous-discontinuous approach used for simulating the whole quasi-brittle failure process. Of relevance is the extension of this approach to account for crack branching.

Last, the capabilities of the X-FEM enrichment and the continuous-discontinuous approach for simulations of branched cracks in quasi-brittle failure are illustrated with a numerical example that includes crack branching.

Keywords: continuous-discontinuous simulation, crack branching, enrichment, eXtended Finite Element Method (X-FEM), quasi-brittle failure.

Acknowledgments

First of all, I would like to express my sincere gratitude to my thesis advisor Prof. Antonio Rodríguez Ferran. Thank you for your time spent, your guidance and your insightful comments. You have made me enjoy doing research and you have encouraged me to start my path into research.

I would also like to acknowledge Dr. Elena Tamayo Mas, for solving any doubts arised during this project and sharing part of her PhD MATLAB code needed to carry out this thesis.

Finally, I would like to thank my friends at UPC and my flatmates, who have been part of this six unforgettable years at Barcelona. Special thanks to my family and Ana, for their tireless encouragement.

Contents

List of figures

List of tables

List of symbols

Latin symbols

$\mathbf{A}_{\text{equi}}$	Constraint matrix for the mechanical problem
$\mathbf{A}_{\text{reg}}$	Constraint matrix for the regularisation problem
$\mathbf{B}$	Derivative shape function matrix
$\boldsymbol{C}$	Elastic stiffness tensor
$\mathbf{D}$	Diffusivity matrix
$\mathbf{D}_{\psi_p}$	Enriched diffusivity matrix for the principal crack
$\mathbf{D}_{\psi_s}$	Enriched diffusivity matrix for the secondary crack
$\mathbf{D}_{\psi_b}$	Enriched diffusivity matrix for the coupling of both cracks
D	Scalar damage parameter
D^*	Isovalue of damage (for the medial axis computation)
D_{crit}	Critical damage value
E	Young's modulus
$\mathbf{K}_{\text{BC}}$	Combined boundary conditions matrix
$\mathbf{K}_{\psi_p,\text{BC}}$	Enriched combined boundary conditions matrix for the principal crack
$\mathbf{K}_{\psi_s,\text{BC}}$	Enriched combined boundary conditions matrix for the secondary crack
$\mathbf{K}_{\psi_b,\text{BC}}$	Enriched combined boundary conditions matrix for the coupling of both cracks
$\mathbf{K}_{\text{cohesion}}$	Cohesive matrix
$\mathbf{K}_{\text{loc}}$	Local tangent matrix
$\mathbf{K}_{\psi_p,\text{loc}}$	Enriched local tangent matrix for the principal crack
$\mathbf{K}_{\psi_s,\text{loc}}$	Enriched local tangent matrix for the secondary crack
$\mathbf{K}_{\psi_b,\text{loc}}$	Enriched local tangent matrix for the coupling of both cracks
$\mathbf{K}_{\text{sec}}$	Secant tangent matrix
$\mathbf{K}_{\psi_p,\text{sec}}$	Enriched secant tangent matrix for the principal crack
$\mathbf{K}_{\psi_p,\text{sec}}$	Enriched secant tangent matrix for the secondary crack
$\mathbf{K}_{\psi_p,\text{sec}}$	Enriched secant tangent matrix for the coupling of both cracks
$\mathbf{K}_{\text{tan}}$	Tangent matrix
ℓ	Characteristic length of a non-local damage model
$\mathbf{M}$	Mass matrix
$\mathbf{M}_{\psi_p}$	Enriched mass matrix for the principal crack
$\mathbf{M}_{\psi_s}$	Enriched mass matrix for the secondary crack

$\mathbf{M}_{\psi_b}$	Enriched mass matrix for the coupling of both cracks
$\mathbf{N}$	Matrix of standard finite element shape functions
$\boldsymbol{n}$	Outward unit normal to the boundary
$\mathbf{T}$	Matrix that takes into account the cohesive forces
$\bar{\boldsymbol{t}}$	Traction on the Neumann boundary
$\bar{\boldsymbol{t}}_d$	Traction on the discontinuity surface of the principal crack
$\bar{\boldsymbol{t}}_s$	Traction on the discontinuity surface of the secondary crack
$\boldsymbol{u}$	Standard displacement field
$\boldsymbol{u}_c$	Regular standard displacement field
$\boldsymbol{u}_p$	Enhanced standard displacement field for the principal crack
$\boldsymbol{u}_s$	Enhanced standard displacement field for the secondary crack
$\mathbf{u}$	Standard nodal displacement vector
$\mathbf{u}_c$	Regular standard nodal displacement vector
$\mathbf{u}_p$	Enhanced standard nodal displacement vector for the principal crack
$\mathbf{u}_s$	Enhanced standard nodal displacement vector for the secondary crack
$\widetilde{\boldsymbol{u}}$	Smoothed displacement field
$\widetilde{\boldsymbol{u}}_c$	Regular smoothed displacement field
$\widetilde{\boldsymbol{u}}_p$	Enhanced smoothed displacement field for the principal crack
$\widetilde{\boldsymbol{u}}_s$	Enhanced smoothed displacement field for the secondary crack
$\widetilde{\mathbf{u}}$	Smoothed nodal displacement vector
$\widetilde{\mathbf{u}}_c$	Regular smoothed nodal displacement vector
$\widetilde{\mathbf{u}}_p$	Enhanced smoothed nodal displacement vector for the principal crack
$\widetilde{\mathbf{u}}_s$	Enhanced smoothed nodal displacement vector for the secondary crack
u^*	Prescribed displacement on the Dirichlet boundary
$[\![\boldsymbol{u}]\!]$	Crack opening
$\boldsymbol{x}$	Spatial coordinate vector
Y	Local state variable of a damage model
$\widetilde{Y}$	Smoothed state variable of a damage model
Y_0	Damage initiation state variable
Y_f	Maximum admissible value for the state variable

Greek symbols

Γ	Boundary surface
Γ_d	Discontinuity surface of the principal crack
Γ_s	Discontinuity surface of the secondary crack
Γ_t	Boundary surface where tractions are prescribed (Neumann boundary)
Γ_u	Boundary surface where displacements are prescribed (Dirichlet boundary)
$\boldsymbol{\varepsilon}$	Small strain tensor
$\widetilde{\boldsymbol{\varepsilon}}$	Smoothed small strain tensor
ε_i	Principal strains

θ	Separation angle
λ_{equi}	Lagrange multipliers for the equilibrium equations
λ_{reg}	Lagrange multipliers for the regularisation equations
ν	Poisson's ratio
$\boldsymbol{\sigma}$	Stress tensor
$\boldsymbol{\tau}$	Tangent vector to the boundary
ψ_p	Sign function for the principal crack
ψ_s	Sign function for the secondary crack
ψ_b	Sign function for crack branching elements
Ω	Domain of $\mathbb{R}^2$ occupied by the solid
$\boldsymbol{\omega}_c$	Regular test function of local displacement
$\boldsymbol{\omega}_p$	Enhanced test function of local displacement for the principal crack
$\boldsymbol{\omega}_s$	Enhanced test function of local displacement for the secondary crack
$\widetilde{\boldsymbol{\omega}}_c$	Regular test function of smoothed displacement
$\widetilde{\boldsymbol{\omega}}_p$	Enhanced test function of smoothed displacement for the principal crack
$\widetilde{\boldsymbol{\omega}}_s$	Enhanced test function of of smoothed displacement for the secondary crack

Operators

In the following, a scalar is represented with the italic type S, a vector with the bold-face type $\boldsymbol{V}$ and tensors with the bold-face type $\mathbf{A}, \mathbf{B}$.

$:$ Double contraction
Double contraction of two tensors: $\mathbf{A} : \mathbf{B} = A_{ij}B_{ij}$

∇ Gradient
Gradient of a scalar in cartesian coordinates: $\nabla S = \frac{\partial S}{\partial x}\boldsymbol{e}_x + \frac{\partial S}{\partial y}\boldsymbol{e}_y + \frac{\partial S}{\partial z}\boldsymbol{e}_z$
Gradient of a vector in cartesian coordinates: $\nabla \boldsymbol{V} = \begin{pmatrix} \frac{\partial V_x}{\partial x} & \frac{\partial V_x}{\partial y} & \frac{\partial V_x}{\partial z} \\ \frac{\partial V_y}{\partial x} & \frac{\partial V_y}{\partial y} & \frac{\partial V_y}{\partial z} \\ \frac{\partial V_z}{\partial x} & \frac{\partial V_z}{\partial y} & \frac{\partial V_z}{\partial z} \end{pmatrix}$

$\nabla\cdot$ Divergence
Divergence of a vector in cartesian coordinates: $\nabla \cdot \boldsymbol{V} = \frac{\partial V_x}{\partial x} + \frac{\partial V_y}{\partial y} + \frac{\partial V_z}{\partial z}$

∇^2 Laplacian
Laplacian of a scalar in cartesian coordinates: $\nabla^2 S = \frac{\partial^2 S}{\partial x^2} + \frac{\partial^2 S}{\partial y^2} + \frac{\partial^2 S}{\partial z^2}$

∇^s Symmetrised gradient
Symmetrised gradient of a vector in cartesian coordinates: $\nabla^s \boldsymbol{V} = \frac{1}{2}\left(\nabla \boldsymbol{V} + \nabla \boldsymbol{V}^T\right)$

Acronyms

$\theta-$SMA	$\theta-$simplified medial axis
BEM	Boundary element method
EFEM	Embedded finite element method
FEM	Finite element method
GFEM	Generalized finite element method
HX-FEM	Harmonic extended finite element method
MA	Medial axis
PDE	Partial differential equation
X-FEM	Extended finite element method

Chapter 1

Introduction

Failure of quasi-brittle materials —such as concrete and rocks— is characterised by a process of strain localisation and damage accumulation that ultimately leads to macrocracks and the eventual loss of load-carrying capacity. The understanding of this type of failure —from damage inception to crack propagation— is essential for the accurate analysis of structural integrity. A particular phenomenon that arises in quasi-brittle failure when a crack propagates is its bifurcation in two or more new cracks, i.e. crack branching.

In civil engineering, crack branching may appear in many problems, see Figure 1.1. In dynamic analysis, it is observed that as cracks travel faster in brittle solids such as concrete, rocks and rock-like materials, they tend to branch out due to instabilities. In quasi-static analysis, crack branching may occur in concrete structures —such as floor slabs— or in hydraulic fracture of rocks. Indeed, quasi-brittle fracture is known to be sensitive to local heterogeneities and boundary conditions that explain crack deviation and crack branching. Crack branching may also appear in problems as diverse as high velocity impacts and corrosion-assisted cracking.

In order to understand quasi-brittle failure, both experimental and numerical tests can be carried out. Even if experimental tests cannot be totally replaced by numerical tests, they can be complemented and reduced by numerical simulations. Numerical tests allow to obtain results at a much lower cost and time, can be easily repeated and allow the analysis of full-scale structures.

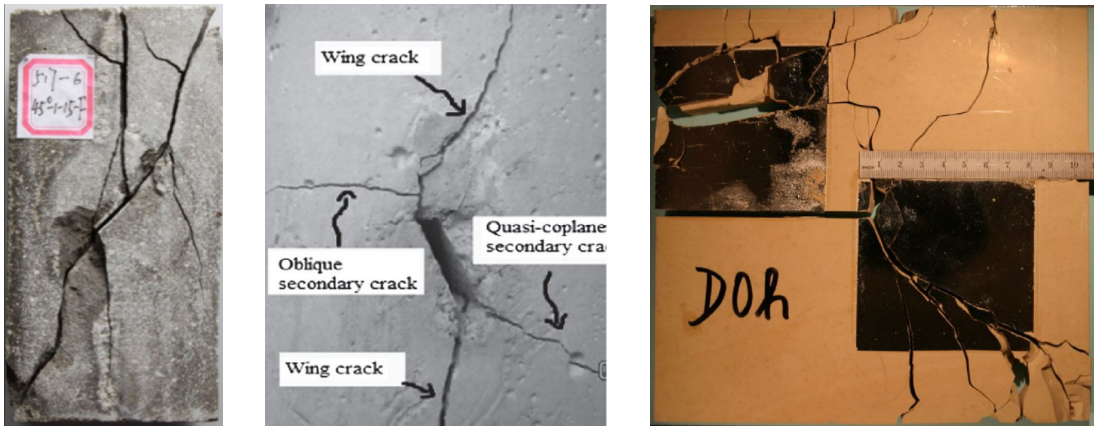

(a) (b) (c)

Figure 1.1: Crack branching in (a) rocks from Zhuang et al. (2014), (b) in concrete from Marji (2014) and (c) in high velocity impacts from Yang et al. (2015).

The numerical simulation of the failure process of quasi-brittle materials has been extensively studied by means of two classical theories: (a) damage mechanics, which is based on continuous models, and (b) fracture mechanics, which belongs to the family of discontinuous models.

Damage mechanics assumes a continuous displacement field, leading to a continuous strain field. Material degradation is accounted for by means of a scalar damage variable that reduces locally the stiffness, accounting for strain softening. Cracks are represented by regions where damage overpasses a critical value, i.e. regions that have lost their load-carrying capacity. Regularised formulations are used in damage mechanics to control strain localisation and overcome mesh size dependence on numerical simulations. Damage mechanics are used to describe the early stages of the failure process —damage inception and propagation— but fail to represent macroscopic cracks appearing in the last stages of the failure process.

Fracture mechanics, represented by discontinuous approaches, explicitly describes cracks by means of a discontinuous displacement field. Among many other techniques, the Extended Finite Element Method (X-FEM) can be used to capture these displacement discontinuities. Thus, discontinuous models can adequately be used in the last stages of failure, when cracks are physically observed. However, these types of models cannot describe damage inception and propagation.

In order to properly characterise the whole failure process both classical theories

—damage and fracture mechanics— can be merged. The main idea of this approach —based on continuous-discontinuous models— is to describe damage inception and evolution by means of damage mechanics and employ fracture mechanics to explicitly introduce cracks.

The objective of this thesis is to use a continuous-discontinuous approach for tackling crack branching. For the early stages of the failure process, a gradient-enhanced model based on smoothed displacements is employed. When damage parameter exceeds a critical value, a crack is introduced by incorporating a discontinuous approximation of the displacement field. If a branched crack is introduced, two discontinuous displacement functions are incorporated in the approximation space for the displacement and the elements are properly enriched with the X-FEM in order to account for both branches.

In order to develop a finite element approach for crack branching in quasi-brittle failure by means of a continuous-discontinuous model, three goals —each of one is presented in a chapter— have been considered:

1. **To propose a X-FEM enrichment to simulate crack branching**. Chapter 3 focuses on the discontinuous model used to introduce a discontinuous displacement field that takes into account crack branching. An enrichment scheme based on the X-FEM is proposed and tested.

2. **To extend the continuous-discontinuous formulation based on non-local displacements to crack branching**. The continuous-discontinuous model presented by Tamayo-Mas and Rodríguez-Ferran (2014) and Tamayo-Mas (2013) is used for the numerical simulation of quasi-brittle failure. Chapter 4 deals with the introduction of crack branching in this formulation, accounting for the necessary changes —in the weak form of the governing equations, in the finite element discretisation and in the linearisation of the discrete weak form— introduced by a second crack and using the X-FEM enrichment proposed in Chapter 3. The geometric criterion —from Tamayo-Mas and Rodríguez-Ferran (2015) and Tamayo-Mas (2013)— used for crack path tracking is also presented.

3. **To verify the capabilities of the approach presented by performing a numerical simulation with crack branching**. In Chapter 5 a numerical test is carried out to test the capabilities of the X-FEM enrichment built

and its implementation in a continuous-discontinuous model. Additionally, the geometrical criterion used for identifying crack path is also verified.

All the codes and simulations of this thesis have been performed in MATLAB. ParaView has been used for the visualisation of results.

Chapter 2

State of the art

This chapter provides an overview of the approaches used in quasi-brittle failure simulation, especially in continuous and discontinuous models. Within the discontinuous models, a review of different numerical methods that account for displacement discontinuities is presented, placing especial attention in recent developments in the numerical simulation of crack branching.

2.1 Introduction

Computational approaches to failure of quasi-brittle materials —such as concrete or rocks— have traditionally used two distinct concepts: damage mechanics and fracture mechanics. The former belongs to the family of continuous models while the later falls in the family of discontinuous models. In the framework of damage mechanics, where continuous approaches are used, cracks are not explicitly represented, but an internal variable is introduced to represent local modifications to the elastic stiffness tensor leading to material degradation. In fracture mechanics, discontinuous approaches are used to model the geometrical discontinuity of the crack as a discontinuity in the displacement field.

Other less common approaches, which do not exactly fall in the two categories above, include discrete approaches. Discrete models describe materials as agglomerations of physical particles —instead of a continuum— which are modeled by discrete elements that interact.

In this chapter, we first present an overview of continuous failure models in Section 2.2. In Section 2.3 discontinuous failure models are reviewed, paying special attention to current developments in the explicit representation of crack branching. Last, in Section 2.4 a review on continuous-discontinuous schemes for quasi-brittle failure is provided.

2.2 Damage mechanics: continuous failure models

Continuous failure models are used for the first stages of failure, where material degradation appears but no macroscopic cracks are visible. Failure is simulated assuming a continuously differentiable displacement field and cracks are represented by continuum regions that have lost their load-carrying capacity. The basic idea of these damage models is that material degradation is accounted for by means of a scalar damage variable $0 \leq D \leq 1$. This variable degrades the elastic stiffness with the accumulation of damage, leading to the stress-strain relation

$$\boldsymbol{\sigma} = (1 - D)\, \boldsymbol{C} : \boldsymbol{\varepsilon} \tag{2.1}$$

Undamaged material is characterised by $D = 0$, while $D = 1$ corresponds to complete loss of stiffness. Thus, continuous models allow to represent damage initiation and growth.

The use of classical (local) damage models theories can result in ill-posed initial boundary problems when a certain level of loading is reached. This is due to the fact that strain softening can induce localisation of the entire degradation process in a vanishing volume —which depends on the mesh size—, resulting in a local loss of ellipticity of the differential equations. As a consequence, local damage models may give rise to pathological mesh dependence.

In order to solve the drawbacks of local damage models, different techniques can be used. On the one hand, the crack-band approach may be employed to overcome this problem, see Jirásek and Bauer (2012). This method consists of removing the pathological mesh dependence by adjusting the post-peak slope of the stress-strain curve on the width of the localised band, which is closely related to the finite element size. However, the use of this method is not straightforward, since the success of the

method depends on many factors, such as the element type and shape and direction of the crack-band, to name some.

On the other hand, non-local (regularised) damage models may be used to prevent localisation into an arbitrar small volume and remove mesh dependence. An additional parameter —the characteristic length ℓ— is included in these models. Two types of formulations stand out in the literature: integral-type and gradient-type non-local models, see Rodríguez-Ferran et al. (2005).

In standard integral-type non-local damage models, damage is regularised through the definition of a non-local internal variable $\widetilde{Y}$, see Bažant and Jirásek (2002). This variable is computed, from the integration over a surrounding zone, as the weighted average of the local internal variable Y. Gradient-type non-local (gradient-enhanced) models have a differential —instead of an integral— relationship between local and non-local variables, where regularisation is obtained through the addition of gradient-dependent terms in the constitutive problem. Both explicit and implicit formulations of the gradient-enhanced damage models can be used, see Peerlings et al. (2001).

A particular case of integral and gradient-type non-local models is the non-local model based on non-local displacements presented by Rodríguez-Ferran et al. (2005). In this method non-locality is introduced at the level of displacements rather than some internal variable. The main advantage of this method is the consistent linearisation of the tangent matrix to attain quadratic convergence in the full Newton-Raphson method. **The gradient version of this method will be used in this thesis to regularise softening**.

A more recent type of non-local models are phase-field models, which is closely related to the gradient-enhanced model. The basic idea of phase-field models is to replace the discontinuity by a small, but finite zone with sharp gradients, see de Borst and Verhoosel (2016).

The main drawback of continuous models is their inability to represent discrete failure surfaces, thus failing to model last stages of failure, when macrocracks are present. In this situation the use of fracture mechanics is necessary.

2.3 Fracture mechanics: discontinuous failure models

In contrast to continuous failure models, fracture mechanics describes failure by means of a discontinuous displacement field (opening of a crack). Hence, they can be employed to capture the last stages of failure —when cracks are physically observed— but cannot adequately capture diffuse degradation.

Nowadays, there exist many numerical methods that are capable of treating cracks by introducing jump discontinuities in the displacement field. Some of them are reviewed here, but for a more extensive review see Rabczuk et al. (2010).

Finite elements coupled with adaptive remeshing can be used to account for displacement discontinuities. In remeshing methods, the element faces are aligned with the crack and the nodes located on these faces are doubled. The main drawback of this method is that the finite element mesh must be adapted after each loading step, if the crack propagates, and requires mapping the internal variables between different meshes.

Embedded discontinuities can handle arbitrary crack paths without remeshing. The embedded finite element method (EFEM) is based on an enrichment at the element level, see Jirásek (2000) for a detailed review. Additionally, the enriched parameters can be eliminated by their static condensation at the element level, resulting in minor modifications to existing finite element codes.

The eXtended Finite Element Method (X-FEM), see Belytschko and Black (1999) and Moës et al. (1999), has become one of the most used techniques to simulate propagating cracks. It is based on a decomposition of the displacement field in a continuous part and a discontinuous part, where the Partition of Unity concept is used. In contrast to the EFEM, the enrichment is nodal instead of elemental and the additional degrees of freedom inherent to the nodes are introduced in the variational formulation. Apart from discontinuities, the X-FEM can also be used for high gradients as shown by Fries and Belytschko (2010), avoiding the refinement of the mesh that would be required if only the classical FEM was used. For a general overview of the developments and applications of the X-FEM in computational fracture mechanics, we refer to the recent review by Sukumar et al. (2015).

Other techniques may include the generalized finite element method (GFEM)

which is similar to X-FEM, meshfree methods and boundary element methods (BEM). In this thesis, the **X-FEM is used to introduce crack branching**.

2.3.1 Crack branching

Crack branching is characterised by the presence of two intersecting discontinuities in the displacement field. In order to incorporate a branched crack in a discontinuous model the numerical methods used for a propagating crack must be adapted. Here, we present a review of the different approaches proposed to tackle crack branching with discontinuous models.

Daux et al. (2000) propose a new discontinuous function (the 'branched' or 'junction' function) that allows to account for a branched crack. Sheng et al. (2015) use this function to develop an approach to handle multiple fractures in the numerical simulation of fluid flow in deformable porous media.

Belytschko et al. (2001) and Duarte et al. (2007) enrich the elements with two linearly independent functions, the step sign functions —which take value +1 at one side of the crack and 0 at the other—, instead of defining a special 'junction' function for the branched element.

Other techniques, apart from the X-FEM, are useful to take into account crack branching in simulations. For instance, Linder and Armero (2009) develop new finite elements to introduce crack branching in brittle materials using the FEM with embedded strong discontinuities (EFEM). An extrinsically enriched meshfree method is used by Bordas et al. (2008) for initiation, branching, growth and coalescence of cracks. Rabczuk et al. (2010) present a method for crack branching based on the extended element-free Galerkin method, by using the sign enrichment functions and the signed distance functions. Last, Mousavi et al. (2011) analyse crack branching using the harmonic X-FEM or HX-FEM. In contrast to standard X-FEM, in HX-FEM the enrichment functions are numerically computed, being the solution of the Laplace equation with special boundary conditions that account for crack branching.

In the context of n-phase flow problems, Zlotnik and Díez (2009) present a hierarchical X-FEM approach for triple (or multiple) junctions inside an element.

In this thesis, **an alternative enrichment with the X-FEM is proposed and tested**.

2.4 Continuous-discontinuous failure models

In order to achieve a better understanding of quasi-brittle failure, continuous-discontinuous approaches have emerged. These approaches combine damage and fracture mechanics in order to describe the whole failure process. Damage mechanics is used for damage inception and propagation. In the last stages of failure, cracks are explicitly introduced with a discontinuous model —i.e., fracture mechanics—, while damage mechanics continues to drive damage evolution.

Continuous-discontinuous approaches are characterised by three stages:

- **Continuous regime**: in the first stages of failure, continuous models based on damage mechanics are used to characterise the inception and evolution of damage. Non-local damage models are preferred due to the pathological mesh dependence of local models.
- **Transition**: in order to change from a continuous model to a discontinuous approach three aspects must be taken into account. First, the criterion used for deciding when a crack is introduced must be established. Normally, this is done when the damage reaches a given critical value. Second, the crack path must be identified in order to locate the crack. Either mechanical or geometrical criteria can be used. Last, energy consistency should be verified, by ensuring that no loss of energy takes place when replacing the damage zone by a crack.
- **Discontinuous regime**: once the crack is introduced, a discontinuous approach —such as X-FEM— is used to model the last stages of the failure process, where damage is driven by the damage model.

Several examples of merging both theories —damage and fracture mechanics— are found in the literature. For instance, Jirásek and Zimmermann (2001) couple a non-local damage model with embedded discontinuities. Simone et al. (2003) introduce propagating cracks according to the X-FEM within a gradient-enhanced non-local model. Roth et al. (2015) present a continuum damage model with a cohesive X-FEM formulation to transfer energy dissipation from the damage mechanics approach to the X-FEM model.

In Tamayo-Mas and Rodríguez-Ferran (2014), the whole failure process is tackled with a continuous-discontinuous model that uses an implicit gradient-enhanced

damage model based on smoothed displacement to drive damage evolution and the X-FEM to introduce and propagate the crack. **This model will be used in this thesis to model crack branching in quasi-brittle failure**.

Chapter 3

X-FEM enrichment for crack branching

This chapter focuses on the use of the eXtended Finite Element Method (X-FEM) to simulate crack branching. A finite element nodal enrichment for a finite element mesh with a branched crack is presented and tested with some numerical examples.

3.1 Introduction

The standard finite element method (FEM) does not allow the modelling of discontinuities, due to the fact that shape functions are continuous, thus leading to a continuous numerical solution of the problem. Cracks are characterised by a jump in the displacement field, and therefore alternative methods must be used to explicitly introduce a crack in fracture mechanics.

One way of using the standard FEM in a discontinuous model is to align the element faces with the crack and double the nodes located on these faces, so as to account for displacement discontinuities. However, using this approach, the finite element mesh must be reconstructed each time the crack propagates, in order to ensure that the crack is always aligned with the mesh.

Among other strategies, X-FEM has emerged in order to overcome this limitation, allowing for the modelling of crack growth independently of the finite element mesh,

and therefore without remeshing. By using X-FEM the continuous approximation is enriched with additional discontinuous functions satisfying the partition of unity concept, see Melenk and Babuška (1996). The use of the partition of unity as a means to enrich a finite element space may be found in Strouboulis et al. (2000).

In discontinuous modelling, if the discrete crack is introduced by means of X-FEM, the standard displacement field $\boldsymbol{u}(\boldsymbol{x})$ —and the gradient-enhanced displacement field $\widetilde{\boldsymbol{u}}(\boldsymbol{x})$, if non-local damage models are used— is enriched with discontinuities functions, in particular, the sign function.

An important issue concerning the addition of a second crack that intersects with the first crack, is how the elements with multiple cracks shall be enriched with the discontinuous functions to allow the two discontinuities to occur.

Different enrichments can be used in the case of crack branching. For instance, Daux et al. (2000) propose a new discontinuous function (the 'branched' or 'junction' function) that allows to account for a branched crack, see Figure 3.1. Belytschko et al. (2001) consider enriching the nodes with two linearly independent functions, the step sign function —which takes value +1 at one side of the crack and 0 at the other—, instead of the 'junction' function.

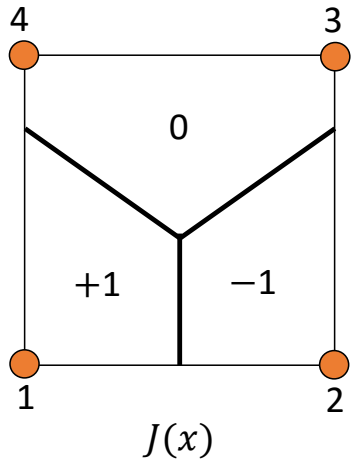

Figure 3.1: 'Junction' or 'branched' function.

In this chapter, we extend the applicability of X-FEM to crack branching (i.e. two intersecting cracks) by presenting an alternative enrichment scheme.

The structure of this chapter is as follows. In Section 3.2 the X-FEM enrichment

for one crack is reviewed. In Section 3.3 an alternative X-FEM enrichment for crack branching is developed. Special emphasis is placed on the enrichment of the element with crack branching and its assembly with adjacent elements. In Section 3.4 the capabilities of this X-FEM enrichment for crack branching are illustrated by means of an elastic numerical example.

3.2 Finite element enrichment with X-FEM: one crack

Given a body Ω with a crack represented by a discontinuity Γ_p, according to the X-FEM, the displacement field $\boldsymbol{u}(\boldsymbol{x})$ can be decomposed as

$$\boldsymbol{u}(\boldsymbol{x}) = \boldsymbol{u}_c(\boldsymbol{x}) + \psi_p(\boldsymbol{x})\,\boldsymbol{u}_p(\boldsymbol{x}) \tag{3.1}$$

where $\boldsymbol{u}_c, \boldsymbol{u}_p$ are continuous fields in Ω and ψ_p is the sign function centred at the discontinuity Γ_p. Therefore, ψ_p is a discontinuous function across the crack surface and is constant on each side of the crack: $+1$ in one side of the crack and -1 on the other. It is noted that if the body Ω is not entirely crossed by the discontinuity Γ_p it is difficult to define what value does the discontinuous function ψ_p take beyond the discontinuity tip, since the body Ω is not strictly divided into two subdomains by the crack defined by Γ_p, see Figure 3.2(a). However, this ambiguity is solved by the fact that the enrichment function is multiplied by nodal shape functions that vanish in the region where ψ_p is ambiguous.

Therefore, the main idea of using X-FEM for simulating a crack is to use a continuous function for all the body Ω, and include a discontinuous field $\psi_p \boldsymbol{u}_p$ to model the crack.

3.2.1 Finite element discretisation

Regarding the finite element discretisation, displacement reads, in the domain of an element crossed by a crack,

$$\boldsymbol{u}(\boldsymbol{x}) \simeq \boldsymbol{u}^h(\boldsymbol{x}) = \sum_{i=1}^{4} \mathbf{N}_i(\boldsymbol{x})\,\mathbf{u}_i^c + \sum_{j=1}^{4} \psi_p(\boldsymbol{x})\,\mathbf{N}_j(\boldsymbol{x})\,\mathbf{u}_j^p \tag{3.2}$$

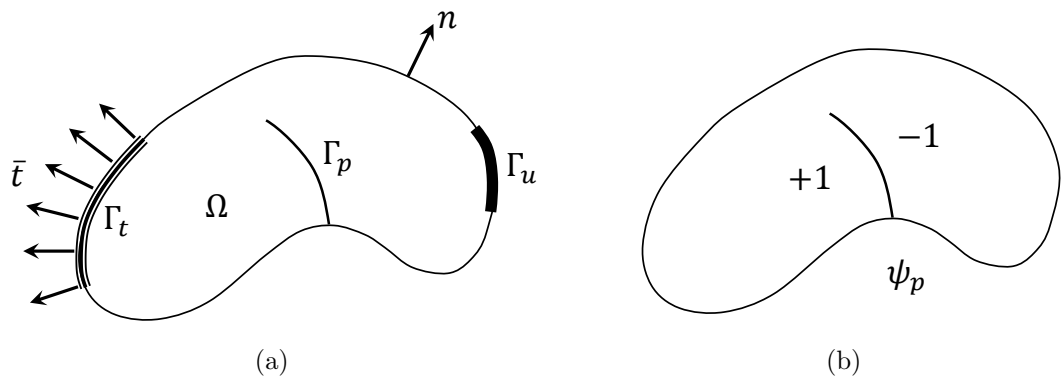

(a) (b)

Figure 3.2: Left: (a) a body with a crack subjected to loads and imposed displacements. Right: (b) definition of ψ_p in the body.

where $\mathbf{u}_i^c$ are the basic nodal degrees of freedom and $\mathbf{u}_j^p$ the enhanced ones associated to the discontinuity Γ_p.

Notice that for an element entirely crossed by a crack (see Figure 3.3), in particular the quadrilateral element of reference with 4 nodes, the shape functions N_i and $\psi_p(\boldsymbol{x})\mathbf{N}_j$ (see Figure 3.4) allow to get a discontinuous displacement field, since the enhanced shape functions $\psi_p(\boldsymbol{x})\mathbf{N}_j$ are discontinuous along the crack.

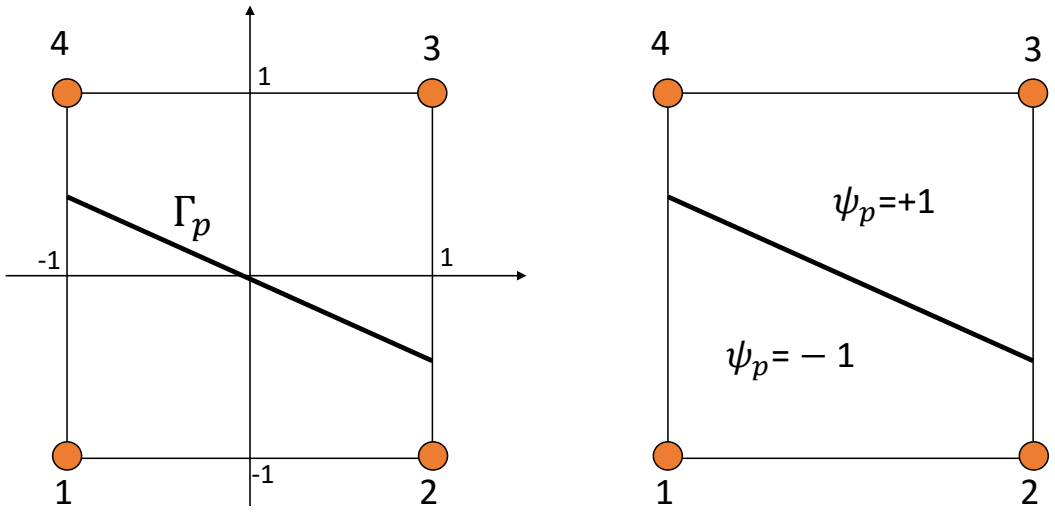

Figure 3.3: Quadrilateral element of reference crossed by one crack and definition of the sign function ψ_p.

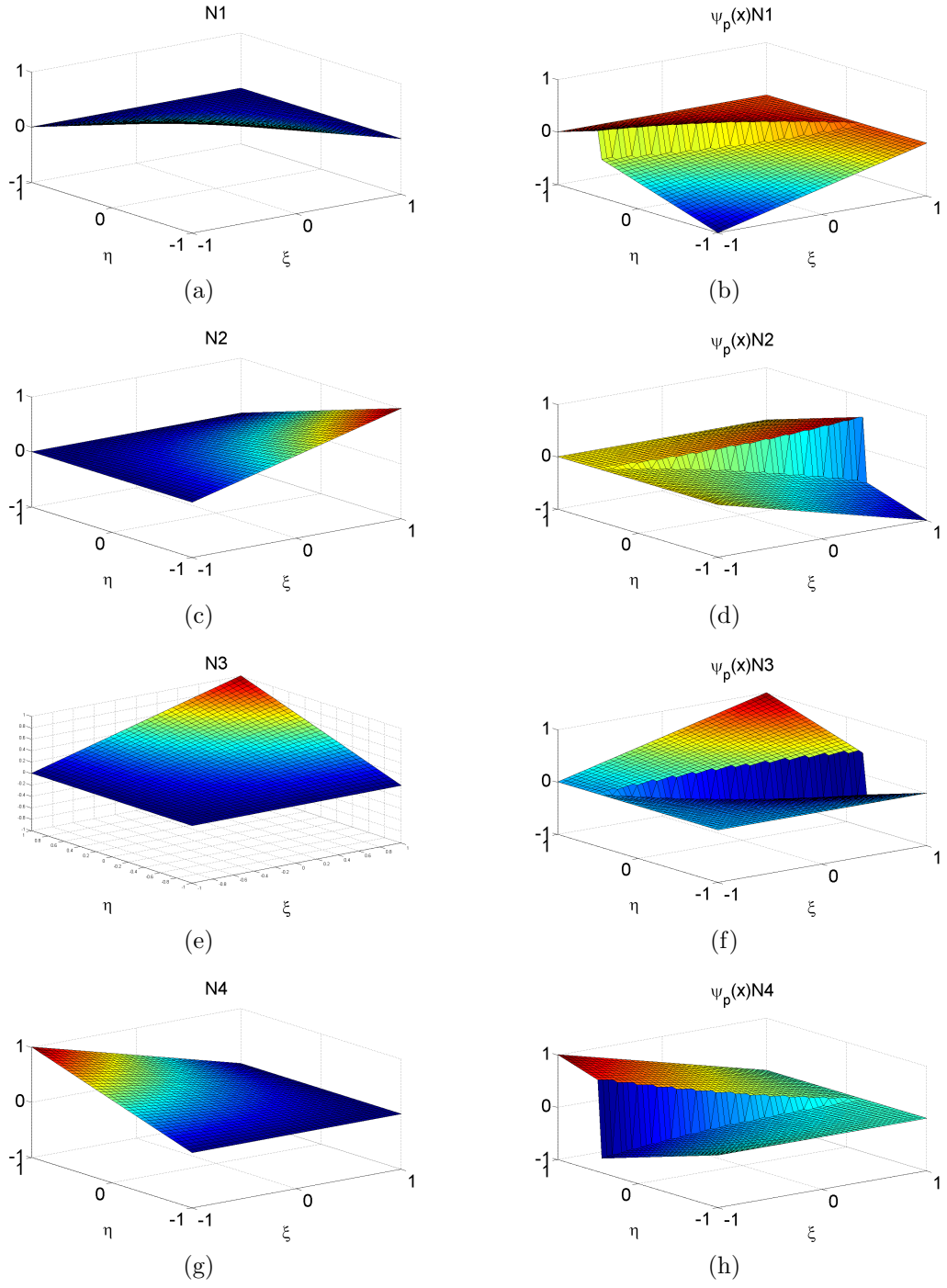

Figure 3.4: Left column: shape functions,(a) N_1, (c) N_2, (e) N_3 and (g) N_4. Right column: enriched shape functions (b) $\psi_p \mathbf{N}_1$, (d) $\psi_p \mathbf{N}_2$, (f) $\psi_p \mathbf{N}_3$ and (h) $\psi_p \mathbf{N}_4$.

3.3 Finite element enrichment with X-FEM: crack branching

In this section we present the finite element enrichment proposed for crack branching. First, in Section 3.3.1 the enrichment for an element with crack branching is presented and verified. Second, in Section 3.3.2 this element is coupled with contiguous elements and the X-FEM enrichment is tested under some elastic cases. Last, in Section 3.3.3 the proposed X-FEM enrichment for crack branching is presented.

3.3.1 One cracked element with two cracks

The finite element enrichment proposed for a finite element containing two cracks consists on defining two discontinuity functions, ψ_p and ψ_s, associated to each one of the two discontinuities Γ_p and Γ_s, see Figure 3.5. From here on, the crack associated to Γ_p will be referred as principal crack and the one associated to Γ_s as secondary crack.

Regarding the finite element discretisation, displacement reads, in the domain of one element crossed by two cracks,

$$\boldsymbol{u}(\boldsymbol{x}) \simeq \boldsymbol{u}^h(\boldsymbol{x}) = \sum_{i=1}^{4} \mathbf{N}_i(\boldsymbol{x})\,\mathbf{u}_i^c + \sum_{j=1}^{4} \psi_p(\boldsymbol{x})\,\mathbf{N}_j(\boldsymbol{x})\,\mathbf{u}_j^p + \sum_{k=1}^{4} \psi_s(\boldsymbol{x})\,\mathbf{N}_k(\boldsymbol{x})\,\mathbf{u}_k^s \qquad (3.3)$$

where $\mathbf{u}_i^c$ are the basic nodal degrees of freedom, $\mathbf{u}_j^p$ the enhanced ones for discontinuity Γ_p and $\mathbf{u}_k^s$ the enhanced ones to respresent discontinuity Γ_s.

The reference element is then divided into three areas. On the one hand, the discontinuity function ψ_p takes the value of $+1$ in the areas at one side of the principal crack Γ_p and the value of -1 in the areas at the other side of the crack, see Figure 3.6(a). On the other hand, the discontinuity function ψ_s takes the value of $+1$ in the areas at one side of the secondary crack Γ_s and the value of -1 in the areas at the other side of the crack, see Figure 3.6(b).

It shoud be noticed that an arbitrary criterion has not been used for choosing in which side of the crack (Γ_p or Γ_s) the discontinuity function (ψ_p or ψ_s) takes values $+1$ or -1. Both discontinuity functions must be in accordance. In the example of Figure 3.5, regarding the three areas in which the element is divided, see Figure 3.5(b), the functions ψ_p and ψ_s must take the same value on subdomains 1 and 2,

considering that the crack comes from the bottom of the element and then branches. This constraint will be discussed in more detail in the next section, when assembling the branching element with adjacent elements.

Additionally, in Figure 3.5 the discontinuity Γ_s does not cross the entire element, instead it stops when intersecting with discontinuity Γ_p. However, the sign function ψ_s must be defined by means of a discontinuity that entirely crosses the element, thus the discontinuity Γ_s —secondary crack— is supposed to continue the path of discontinuity Γ_p —principal crack— when the intersection is reached. In that way, the sign function associated to the secondary crack can be defined as in Figure 3.6(b).

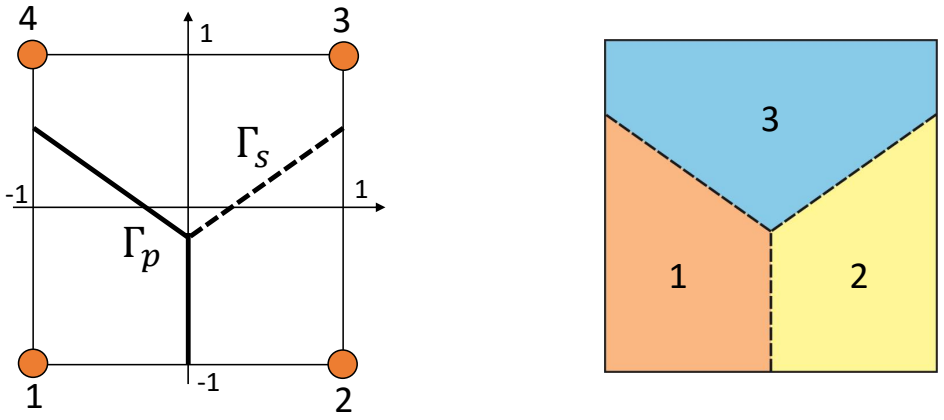

(a) (b)

Figure 3.5: (a) Quadrilateral element of reference crossed by two cracks. (b) Labels for the different subdomains.

In order to see whether this enrichment allows to effectively activate each discontinuity, we have analysed the elastic stiffness matrix (in 2D) resulting from this enrichment. Since the four nodes of the element are enriched by both discontinuities, there are 24 degrees of freedom (for each node: two standard displacements $\boldsymbol{u}_c$, two enhanced displacements for the principal crack $\boldsymbol{u}_p$ and two enhanced displacements for the secondary crack $\boldsymbol{u}_s$). Therefore an elastic stiffness matrix of dimensions 24×24 is obtained.

Rigid modes —two translations and one infinitesimal rotation— of each of the three subdomains, see Figure 3.8, in which the element is divided by both cracks have zero eigenvalue. Indeed, if eigenvalues are computed with the MATLAB function

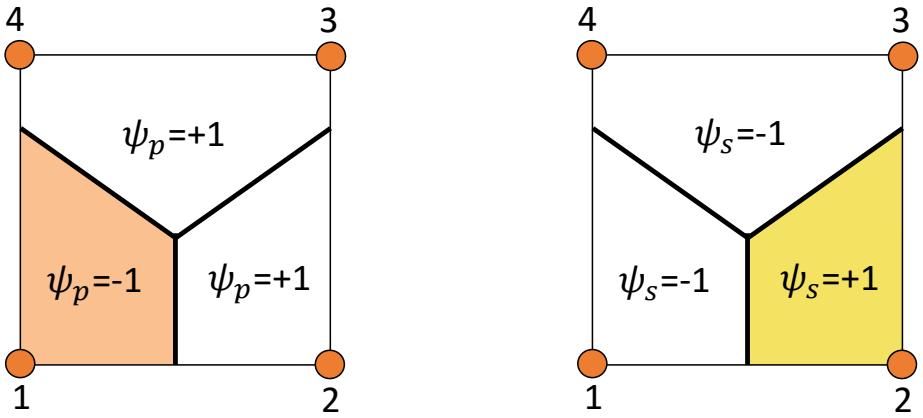

(a) (b)

Figure 3.6: (a) Definition of ψ_p in the reference element and (b) definition of ψ_s in the reference element.

'eig', we obtain that the elastic stiffness matrix has the eigenvalue 0 with multiplicity 9, whose eigenmodes are the nine rigid modes presented in Figure 3.8. Thus, this enrichment is valid for the element with crack branching.

Additionally, it is proved that this enrichment is also valid for any type of arrangement of both discontinuities. For instance, the point where crack branching occurs can be located on an edge of the element, the discontinuities may not be symmetric or may not intersect, see Figure 3.7. In fact, different types of crack arrangements will be used in the following sections to prove the capabilities of this enrichment.

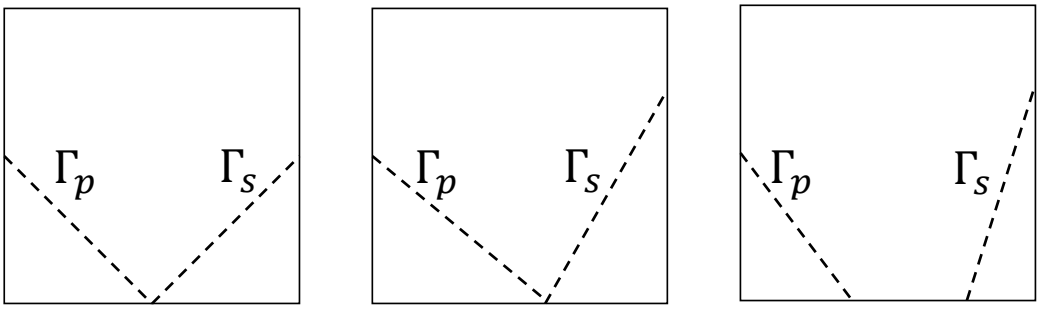

Figure 3.7: Quadrilateral element with different discontinuity arrangements

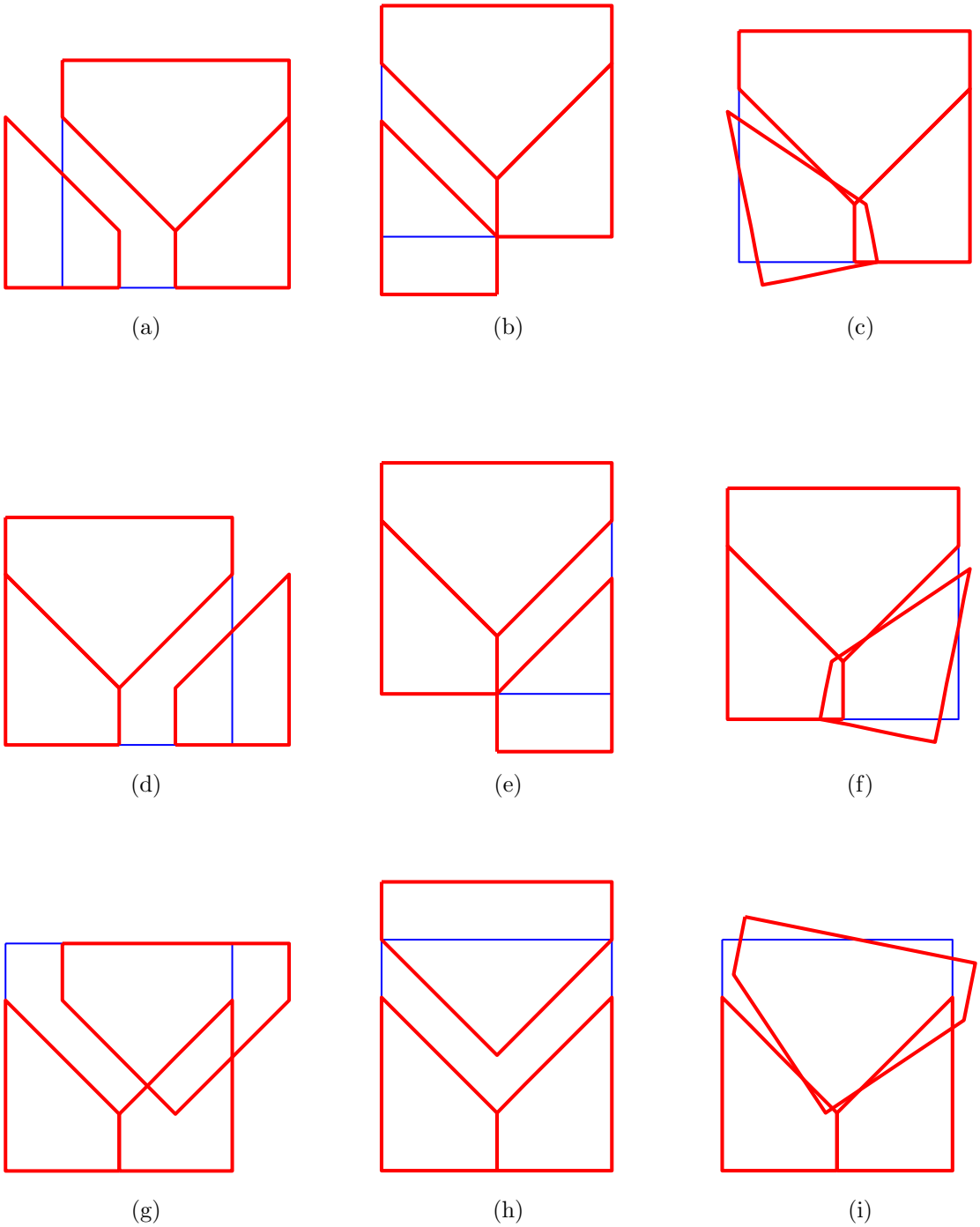

Figure 3.8: Rigid modes of each subdomain, arranged in: first row, subdomain 1; second row, subdomain 2; third row, subdomain 3; left column, horizontal translations; center column, vertical translations; right column, rotations.

3.3.2 Coupling the element with crack branching

With the proposed X-FEM enrichment for elements with crack branching, both discontinuities can be reproduced. Once the element with crack branching is enriched, the adjacent elements that only contain one crack must be enriched with the corresponding function ψ_p for the principal crack and ψ_s for the secondary crack.

It is a critical issue to see how the element containing crack branching is assembled with contiguous elements. The orientation of the sign functions ψ_p and ψ_s must be the same along the corresponding discontinuities and therefore must not change in adjacent elements.

3.3.2.1 Coupling with the element before crack branching

If two elements, see Figure 3.9, are considered —the element with crack branching and the element before crack branching— the X-FEM enrichment must allow to: (a) separate the principal crack Γ_p on the element containing only one crack and (b) activate crack branching by opening the principal and secondary cracks (Γ_p and Γ_s) on the element containing crack branching. Notice that the orientation of the sign function ψ_p is maintained from one element to the other, see Figure 3.9(b).

In this case, the adjacent element —with only the principal crack— has all the nodes enhanced by the principal crack but only two nodes are enriched by the secondary crack. See Figure 3.9, where orange nodes are enhanced by the principal crack and yellow nodes are enhanced by the secondary crack. In this element two nodes are enriched even if the secondary crack does not cross the element. This is done in order to maintain continuity of displacements across the elements. If these two nodes were not enhanced and only displacements $\mathbf{u}_c$ and $\mathbf{u}_p$ were used for approximating the displacement field $\boldsymbol{u}$, there would be a discontinuity along the edge between both elements.

Since the secondary crack does not cross the adjacent element, the sign function ψ_s must be defined by the principal crack Γ_p and must maintain the same orientation as ψ_p. Thus, both sign functions, ψ_s and ψ_p, are the same in this element, see Figure 3.9. A different definition of the sign function ψ_s on the domain of that element would lead to an undesired second discontinuity.

The orientation defined for the sign functions ψ_p and ψ_s must be the same along

the principal and secondary cracks. This leads to the definition of ψ_p and ψ_s on the element containing crack branching shown in Figure 3.9.

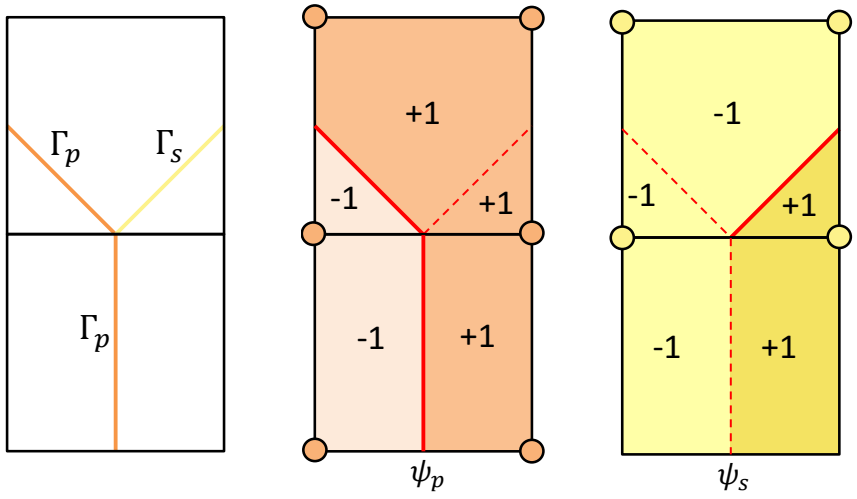

(a) (b) (c)

Figure 3.9: (a) Two elements with crack branching, (b) definition of ψ_p in the reference element and (c) definition of ψ_s in the reference element

The elastic stiffness matrix resulting from assembling both elements is of dimensions 32×32 and again has 9 zero eigenvalues. The corresponding eigenmodes are the rigid modes —two translations and one infinitesimal rotation— of each of the three subdomains defined by the principal and secondary cracks.

Indeed, the translation of each subdomain can be obtained with adequate boundary conditions as shown in Figure 3.10. Additionally, in order to verify the correct definition of the X-FEM enrichment, if the boundary conditions of Figure 3.11 are applied, both discontinuities are activated and the branched crack opens symmetrically.

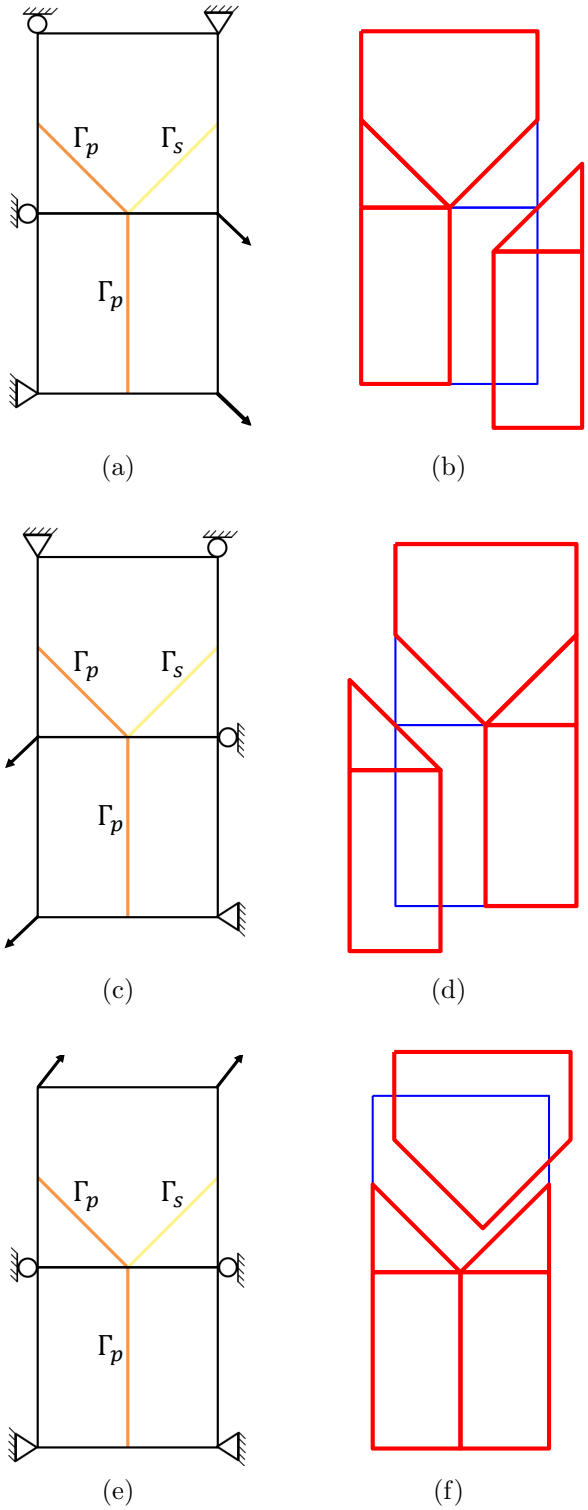

Figure 3.10: First row (a,b): translation of bottom-right subdomain, second row (c,d): translation of bottom-left subdomain, and third row (e,f): translation of upper subdomain.

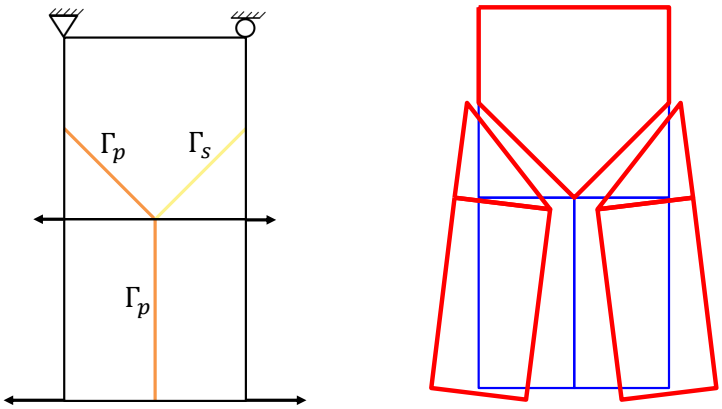

(a) (b)

Figure 3.11: Opening of crack branching.

3.3.2.2 Assembling several elements

If several elements are assembled, the coupling of the crack branching element with the contiguous elements is the same as the one described in Section 3.3.2.1. As seen in the example of Figure 3.12 the elements are enriched by the principal crack (orange nodes) and by the secondary crack (yellow nodes). The nodes of the element with crack branching are enhanced by both cracks (grey nodes).

The sign functions ψ_p and ψ_s keep the orientation on adjacent elements to the crack branching element. It is noted that the sign functions ψ_p and ψ_s are defined in the elements containing at least one enhanced node, see Figure 3.13. Therefore, the ambiguity associated with the definition of ψ_p and ψ_s when the body Ω is not entirely crossed by the principal and secondary cracks, is solved in the finite element discretisation. Indeed, the discontinuous functions ψ_p and ψ_s must only be defined locally, in the finite elements crossed by discontinuities and the adjacent ones.

The elastic stiffness matrix of the finite element discretization on Figure 3.12 (with dimensions 112×112) has the zero eigenvalue with multiplicity 9. This verifies that the X-FEM enrichment works well, since we can obtain the 3 rigid modes of each one of the three subdomains in which the body is divided by both cracks.

Indeed, as done in Section 3.3.2.1 for two elements, the three subdomains can be separated as shown in Figure 3.14. In addition, several tests have been carried out by

loading each one of the subdomains to verify that only the corresponding subdomain is deformed, activating the associated crack. Results are shown in Figure 3.14, with elements painted in red and black only for visualisation purposes.

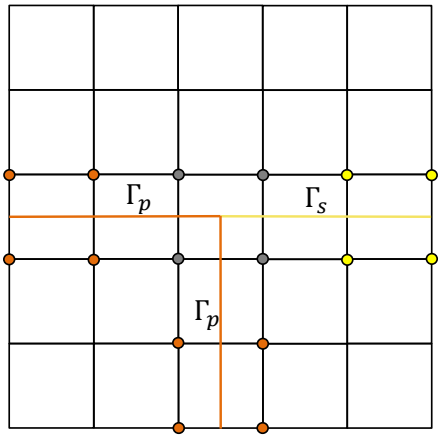

Figure 3.12: Mesh composed of 25 elements, with enriched nodes.

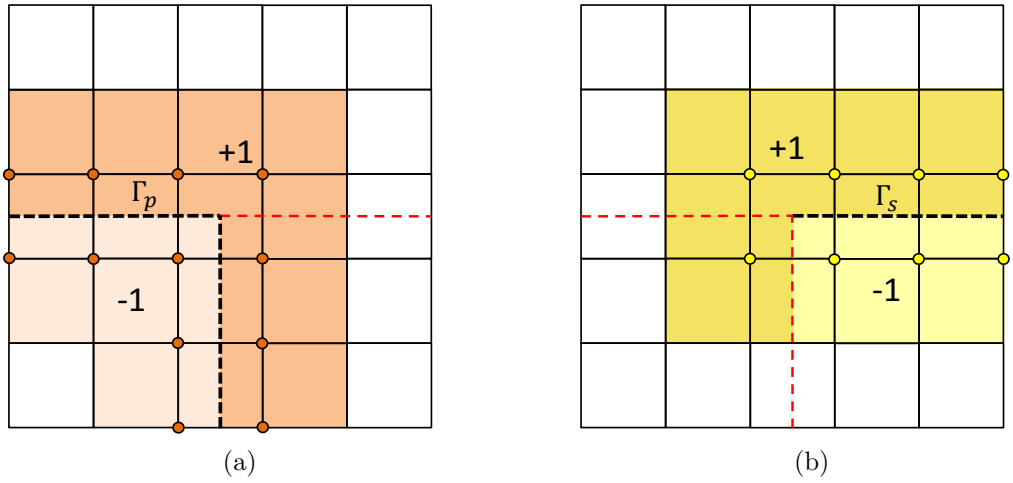

Figure 3.13: (a) Definition of ψ_p and (b) definition of ψ_s in the finite element mesh.

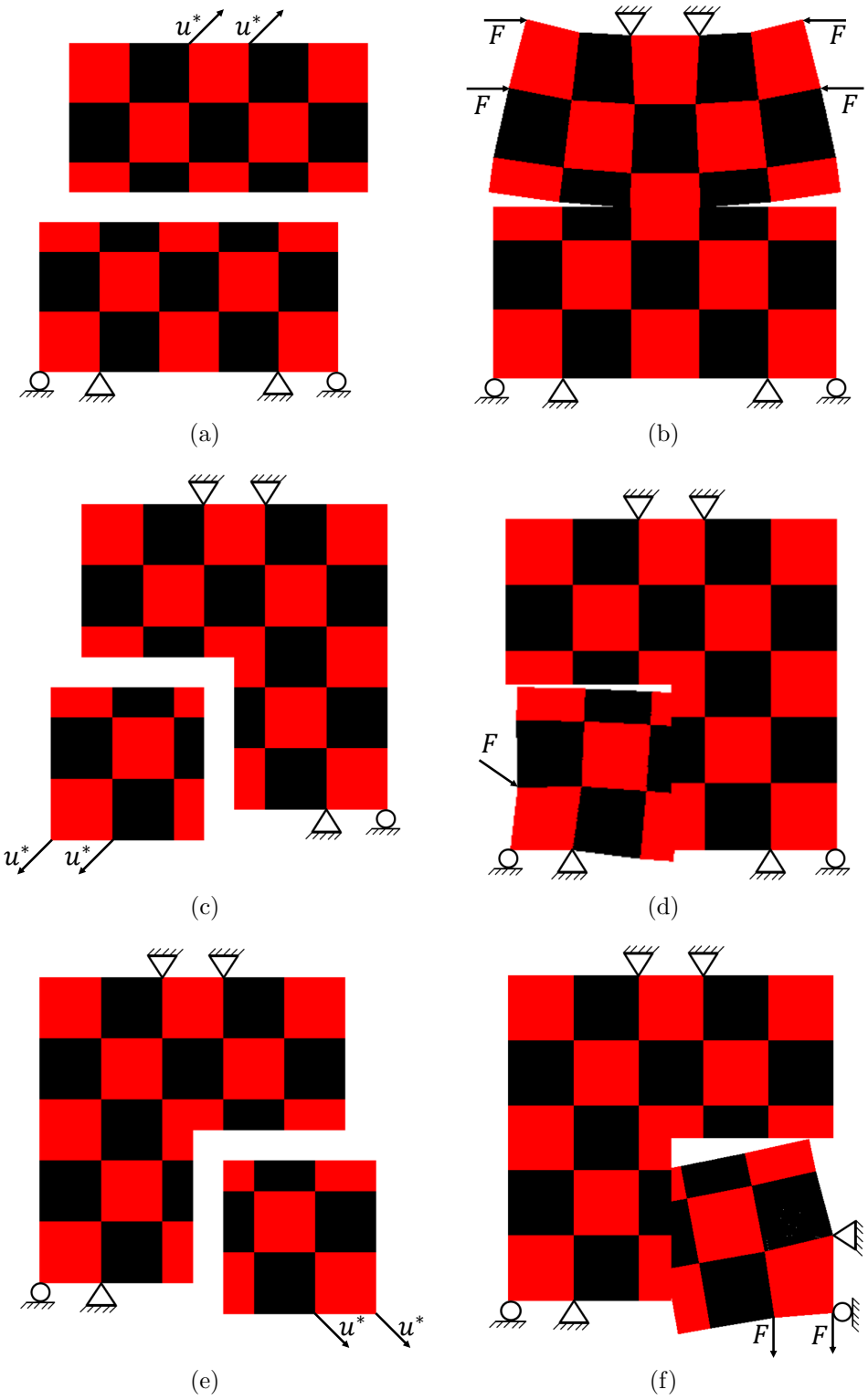

Figure 3.14: Translation of the (a) upper, (c) left-bottom and (e) right-bottom subdomain. Deformation of the (b) upper, (d) left-bottom and (f) right-bottom subdomain.

3.3.3 Proposed X-FEM enrichment

In Section 3.3.1 it has been verified that the X-FEM method allows to represent two cracks. The assembling with contiguous elements has been addressed in Section 3.3.2, concluding that with adequate considerations for the X-FEM enrichment it is possible to make the assambly with contiguous elements and still allow to represent crack branching. Additionally, it has been shown that it is not necessary to define a special sign function in the element with crack branching such as in Daux et al. (2000). It is enough to use both sign functions (ψ_p and ψ_s) corresponding to each one of the cracks.

Thus, in order to represent crack branching, the displacement field can be decomposed as

$$\boldsymbol{u}(\boldsymbol{x}) = \boldsymbol{u}_c(\boldsymbol{x}) + \psi_p(\boldsymbol{x})\,\boldsymbol{u}_p(\boldsymbol{x}) + \psi_s(\boldsymbol{x})\,\boldsymbol{u}_s(\boldsymbol{x}) \tag{3.4}$$

where $\boldsymbol{u}_c$, $\boldsymbol{u}_p$, $\boldsymbol{u}_s$ are continuous fields in Ω and ψ_p, ψ_s are the sign functions centred at discontinuities Γ_p and Γ_s, respectively.

Therefore, the displacement field is composed by a continuous field $\boldsymbol{u}_c$, a discontinuous field $\psi_p\boldsymbol{u}_p$ to represent the strong discontinuity associated to the principal crack Γ_p and a discontinuous field $\psi_s\boldsymbol{u}_s$ to represent the strong discontinuity associated to the secondary crack Γ_s.

Lets consider a general branched crack geometry as shown in Figure 3.15. If the finite element discretisation is performed, the nodes (squares) of the elements containing the principal crack (solid line) are enriched as if the secondary crack was absent. Analogously, the nodes (crosses) of the elements containing the secondary crack (dashed line) are enriched as if the principal crack was absent. The element with both cracks has the nodes (crosses inside squares) enriched by both discontinuities.

Notice that it is not necessary to define ψ_s and ψ_p in all the domain. The sign functions must only be defined in the elements that have at least one enhanced node —finite element containing a crack or on the vicinity of a crack—, when the finite element discretisation is performed.

It is worth to notice that no tip functions are used in the description of the displacement field $\boldsymbol{u}$. Thus, the crack tip must be located in an edge or a node of the finite element mesh. The nodes belonging to the edge where the crack ends must not be enriched, in order to verify that the crack ends, i.e. there is no jump on

displacement at the tip of the crack. The same applies for a node if the crack tip is not located on an edge but on a node.

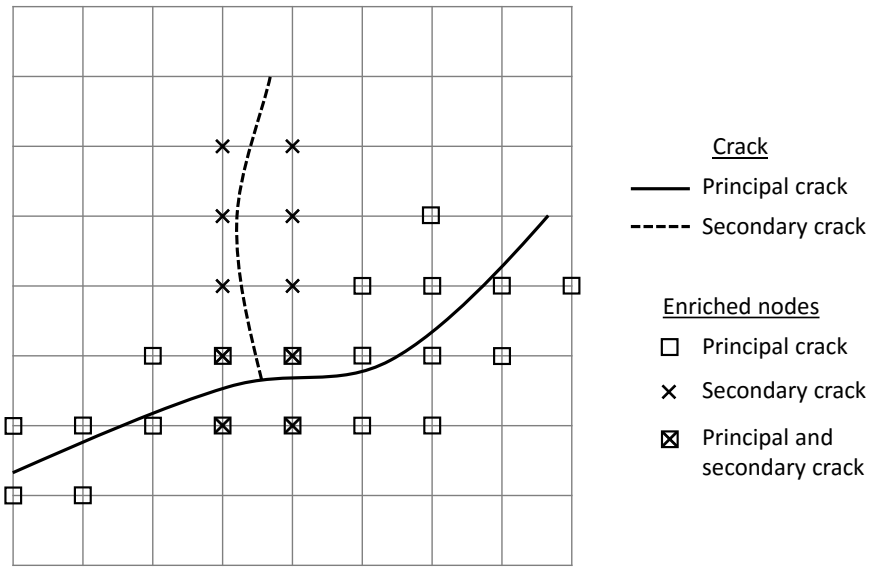

Figure 3.15: Example of the X-FEM enrichment for an arbitrary branched crack

3.4 Numerical example of crack branching

A 2D elastic problem on a square domain under imposed displacements has been solved in order to show the capabilities of the X-FEM enrichment proposed. The geometry of the problem is shown in Figure 3.16. The right edge of the domain is fixed and imposed displacements are applied in the upper and bottom edges. The geometry of the branched crack is introduced beforehand. Additionally a triangular law for the imposed displacements has been used in order to activate the discontinuity easily. The governing and constitutive equations are

$$\nabla \cdot \boldsymbol{\sigma} = \mathbf{0} \quad \text{in } \Omega \tag{3.5a}$$

$$\boldsymbol{u} = \boldsymbol{u}^* \quad \text{on } \Gamma_u \tag{3.5b}$$

$$\boldsymbol{\sigma} = \boldsymbol{C} : \boldsymbol{\varepsilon} \tag{3.5c}$$

$$\boldsymbol{\varepsilon} = \nabla^s \boldsymbol{u} \tag{3.5d}$$

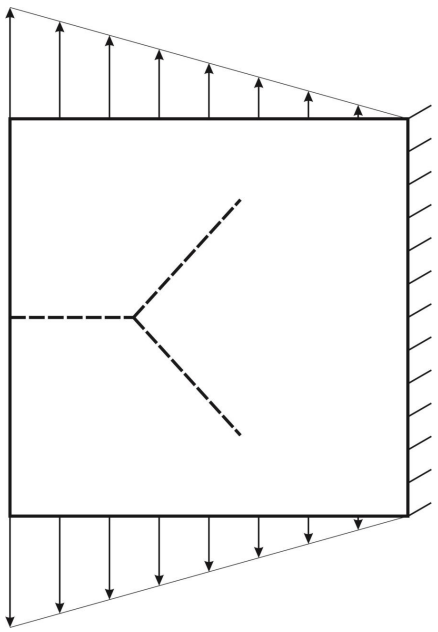

Figure 3.16: 2D elastic domain with a branched crack.

The domain is discretised in a mesh of 9×9 elements. Once branching occurs the two cracks cross the elements through their diagonal. This is done in this example to ease the computation of the stiffness matrix —which is obtained by dividing the element in subdomains where integration is performed by a gauss quadrature— but any arbitrary arrangement can be used.

The nodes of the finite element mesh are enriched as described in Section 3.3.3. The crack on the top is considered to be the principal crack, while the other is the secondary crack. The other way could as well be considered without affecting the solution of the problem. As shown in Figure 3.17, the corresponding nodes are enriched for the principal crack (orange) and for the secondary crack (yellow). The element with both cracks has all the nodes enriched by both discontinuities (grey). The sign functions are defined in concordance. The sign function ψ_p takes the value -1 above the principal crack and $+1$ below, while function ψ_s takes -1 above the secondary crack and $+1$ below.

The numerical solution to this elastic problem using the X-FEM enrichment allows to explicitly represent the branched crack by showing a discontinuity in displacements. See Figure 3.18, where elements are painted in red and black for illustrative purposes.

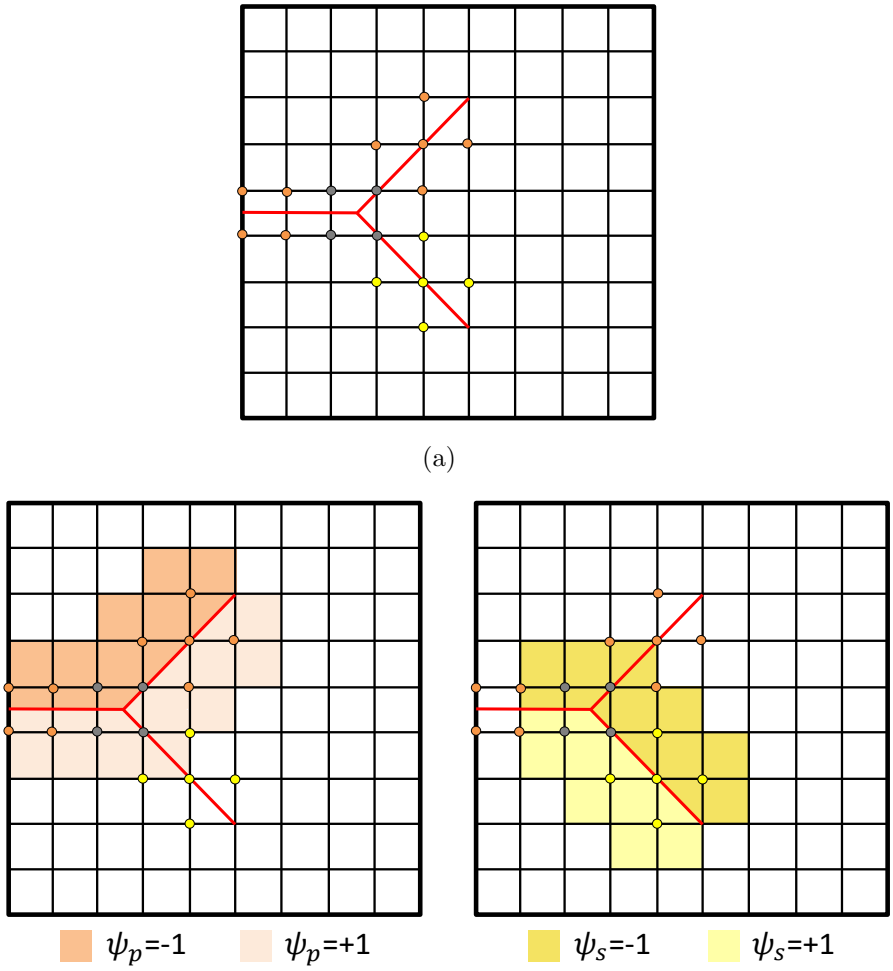

(a)

(b)

(c)

Figure 3.17: (a) Enrichment of the mesh, (b) value of ψ_p in the enriched elements by Γ_p and (c) value of ψ_s in the enriched elements by Γ_s.

The branched crack opens as expected and the symmetry reflects that the hierarchy used to define the principal and the secondary crack does not affect the solution. Indeed, the enhanced nodal values $\mathbf{u}_p$ and $\mathbf{u}_s$ take symmetrically the same value and the opening of the crack is equal distributed among $\mathbf{u}_p$ and $\mathbf{u}_s$.

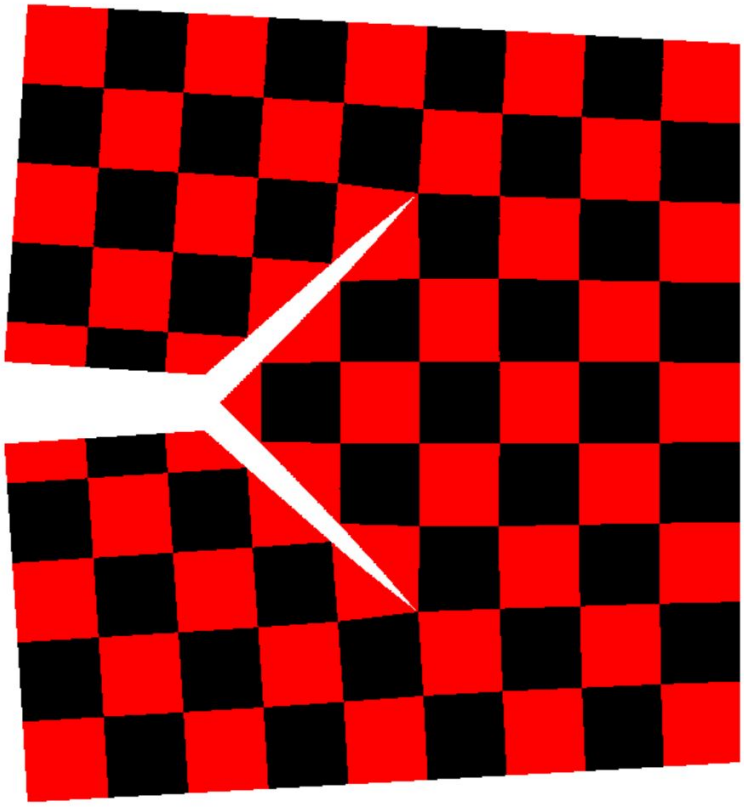

Figure 3.18: Opening of a branched crack in an elastic bulk.

Chapter 4

Continuous-discontinuous damage model for crack branching

In this chapter the continuous-discontinuous strategy used for the simulation of quasi-brittle failure is presented. Special emphasis is placed on the introduction of crack branching in the model.

4.1 Introduction

In damage mechanics, regularised damage models (both, integral-type and gradient-type formulations) may be used to describe the early stages of the failure process, but fail to introduce displacement discontinuities. Hence, these formulations based on continuous models are not useful when an explicit representation of cracks is necessary, such as in modelling fracking.

In fracture mechanics, discontinuous models are used for modelling the last stages of the failure process, where cracks must be explicitly introduced. However, this approach does not describe damage inception and damage propagation.

The best way to tackle the problem is by combining both theories. If a continuous-discontinuous approach is used, the inception and propagation of damage is described by a continuous model (damage mechanics), while cracks are introduced by a discontinuous model (fracture mechanics). The continuous bulk is regularised by means of

a gradient-enhanced damage model based on smoothed displacements. As soon as the damage parameter is close or equal to a critical value (D_{crit}) a crack is introduced by means of the eXtended Finite Element Method (X-FEM). More specifically, a traction-free crack or a cohesive crack (if $D_{\text{crit}} < 1$) can be included. A geometrical approach based on the medial axis is used to determine the crack path. Once the crack is introduced a continuous-discontinuous model —which couples the gradient-enhanced damage model with the X-FEM— is used.

The main purpose of this chapter is to extend the continuous-discontinuous strategy to its use for modelling crack branching. The continuous-discontinuous model developed by Tamayo-Mas and Rodríguez-Ferran (2014) for one propagating crack has been used, making adequate changes to introduce crack branching.

The structure of the chapter is as follows. In Section 4.2 the gradient-enhanced damage model is reviewed, placing special attention on the boundary conditions for non-local displacements introduced by this model. Section 4.3 deals with the extension of the continuous-discontinuous approach with the gradient-enhanced damage model. Finally, in Section 4.4 we present the geometrical approach used for tracking crack path.

4.2 Gradient-enhanced damage model

In order to describe the first stages of the failure process —damage inception and growth— a non-local damage model is used. Non-local damage models are used in numerical simulations of quasi-brittle failure to control strain localisation and to overcome the pathological mesh-dependence of local models. Non-locality is introduced by means of integral-type or gradient-type regularised formulations, where a certain variable is replaced by its non-local counterpart. Typically, an internal state variable, such as Y, is selected to introduce non-locality. In this thesis, a gradient-enriched formulation is used to regularise softening. Specifically, the non-local damage model based on non-local displacements developed by Rodríguez-Ferran et al. (2005) is used.

In the implicit gradient-enhanced continuum model based on smoothed displacements, non-locality is introduced at the level of displacements. Thus, two different displacement fields coexist: (a) the standard or local displacement field $\boldsymbol{u}$ and (b) the gradient-enriched displacement field $\widetilde{\boldsymbol{u}}$.

The gradient-enriched displacement field is the solution of a partial differential equation with $\boldsymbol{u}$ as the source term. Analogously to the diffusion-reaction equation

$$\widetilde{Y}(\boldsymbol{x}) - \ell^2 \nabla^2 \widetilde{Y}(\boldsymbol{x}) = Y(\boldsymbol{x}) \tag{4.1}$$

used in standard gradient-enhanced damage models —where the state variable Y is selected to introduce non-locality and ℓ is the characteristic length parameter which drives diffusion— here the regularisation PDE is

$$\widetilde{\boldsymbol{u}}(\boldsymbol{x}) - \ell^2 \nabla^2 \widetilde{\boldsymbol{u}}(\boldsymbol{x}) = \boldsymbol{u}(\boldsymbol{x}) \tag{4.2}$$

Therefore, the key idea of this formulation is to use this regularised displacement field —instead of the regularised internal variable $\widetilde{Y}$— to introduce non-locality, see Table 4.1 for details.

Hence, the non-local damage model used consists of the following equations, summarized in Table 4.1:

- The relationship between Cauchy stresses $\boldsymbol{\sigma}$ and small strains $\boldsymbol{\varepsilon}$ —the symmetrised gradient of displacements $\boldsymbol{u}$, Equation (4.3b)—, where the loss of stiffness is described by means of a scalar damage parameter D which ranges from 0 to 1, Equation (4.3a).
- The definition of a non-local state variable $\widetilde{Y}$, Equation (4.3e), as a function of the smoothed strains $\widetilde{\boldsymbol{\varepsilon}}$ —the symmetrised gradient of smoothed displacements $\widetilde{\boldsymbol{u}}$, Equation (4.3d), obtained from the regularisation PDE (4.3c).
- A damage evolution law, where the non-local state variable $\widetilde{Y}$ drives the evolution of the damage parameter D, Equation (4.3f).

This implicit gradient-enhanced continuum model based on smoothed displacement is used to describe the early stages of failure, before damage reaches a critical value D_{crit} and a crack is introduced.

4.2.1 Boundary conditions for non-local displacements

Analogously to standard gradient-enriched formulation —where boundary conditions for the non-local state variable $\widetilde{Y}$ are required— in the implicit gradient-enhanced damage model boundary conditions are necessary for non-local displacements, see

Constitutive equation	$\boldsymbol{\sigma} = (1 - D)\,\boldsymbol{C} : \boldsymbol{\varepsilon}$	(4.3a)
Strains	$\boldsymbol{\varepsilon} = \nabla^s \boldsymbol{u}$	(4.3b)
Smoothed displacements	$\widetilde{\boldsymbol{u}} - \ell^2 \nabla^2 \widetilde{\boldsymbol{u}} = \boldsymbol{u}$	(4.3c)
Smoothed strains	$\widetilde{\boldsymbol{\varepsilon}} = \nabla^s \widetilde{\boldsymbol{u}}$	(4.3d)
Smoothed state variable	$\widetilde{Y} = Y\left(\widetilde{\boldsymbol{\varepsilon}}\right)$	(4.3e)
Damage evolution	$D = D(\widetilde{Y})$	(4.3f)

Table 4.1: Gradient-enhanced damage model based on smoothed displacements.

Equation (4.2). As suggested by Tamayo-Mas (2013), combined boundary conditions are used for non-local displacements. That is, to prescribe Dirichlet boundary conditions for the normal component of the displacement field while non-homogeneous Neumann boundary conditions are imposed for the tangential components,

$$\left.\begin{aligned} \widetilde{\boldsymbol{u}} \cdot \boldsymbol{n} &= \boldsymbol{u} \cdot \boldsymbol{n} \\ \nabla\left(\widetilde{\boldsymbol{u}} \cdot \boldsymbol{\tau}\right) \cdot \boldsymbol{n} &= \nabla\left(\boldsymbol{u} \cdot \boldsymbol{\tau}\right) \cdot \boldsymbol{n} \end{aligned}\right\} \text{on } \partial\Omega \tag{4.4}$$

where $\boldsymbol{n}$ denotes the outward unit normal to Ω and $\boldsymbol{\tau}$ is the tangent vector such that $\{\boldsymbol{n}, \boldsymbol{\tau}\}$ form an orthonormal basis for $\mathbb{R}^2$.

Combined boundary conditions have been shown by Tamayo-Mas and Rodríguez-Ferran (2012) to be a good alternative to other types of boundary conditions such as Dirichlet, homogeneous Neumann and non-homogeneous Neumann boundary conditions. Using combined boundary conditions, the material response remains local along the normal direction at the boundary and preservation of volume is ensured, as opposed to homogeneous and non-homogeneous Neumann Boundary conditions. Dirichlet boundary conditions impose that the local and non-local displacement coincide along the domain boundary, leading to a local response in the boundary. This may not allow displacement smoothing along the boundary, which can be negative when localisation starts on the boundary. Combined boundary conditions solve this problem by ensuring that the displacement is smooth along the boundaries.

4.3 Continuous-discontinuous approach with a gradient-enhanced damage model

To simulate the last stages of the failure process —i.e. when macrocracks appear—, the implicit gradient-enhanced model based on smoothed displacements is coupled with propagating cracks. In this final stage of the process, the bulk Ω is bounded by $\Gamma = \Gamma_u \cup \Gamma_t \cup \Gamma_p \cup \Gamma_s$, as shown in Figure 4.1. Prescribed displacements are imposed on Γ_u, while tractions are imposed on Γ_t. The boundaries of the branched crack are represented by boundaries Γ_p and Γ_s. In this chapter, Γ_p represents the principal crack which branches into two cracks. One of the two cracks will be considered to be the continuation of the principal crack, Γ_p, while the other will be identified as secondary crack, Γ_s.

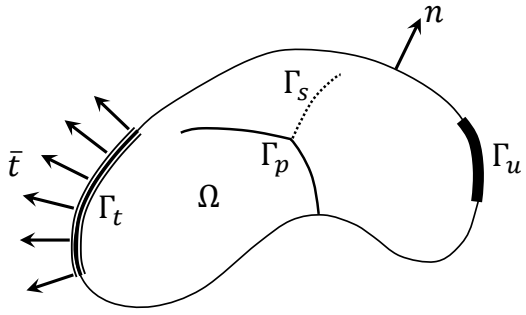

Figure 4.1: Notations for a body with two cracks subjected to loads and imposed displacements.

The key idea of this combined strategy is to characterise the local and non-local displacement fields by means of the X-FEM, see Belytschko and Black (1999) and Moës et al. (1999). Indeed, with the X-FEM enrichment proposed in Chapter 3, $\boldsymbol{u}$ and $\widetilde{\boldsymbol{u}}$ can be decomposed as

$$\boldsymbol{u}(\boldsymbol{x}) = \boldsymbol{u}_c(\boldsymbol{x}) + \psi_p(\boldsymbol{x})\,\boldsymbol{u}_p(\boldsymbol{x}) + \psi_s(\boldsymbol{x})\,\boldsymbol{u}_s(\boldsymbol{x}) \tag{4.5a}$$

$$\widetilde{\boldsymbol{u}}(\boldsymbol{x}) = \widetilde{\boldsymbol{u}}_c(\boldsymbol{x}) + \psi_p(\boldsymbol{x})\,\widetilde{\boldsymbol{u}}_p(\boldsymbol{x}) + \psi_s(\boldsymbol{x})\,\widetilde{\boldsymbol{u}}_s(\boldsymbol{x}) \tag{4.5b}$$

where $\boldsymbol{u}_i$, $\widetilde{\boldsymbol{u}}_i$ $(i = c, p, s)$ are continuous fields in Ω and ψ_p, ψ_s are the sign functions centred at discontinuities Γ_p and Γ_s—equals $+1$ at one side of the discontinuity and equals -1 at the other one. If the body Ω is not entirely crossed by the discontinuities Γ_p and Γ_s, then ψ_p and ψ_s are ambiguously defined. Nevertheless, as discussed in Chapter 3 this ambiguity disappears when the domain is discretised and the value

of functions ψ_p and ψ_s is only necessary in the elements with at least one enriched node.

The continuous parts $\boldsymbol{u}_c$ and $\widetilde{\boldsymbol{u}}_c$ correspond to the displacement field without any crack, while the additional discontinuous fields $\psi_p\boldsymbol{u}_p$ and $\psi_p\widetilde{\boldsymbol{u}}_p$ model the principal crack and $\psi_s\boldsymbol{u}_s$ and $\psi_s\widetilde{\boldsymbol{u}}_s$ model the secondary crack. Here, a branched crack has been considered leading to the introduction of two additional displacement fields $\boldsymbol{u}_p$ and $\boldsymbol{u}_s$, since the purpose of this work is to model crack branching. Indeed, when only the principal crack exists and branching has not yet occur, the terms in Equation (4.5) associated to $\boldsymbol{u}_s$ and $\widetilde{\boldsymbol{u}}_s$ disappear.

Note that in Equation (4.5), both mechanical and smoothed displacements are discontinuous. Being smoothed displacements $\widetilde{\boldsymbol{u}}$ discontinuous is a natural choice. Indeed, if we consider the regularisation PDE (4.2) with $\ell = 0$, the expected solution is $\boldsymbol{u} = \widetilde{\boldsymbol{u}}$. Therefore, given a discontinuous displacement field $\boldsymbol{u}$ the regularised displacement field $\widetilde{\boldsymbol{u}}$ must also be discontinuous.

4.3.1 Governing equations

The strong form of the equilibrium equation and boundary conditions for the body $\bar{\Omega} = \Omega \cup \Gamma$ without body forces is given by

$$\nabla \cdot \boldsymbol{\sigma} = \mathbf{0} \quad \text{in } \Omega \tag{4.6a}$$

$$\boldsymbol{\sigma} \cdot \boldsymbol{n} = \bar{\boldsymbol{t}} \quad \text{on } \Gamma_t \tag{4.6b}$$

$$\boldsymbol{\sigma} \cdot \boldsymbol{n} = \mathbf{0} \quad \text{on } \Gamma_d \cup \Gamma_s \tag{4.6c}$$

$$\boldsymbol{u} = \boldsymbol{u}^* \quad \text{on } \Gamma_u \tag{4.6d}$$

where $\boldsymbol{\sigma}$ is the Cauchy stress tensor, $\boldsymbol{n}$ is the outward unit normal to the body, $\bar{\boldsymbol{t}}$ is the traction on the Neumann boundary and $\boldsymbol{u}^*$ is a prescribed displacement on the Dirichlet boundary. Note that non-cohesive cracks are used since the right-hand-side term of Equation (4.6c) is 0. Cohesive cracks may be introduced as explained in Appendix B. Non-cohesive cracks are often introduced when the damage parameter is close to one in order to be energetically consistent.

In this continuous-discontinuous approach, the regularisation PDE (4.2) is employed to incorporate non-locality. Since now the displacement field is composed, not only by $\boldsymbol{u}_c$, but also by $\boldsymbol{u}_p$ and $\boldsymbol{u}_s$, the boundary conditions for the regularisation PDE described in Equation (4.4) must be extended:

$$\left.\begin{array}{c}(\widetilde{\boldsymbol{u}}_c+\psi_p\widetilde{\boldsymbol{u}}_p+\psi_s\widetilde{\boldsymbol{u}}_s)\cdot\boldsymbol{n}=(\boldsymbol{u}_c+\psi_p\boldsymbol{u}_p+\psi_s\boldsymbol{u}_s)\cdot\boldsymbol{n}\\ \nabla\left((\widetilde{\boldsymbol{u}}_c+\psi_p\widetilde{\boldsymbol{u}}_p+\psi_s\widetilde{\boldsymbol{u}}_s)\cdot\boldsymbol{\tau}\right)\cdot\boldsymbol{n}=\nabla\left((\boldsymbol{u}_c+\psi_p\boldsymbol{u}_p+\psi_s\boldsymbol{u}_s)\cdot\boldsymbol{\tau}\right)\cdot\boldsymbol{n}\end{array}\right\}\text{on }\Gamma \tag{4.7}$$

However, these boundary conditions may be simplified in the finite element discretisation. In the elements enriched by only one crack, the Dirichlet boundary condition of the continuous ($\boldsymbol{u}_c$) and discontinuous ($\boldsymbol{u}_p$) components of the displacement field are uncoupled by the fact that at one side of the crack surface (ψ_p=+1) reads

$$(\widetilde{\boldsymbol{u}}_c+\widetilde{\boldsymbol{u}}_p)\cdot\boldsymbol{n}=(\boldsymbol{u}_c+\boldsymbol{u}_p)\cdot\boldsymbol{n} \tag{4.8}$$

while at the other side (ψ_p=-1) reads

$$(\widetilde{\boldsymbol{u}}_c-\widetilde{\boldsymbol{u}}_p)\cdot\boldsymbol{n}=(\boldsymbol{u}_c-\boldsymbol{u}_p)\cdot\boldsymbol{n} \tag{4.9}$$

Adding equations (4.8) and (4.9) it results that the Dirichlet boundary condition from Equation (4.7) can be simplified to

$$\widetilde{\boldsymbol{u}}_c\cdot\boldsymbol{n} = \boldsymbol{u}_c\cdot\boldsymbol{n} \tag{4.10a}$$
$$\psi_p\widetilde{\boldsymbol{u}}_p\cdot\boldsymbol{n} = \psi_p\boldsymbol{u}_p\cdot\boldsymbol{n} \tag{4.10b}$$

Analogoulsy for the elements containing only nodes enriched by the secondary crack:

$$\widetilde{\boldsymbol{u}}_c\cdot\boldsymbol{n} = \boldsymbol{u}_c\cdot\boldsymbol{n} \tag{4.11a}$$
$$\psi_s\widetilde{\boldsymbol{u}}_s\cdot\boldsymbol{n} = \psi_s\boldsymbol{u}_s\cdot\boldsymbol{n} \tag{4.11b}$$

For the cracked finite elements containing both the principal and the secondary crack, this uncoupling is not possible. However, given the fact that there are only a few elements with two cracks and that the damage is very high in these elements, it is not a critical issue uncoupling the Dirichlet boundary conditions for the regularisation PDE:

$$\widetilde{\boldsymbol{u}}_c\cdot\boldsymbol{n} = \boldsymbol{u}_c\cdot\boldsymbol{n} \tag{4.12a}$$
$$\psi_p\widetilde{\boldsymbol{u}}_p\cdot\boldsymbol{n} = \psi_p\boldsymbol{u}_p\cdot\boldsymbol{n} \tag{4.12b}$$
$$\psi_s\widetilde{\boldsymbol{u}}_s\cdot\boldsymbol{n} = \psi_s\boldsymbol{u}_s\cdot\boldsymbol{n} \tag{4.12c}$$

Analogously, the tangential component of the boundary conditions can also be simplified, leading to the following boundary conditions for smoothed displacements $\widetilde{\boldsymbol{u}}$

$$\left.\begin{aligned} \widetilde{\boldsymbol{u}}_i \cdot \boldsymbol{n} &= \boldsymbol{u}_i \cdot \boldsymbol{n} \\ \nabla\left(\widetilde{\boldsymbol{u}}_i \cdot \tau\right) \cdot \boldsymbol{n} &= \nabla\left(\boldsymbol{u}_i \cdot \tau\right) \cdot \boldsymbol{n} \end{aligned}\right\} \text{on } \Gamma \tag{4.13}$$

where $i = c, p, s$.

Thus, the problem is governed by the equilibrium equations with the corresponding boundary conditions, Equation (4.6), plus the regularisation equation (4.2) with the corresponding boundary conditions for smoothed displacements, Equation (4.13).

Both equations —equilibrium and regularisation equations — are first expressed in a weak form to be later linearised. The weak form of the equilibrium equation (4.6) reads

$$\int_\Omega \nabla^s \boldsymbol{\omega}_c : \boldsymbol{\sigma}\, \mathrm{d}\Omega = \int_{\Gamma_t} \boldsymbol{\omega}_c \cdot \bar{\boldsymbol{t}}\, \mathrm{d}\Gamma \quad \forall \boldsymbol{\omega}_c \in H^1(\Omega) \tag{4.14a}$$

$$\int_\Omega \psi_p \nabla^s \boldsymbol{\omega}_p : \boldsymbol{\sigma}\, \mathrm{d}\Omega = \int_{\Gamma_t} \psi_p \boldsymbol{\omega}_p \cdot \bar{\boldsymbol{t}}\, \mathrm{d}\Gamma \quad \forall \boldsymbol{\omega}_p \in H^1(\Omega) \tag{4.14b}$$

$$\int_\Omega \psi_s \nabla^s \boldsymbol{\omega}_s : \boldsymbol{\sigma}\, \mathrm{d}\Omega = \int_{\Gamma_t} \psi_s \boldsymbol{\omega}_s \cdot \bar{\boldsymbol{t}}\, \mathrm{d}\Gamma \quad \forall \boldsymbol{\omega}_s \in H^1(\Omega) \tag{4.14c}$$

whereas the regularisation equation leads to

$$\begin{aligned} &\int_\Omega \widetilde{\boldsymbol{\omega}}_c \cdot \widetilde{\boldsymbol{u}}\, \mathrm{d}\Omega + \ell^2 \int_\Omega \nabla\widetilde{\boldsymbol{\omega}}_c : \left(\nabla\widetilde{\boldsymbol{u}}_c + \psi_p \nabla\widetilde{\boldsymbol{u}}_p + \psi_s \nabla\widetilde{\boldsymbol{u}}_s\right) \mathrm{d}\Omega = \int_\Omega \widetilde{\boldsymbol{\omega}}_c \cdot \boldsymbol{u}\, \mathrm{d}\Omega + \\ +\ &\ell^2 \int_\Gamma \left(\widetilde{\boldsymbol{\omega}}_c \cdot \boldsymbol{\tau}\right) \cdot \left[\nabla\left(\boldsymbol{u}_c \cdot \boldsymbol{t}_1\right) \cdot \boldsymbol{n} + \psi_p \nabla\left(\boldsymbol{u}_p \cdot \boldsymbol{\tau}\right) \cdot \boldsymbol{n} + \psi_s \nabla\left(\boldsymbol{u}_s \cdot \boldsymbol{\tau}\right) \cdot \boldsymbol{n}\right] \mathrm{d}\Gamma \end{aligned} \tag{4.15a}$$

$$\begin{aligned} &\int_\Omega \psi_p \widetilde{\boldsymbol{\omega}}_p \cdot \widetilde{\boldsymbol{u}}\, \mathrm{d}\Omega + \ell^2 \int_\Omega \nabla\widetilde{\boldsymbol{\omega}}_p : \left(\psi_p \nabla\widetilde{\boldsymbol{u}}_c + \nabla\widetilde{\boldsymbol{u}}_p + \psi_b \nabla\widetilde{\boldsymbol{u}}_s\right) \mathrm{d}\Omega = \int_\Omega \psi_p \widetilde{\boldsymbol{\omega}}_p \cdot \boldsymbol{u}\, \mathrm{d}\Omega + \\ +\ &\ell^2 \int_\Gamma \left(\widetilde{\boldsymbol{\omega}}_p \cdot \boldsymbol{\tau}\right) \cdot \left[\psi_p \nabla\left(\boldsymbol{u}_c \cdot \boldsymbol{\tau}\right) \cdot \boldsymbol{n} + \nabla\left(\boldsymbol{u}_p \cdot \boldsymbol{\tau}\right) \cdot \boldsymbol{n} + \psi_b \nabla\left(\boldsymbol{u}_s \cdot \boldsymbol{\tau}\right) \cdot \boldsymbol{n}\right] \mathrm{d}\Gamma \end{aligned} \tag{4.15b}$$

$$\begin{aligned} &\int_\Omega \psi_s \widetilde{\boldsymbol{\omega}}_s \cdot \widetilde{\boldsymbol{u}}\, \mathrm{d}\Omega + \ell^2 \int_\Omega \nabla\widetilde{\boldsymbol{\omega}}_s : \left(\psi_s \nabla\widetilde{\boldsymbol{u}}_c + \psi_b \nabla\widetilde{\boldsymbol{u}}_p + \nabla\widetilde{\boldsymbol{u}}_s\right) \mathrm{d}\Omega = \int_\Omega \psi_s \widetilde{\boldsymbol{\omega}}_s \cdot \boldsymbol{u}\, \mathrm{d}\Omega + \\ +\ &\ell^2 \int_\Gamma \left(\widetilde{\boldsymbol{\omega}}_s \cdot \boldsymbol{\tau}\right) \cdot \left[\psi_s \nabla\left(\boldsymbol{u}_c \cdot \boldsymbol{\tau}\right) \cdot \boldsymbol{n} + \psi_b \nabla\left(\boldsymbol{u}_p \cdot \boldsymbol{\tau}\right) \cdot \boldsymbol{n} + \nabla\left(\boldsymbol{u}_s \cdot \boldsymbol{\tau}\right) \cdot \boldsymbol{n}\right] \mathrm{d}\Gamma \end{aligned} \tag{4.15c}$$

where $\boldsymbol{\omega} = \boldsymbol{\omega}_c + \psi_p \boldsymbol{\omega}_p + \psi_s \boldsymbol{\omega}_s$ and $\widetilde{\boldsymbol{\omega}} = \widetilde{\boldsymbol{\omega}}_c + \psi_p \widetilde{\boldsymbol{\omega}}_p + \psi_s \widetilde{\boldsymbol{\omega}}_s$ are the test functions of the space of admissible —local and smoothed, respectively— displacement variations. It

is noted that a new sign function ψ_b appears, which is defined as $\psi_b = \psi_p\psi_s$, see Appendix A for details. Additionally the following conditions have been used: (a) $\psi_p\psi_p = 1$ and (b) $\psi_s\psi_s = 1$. The sign functions ψ_p, ψ_s and ψ_b for a body Ω are presented in Figure 4.2.

For details of Equations (4.14) and (4.15) see Appendix A.

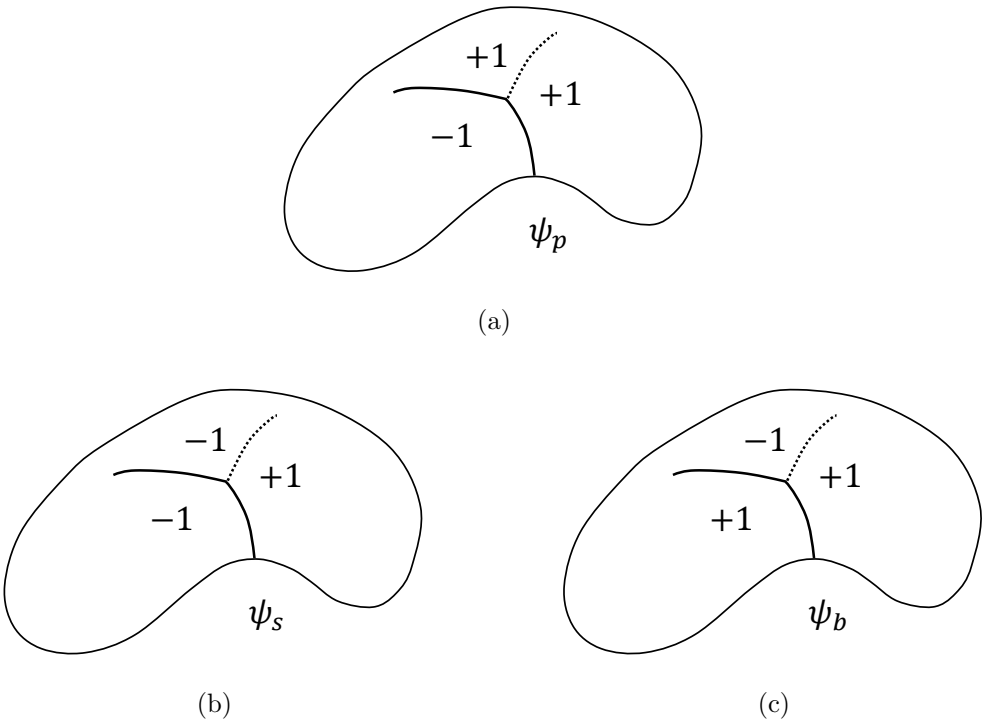

Figure 4.2: Definition of (a) ψ_p, (b) ψ_s and (c) ψ_b, on Ω.

4.3.2 Linearisation and consistent tangent matrix

Regarding the finite element discretisation, local and non-local displacements read, in the domain of an element with enhanced nodes for the principal and secondary crack,

$$\boldsymbol{u}(\boldsymbol{x}) \simeq \boldsymbol{u}^h(\boldsymbol{x}) = \mathbf{N}(\boldsymbol{x})\mathbf{u}_c + \psi_p(\boldsymbol{x})\mathbf{N}(\boldsymbol{x})\mathbf{u}_p + \psi_s(\boldsymbol{x})\mathbf{N}(\boldsymbol{x})\mathbf{u}_s \tag{4.16a}$$

$$\widetilde{\boldsymbol{u}}(\boldsymbol{x}) \simeq \widetilde{\boldsymbol{u}}^h(\boldsymbol{x}) = \mathbf{N}(\boldsymbol{x})\widetilde{\mathbf{u}}_c + \psi_p(\boldsymbol{x})\mathbf{N}(\boldsymbol{x})\widetilde{\mathbf{u}}_p + \psi_s(\boldsymbol{x})\mathbf{N}(\boldsymbol{x})\widetilde{\mathbf{u}}_s \tag{4.16b}$$

where $\mathbf{N}$ is the matrix of standard finite element shape functions, $\mathbf{u}_c$, $\widetilde{\mathbf{u}}_c$ are the basic nodal degrees of freedom, $\mathbf{u}_p$, $\widetilde{\mathbf{u}}_p$ are the enhanced ones due to the principal crack

and $\mathbf{u}_s$, $\widetilde{\mathbf{u}}_s$ are the enhanced ones due to the secondary crack.

Indeed, for elements with only enhanced nodes by the principal crack, the terms $\psi_s(\boldsymbol{x})\mathbf{N}(\boldsymbol{x})\mathbf{u}_s$ and $\psi_s(\boldsymbol{x})\mathbf{N}(\boldsymbol{x})\widetilde{\mathbf{u}}_s$ disappear from Equation (4.16). Analogously, for elements with only enhanced nodes by the secondary crack, the terms $\psi_p(\boldsymbol{x})\mathbf{N}(\boldsymbol{x})\mathbf{u}_p$ and $\psi_p(\boldsymbol{x})\mathbf{N}(\boldsymbol{x})\widetilde{\mathbf{u}}_p$ disappear.

According to the finite element discretisation of the local and non-local displacement, Equation (4.16), the equilibrium equation (4.14), leads to the discrete weak form

$$\int_\Omega \mathbf{B}^T\boldsymbol{\sigma}\,\mathrm{d}\Omega = \int_{\Gamma_t} \mathbf{N}^T\bar{\boldsymbol{t}}\,\mathrm{d}\Gamma \tag{4.17a}$$

$$\int_\Omega \psi_p\mathbf{B}^T\boldsymbol{\sigma}\,\mathrm{d}\Omega = \int_{\Gamma_t} \psi_p\mathbf{N}^T\bar{\boldsymbol{t}}\,\mathrm{d}\Gamma \tag{4.17b}$$

$$\int_\Omega \psi_s\mathbf{B}^T\boldsymbol{\sigma}\,\mathrm{d}\Omega = \int_{\Gamma_t} \psi_s\mathbf{N}^T\bar{\boldsymbol{t}}\,\mathrm{d}\Gamma \tag{4.17c}$$

while the regularisation equation (4.15), leads to

$$\begin{aligned}(\mathbf{M}+\ell^2\mathbf{K}_{\mathrm{BC}})\mathbf{u}_c + (\mathbf{M}_{\psi_p}+\ell^2\mathbf{K}_{\psi_p,\mathrm{BC}})\mathbf{u}_p + (\mathbf{M}_{\psi_s}+\ell^2\mathbf{K}_{\psi_s,\mathrm{BC}})\mathbf{u}_s = \\ = (\mathbf{M}+\ell^2\mathbf{D})\widetilde{\mathbf{u}}_c + (\mathbf{M}_{\psi_p}+\ell^2\mathbf{D}_{\psi_p})\widetilde{\mathbf{u}}_p + (\mathbf{M}_{\psi_s}+\ell^2\mathbf{D}_{\psi_s})\widetilde{\mathbf{u}}_s\end{aligned} \tag{4.18a}$$

$$\begin{aligned}(\mathbf{M}_{\psi_p}+\ell^2\mathbf{K}_{\psi_p,\mathrm{BC}})\mathbf{u}_c + (\mathbf{M}+\ell^2\mathbf{K}_{\mathrm{BC}})\mathbf{u}_p + (\mathbf{M}_{\psi_b}+\ell^2\mathbf{K}_{\psi_b,\mathrm{BC}})\mathbf{u}_s = \\ = (\mathbf{M}_{\psi_p}+\ell^2\mathbf{D}_{\psi_p})\widetilde{\mathbf{u}}_c + (\mathbf{M}+\ell^2\mathbf{D})\widetilde{\mathbf{u}}_p + (\mathbf{M}_{\psi_b}+\ell^2\mathbf{D}_{\psi_b})\widetilde{\mathbf{u}}_s\end{aligned} \tag{4.18b}$$

$$\begin{aligned}(\mathbf{M}_{\psi_s}+\ell^2\mathbf{K}_{\psi_s,\mathrm{BC}})\mathbf{u}_c + (\mathbf{M}_{\psi_b}+\ell^2\mathbf{K}_{\psi_b,\mathrm{BC}})\mathbf{u}_p + (\mathbf{M}+\ell^2\mathbf{K}_{\mathrm{BC}})\mathbf{u}_s = \\ = (\mathbf{M}_{\psi_s}+\ell^2\mathbf{D}_{\psi_s})\widetilde{\mathbf{u}}_c + (\mathbf{M}_{\psi_b}+\ell^2\mathbf{D}_{\psi_b})\widetilde{\mathbf{u}}_p + (\mathbf{M}+\ell^2\mathbf{D})\widetilde{\mathbf{u}}_s\end{aligned} \tag{4.18c}$$

with matrices defined in Appendix B.

It should be noted that:

- Equation (4.17a) is the standard non-linear system of equilibrium equations, while Equation (4.17b) and Equation (4.17c) take into account the contribution of the principal and secondary cracks. The effect of the displacement discontinuity is taken into account by enforcing equilibrium of the enriched internal and external forces for each crack.

- From Equation (4.17) it may seem that the standard degrees of freedom and the enhanced degrees of freedom are uncopuled, but they are not. By the constitutive equation (see Table 4.1) $\boldsymbol{\sigma}$ depends on strains —which derivate from $\boldsymbol{u}$— and thus also on $\boldsymbol{u}_c$, $\boldsymbol{u}_p$ and $\boldsymbol{u}_s$.

- In Equation (4.18), $\mathbf{M}$ and $\mathbf{D}$ are the mass and diffusivity matrices. Then, matrices $\mathbf{M}_{\psi_p}$, $\mathbf{M}_{\psi_s}$and $\mathbf{M}_{\psi_b}$ can be understood as enriched mass matrices, while $\mathbf{D}_{\psi_p}$, $\mathbf{D}_{\psi_s}$ and $\mathbf{D}_{\psi_b}$ can be seen as enriched diffusivity matrices.

- Matrices $\mathbf{K}_{\mathrm{BC}}$, $\mathbf{K}_{\psi_p,\mathrm{BC}}$, $\mathbf{K}_{\psi_s,\mathrm{BC}}$ and $\mathbf{K}_{\psi_b,\mathrm{BC}}$ from Equation (4.18) take into account the tangential part of the combined boundary conditions for the regularisation PDE, see Appendix B.

- The addition of the secondary crack (i.e. crack branching) adds two equations, Equation (4.17c) and Equation (4.18c), to the system of equations resulting from the consideration of only the principal crack, which is composed by Equations (4.17a), (4.17b), (4.18a) and (4.18b). Additional terms also appear in these last four equations due to the introduction of a second crack.

Equations (4.17) and (4.18) are linearised in order to obtain the tangent matrix, see Equation (4.19) with matrices defined in Appendix B, needed to attain quadratic convergence in the Newton-Raphson method. Traditional quadrature rules, such as Gauss quadratures, are not adequate to obtain the matrices from Equation (4.19) because they fail to integrate discontinuous functions. Therefore, in order to obtain the tangent matrix, the elements crossed by a crack have been subdivided into subdomains with a continuous polynomial solution where a standard Gauss quadrature has been applied. See Appendix C for details.

$$
\mathbf{K}_{\text{tan}} = \begin{bmatrix}
\mathbf{K}_{\text{sec}} & \mathbf{K}_{\psi_p,\text{sec}} & \mathbf{K}_{\psi_s,\text{sec}} & \mathbf{K}_{\text{loc}} & \mathbf{K}_{\psi_p,\text{loc}} & \mathbf{K}_{\psi_s,\text{loc}} \\
\mathbf{K}_{\psi_p,\text{sec}} & \mathbf{K}_{\text{sec}} & \mathbf{K}_{\psi_b,\text{sec}} & \mathbf{K}_{\psi_p,\text{loc}} & \mathbf{K}_{\text{loc}} & \mathbf{K}_{\psi_b,\text{loc}} \\
\mathbf{K}_{\psi_s,\text{sec}} & \mathbf{K}_{\psi_b,\text{sec}} & \mathbf{K}_{\text{sec}} & \mathbf{K}_{\psi_s,\text{loc}} & \mathbf{K}_{\psi_b,\text{loc}} & \mathbf{K}_{\text{loc}} \\
-(\mathbf{M}+\ell^2\mathbf{K}_{\text{BC}}) & -(\mathbf{M}_{\psi_p}+\ell^2\mathbf{K}_{\psi_p,\text{BC}}) & -(\mathbf{M}_{\psi_s}+\ell^2\mathbf{K}_{\psi_s,\text{BC}}) & \mathbf{M}+\ell^2\mathbf{D} & \mathbf{M}_{\psi_p}+\ell^2\mathbf{D}_{\psi_p} & \mathbf{M}_{\psi_s}+\ell^2\mathbf{D}_{\psi_s} \\
-(\mathbf{M}_{\psi_p}+\ell^2\mathbf{K}_{\psi_p,\text{BC}}) & -(\mathbf{M}+\ell^2\mathbf{K}_{\text{BC}}) & -(\mathbf{M}_{\psi_b}+\ell^2\mathbf{K}_{\psi_b,\text{BC}}) & \mathbf{M}_{\psi_p}+\ell^2\mathbf{D}_{\psi_p} & \mathbf{M}+\ell^2\mathbf{D} & \mathbf{M}_{\psi_b}+\ell^2\mathbf{D}_{\psi_b} \\
-(\mathbf{M}_{\psi_s}+\ell^2\mathbf{K}_{\psi_s,\text{BC}}) & -(\mathbf{M}_{\psi_b}+\ell^2\mathbf{K}_{\psi_b,\text{BC}}) & -(\mathbf{M}+\ell^2\mathbf{K}_{\text{BC}}) & \mathbf{M}_{\psi_s}+\ell^2\mathbf{D}_{\psi_s} & \mathbf{M}_{\psi_b}+\ell^2\mathbf{D}_{\psi_b} & \mathbf{M}+\ell^2\mathbf{D}
\end{bmatrix}, \tag{4.19}
$$

4.4 Identification of crack path

When switching from the continuous to the discontinuous approach it is essential to identify the location of the crack. We cannot introduce displacement discontinuities without knowing a priori the crack path and consequently the value of sign functions ψ_p and ψ_s.

Different approaches can be found in the literature: (a) mechanical and (b) geometric criteria. From the mechanical point of view, one way to locate a crack is by assuming the crack path to be perpendicular to the direction of maximum principal stress. With a geometric criterion the medial axis (MA) of the damaged zone can be computed.

4.4.1 Medial axis

In this thesis the medial axis, a geometrical criterion, is used to determine the crack path. The basic idea of this approach is to determine the crack path from the damage profile. The medial axis of a domain Ω is defined as the loci of centers of bi-tangent interior balls, see Figure 4.3, and it can be conceived as its skeleton.

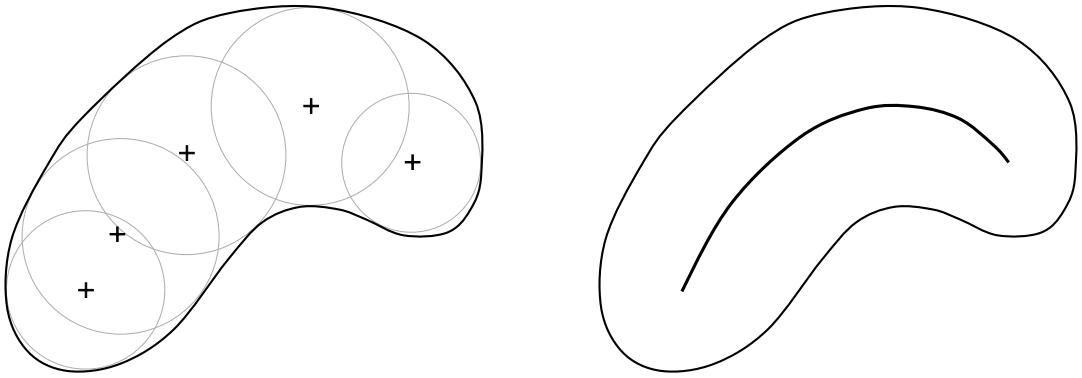

(a) (b)

Figure 4.3: (a) Given a boundary the bi-tangent interior balls are computed and (b) the MA is obtained by joining the centers.

The main drawback of this geometric tool is that it is very sensitive to minor perturbations of the object's boundary, leading to the appearance of spurious branches, see Figure 4.4 obtained from Tamayo-Mas and Rodríguez-Ferran (2015). In this the-

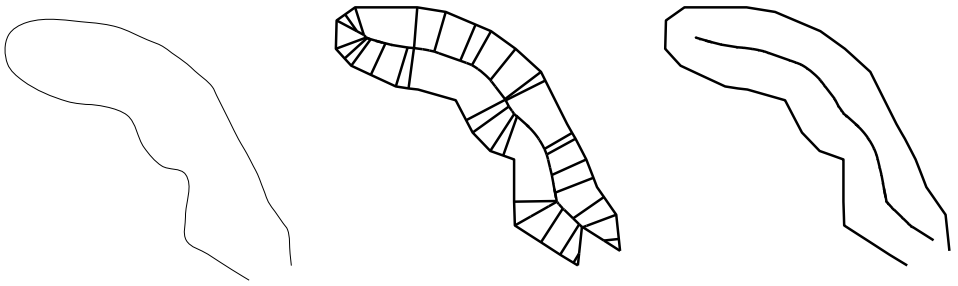

(a) (b) (c)

Figure 4.4: (a) Given a domain Ω (b) the MA is obtained including spurious branches. If the $\theta-$SMA is used, these branches are removed. the bi-tangent interior balls are computed. Source: Tamayo-Mas and Rodríguez-Ferran (2015).

sis the $\theta-$simplified medial axis, a stable version of the medial axis, see Foskey et al. (2003), is used. In order to avoid the spurious branches, this stable version takes into account the separation angle of each interior ball used in the computation of the medial axis.

The separation angle, $S(P) \in [0, \pi]$, of an interior ball with center at point P is defined as

$$S(P) = \angle P_1 P P_2, \tag{4.20}$$

where P_1 and P_2 are the tangent points of the interior ball with the boundary, see Figure 4.5. If the interior ball has more than two points of tangency, the separation angle is the largest angle between P and each pair of points of tangency

$$S(P) = \max_{P_1, P_2 \in T(P)} (\angle P_1 P P_2) \tag{4.21}$$

whith $T(P)$ the set of points of tangency of the interior ball with centre at P.

The stability of the $\theta-$simplified medial axis is given by the fact that a restriction on the points of the medial axis is introduced by the separation angle. Given an angle $\theta \in [0, \pi]$, the points with a separation angle lower than θ are removed. With the adequate selection of θ, the spurious branches —which are obtained from points whose separation angle is small— are removed.

Even if this modified version of the medial axis allows to suppress spurious branches, it captures crack branching, as shown in Chapter 5.

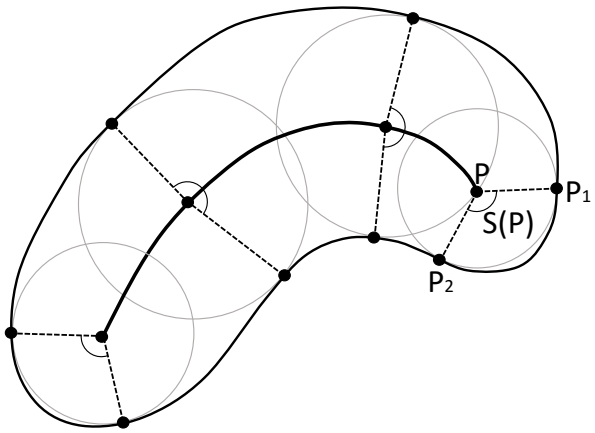

Figure 4.5: Definition of the separation angle $S(P)$.

4.4.2 Determining crack path by the $\theta-$simplified medial axis

The following steps are followed to determine crack path with the $\theta-$simplified medial axis:

- **Crack initiation**: it is assumed that the crack starts only from the boundary of the domain. A crack is introduced only when the damage parameter reaches a value of D_{crit} in an element on the boundary of the mesh.

- $\theta-$**SMA computation**: once the crack initiation is located, the crack path is computed by means of the $\theta-$simplified medial axis tool. A damage isoline $D(\boldsymbol{x}) = D^*$ is defined and the medial axis of this boundary is computed. Two key parameters must be defined in order to compute the $\theta-$SMA: the value of the isoline $D(\boldsymbol{x}) = D^*$ and the value of the separation angle θ.

- **Crack propagation**: once the $\theta-$SMA is computed different criteria can be used to decide which elements are cracked. On the one hand, the new enriched elements may be selected as the elements crossed by the computed $\theta-$SMA which go from the crack tip up to the first element not satisfying $D > D_{\text{crit}}$. On the other hand, we can establish the criterion that all the elements crossed by the computed $\theta-$SMA are enriched, thus concluding that the crack propagates at the same time the isoline does. Once an element is enriched, i.e. is considered to be cracked, the damage parameter is fixed to 1 for the rest of the simulation.

In order to compute the $\theta-$SMA, first the value of the damage isoline and the value of the separation angle must be set.

As discussed before, the medial axis is very sensitive with small variations in the boundary of the solid. Of course, different boundaries are obtained with different values of the damage isoline. However, thanks to the use of the stable version of the medial axis ($\theta-$SMA) and the use of a smooth damage field, the value of the isoline has not a great impact on the location of the crack. However, if we use the criterion that establishes that all the elements crossed by the $\theta-$SMA are cracked regardless of the value of the damage parameter, we must select a high value for the damage isoline because an element can be considered as cracked only if it has high damage.

The separation angle is the main parameter used to remove spurious cracks. The spurious branches appear with low values of θ and therefore a value high enough to capture only the main crack must be selected. Diferent examples for selecting this value are shown by Tamayo-Mas and Rodríguez-Ferran (2015).

Chapter 5

An application example

In this chapter, we present a numerical example to test the continuous-discontinuous model presented in Chapter 4 with the X-FEM enrichment presented in Chapter 3.

5.1 Introduction

A two-dimensional numerical example is used in order to illustrate the capabilities of the X-FEM to reproduce crack branching. This example consists of a square specimen under mode I fracture (or opening mode). Mode I fracture appears when a tensile stress is applied normal to the plane of a crack.

A square specimen is subjected to prescribed displacements u^* at the top and the bottom sides, see Figure 5.1. The right side is clamped in order to induce branching. The prescribed displacements are linearly distributed. In the left side, a region is weaken to break uniformity and cause localisation for damage inception. An alternative way to localise damage may be to introduce a small notch.

The geometric and material parameters of this setting are summarised in Table 5.1. Note that the Poisson's coefficient is set to ν =0.3 in order to produce crack branching. The weaken region is characterized by a reduction of Young's modulus, alternatively a lower damage threshold (Y_0) may also be used instead.

Note that the problem is similar to the elastic problem tested in Section 3.4. However, in this chapter the crack path is described by the damage field obtained

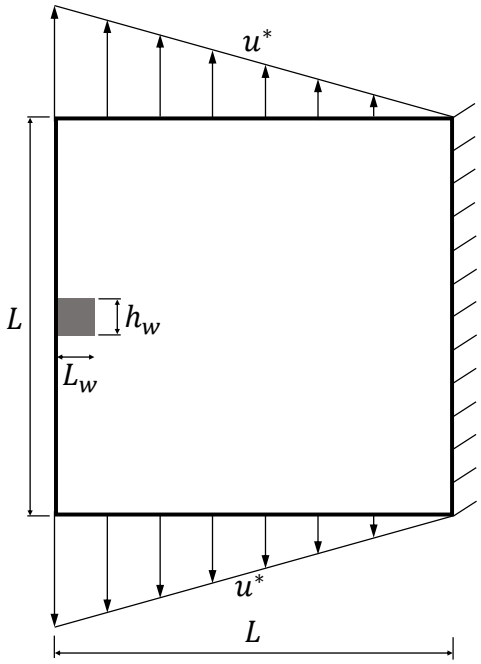

Figure 5.1: Square specimen under mode I loading conditions: problem statement.

from a non-local continuous damage model instead of being pre-defined by the user.

Meaning	**Symbol**	**Value**
Length of the specimen	L	10 cm
Length of the weaker part	L_W	1 cm
Width of the weaker part	h_W	1 finite element
Young's modulus	E	20 000 MPa
Young's modulus of the weaker part	E_W	2 000 MPa
Damage threshold	Y_0	10^{-4}
Final strain	Y_f	1.25×10^{-2}
Poisson's coefficient	ν	0.3

Table 5.1: Square specimen under mode I loading conditions: geometrical and material parameters.

5.2 Governing equations

The governing equations of this problem, as stated in Chapter 4, are the equilibrium equation (4.6) and the regularisation equation (4.2) with the corresponding boundary conditions, Equation (4.13). The gradient-enhanced damage model based on smoothed displacements is used, see Table 4.1.

To carry out this test a smoothed state variable function $\widetilde{Y} = Y\left(\widetilde{\varepsilon}\right)$ and a damage evolution law $D = D(\widetilde{Y})$ must be defined. The simplified Mazars model, see Mazars (1986), is used

$$Y = \sqrt{\sum_{i=1}^{3} \left(\max(0, \varepsilon_i)\right)^2} \tag{5.1}$$

where ε_i $(i = 1, 2, 3)$ are the principal strains. A linear damage evolution law is considered

$$D(Y) = \begin{cases} 0 & \text{if } Y < Y_0 \\ \frac{Y_f}{Y_f - Y_0}\left(1 - \frac{Y_0}{Y}\right) & \text{if } Y_0 < Y < Y_f \\ 1 & \text{if } Y_f < Y \end{cases} \tag{5.2}$$

where Y_0, Y_f are the damage initiation state variable and the final state variable respectively.

5.3 Numerical insights

The numerical example presented above is a non-linear problem, where non-linearity is introduced by damage (i.e. strain softening). The non-linear system of equations, which expresses static equilibrium and regularisation, is solved with an incremental-iterative scheme, based on the linearisation of the non-linear system of equations. In each load step n the prescribed displacement on the top and bottom sides of the domain is updated according to

$${}^{n+1}\boldsymbol{u} = {}^{n}\boldsymbol{u} + \boldsymbol{\delta u} \tag{5.3}$$

The full Newton-Raphson method is used to solve the non-linear system of equations in each load step. Thus, quadratic convergence is obtained. The prescribed displacement at iteration $k+1$ within the same load step n reads

$${}^{n}\boldsymbol{u}^{k+1} = {}^{n}\boldsymbol{u}^{k} + \boldsymbol{\delta u}^{k+1} \tag{5.4}$$

The iterative correction $\boldsymbol{\delta u}^{k+1}$ at each Newton-Raphson iteration is computed with the tangent matrix $\mathbf{K}_{\tan}$, obtained from the linearisation of the system, according to

$$\mathbf{K}_{\tan}({}^{n}\boldsymbol{u}^{k})\boldsymbol{\delta u}^{k+1} = -\boldsymbol{r}({}^{n}\boldsymbol{u}^{k}) \tag{5.5}$$

with $\boldsymbol{r}({}^{n}\boldsymbol{u}^{k})$ the residual vector at previous Newton-Raphson iteration.

The Lagrange-multiplier technique is chosen to impose boundary conditions for the equilibrium and regularisation equations. Then, the iterative correction $\boldsymbol{\delta u}^{k+1}$ in the full Newton-Raphson method is computed by solving the system of equations

$$\begin{bmatrix} \mathbf{K}_{\tan}({}^{n}\boldsymbol{u}^{k}) & \mathbf{A}^{T} \\ \mathbf{A} & \mathbf{0} \end{bmatrix} \begin{bmatrix} \boldsymbol{\delta u}^{k+1} \\ \boldsymbol{\delta \lambda}^{k+1} \end{bmatrix} = \begin{bmatrix} -\boldsymbol{r}({}^{n}\boldsymbol{u}^{k}, {}^{n}\boldsymbol{\lambda}^{k}) \\ 0 \end{bmatrix} \tag{5.6}$$

where the block matrices $\mathbf{A}$ and $\mathbf{A}^{T}$ account for the Dirichlet boundary constraints for both the equilibrium and the regularisation equations. See Appendix B for details.

Numerical integration is necessary to compute the tangent matrix $\mathbf{K}_{\tan}$. Traditional quadrature rules such as Gauss quadratures cannot integrate discontinuous functions, which appear with the introduction of a crack by means of X-FEM. An alternative integration rule based on the subdivision of cracked elements is used. Refer to Appendix C for details.

In incremental-iterative processes it is essential to use adaptive stepping. This tehcnique allows to adapt the step size depending on the results in the current step. The main idea of this method is to increase the step size when convergence is "easy" and reduce when it is "difficult", trying to attain convergence in a desired number of iterations. With this method, the step size in each iteration reads as

$$\Delta\alpha^{i+1} = \Delta\alpha^{i}\sqrt{n^{i}_{\text{des}}/n^{i}} \tag{5.7}$$

where $\Delta\alpha^{i}$, $\Delta\alpha^{i+1}$ are the step sizes in the current load step and next load step, respectively. The parameter n^{i}_{des} is the desired number of iterations in the next load step and n^{i} is the number of iterations of the current load step to obtain convergence.

5.4 Continuous model: damage inception and evolution

In the continuous approach, damage evolution is obtained by using the gradient-enhanced damage model with smoothed displacements. Results are shown in Figure 5.3. Damage inception occurs in the weakened region and propagates until the damaged bulk branches. At this point the damage continues to propagate for each of the two branches until they reach the top and bottom sides of the square domain.

The diffusion of the damage field is controlled by the characteristic length ℓ. If this parameter is increased more diffusion appears in the solution. The damage fields (with the deformed mesh) for different values of ℓ are shown in Figure 5.2. Notice that if the characteristic length is set to 0, the horizontal damage band at the left edge of the specimen is too thin —one element wide— not allowing to incorporate the isoline $D(\boldsymbol{x}) = D^*$ when the damage field is smoothed. In this chapter the value of the characteristic length has been set to ℓ=0.3 mm.

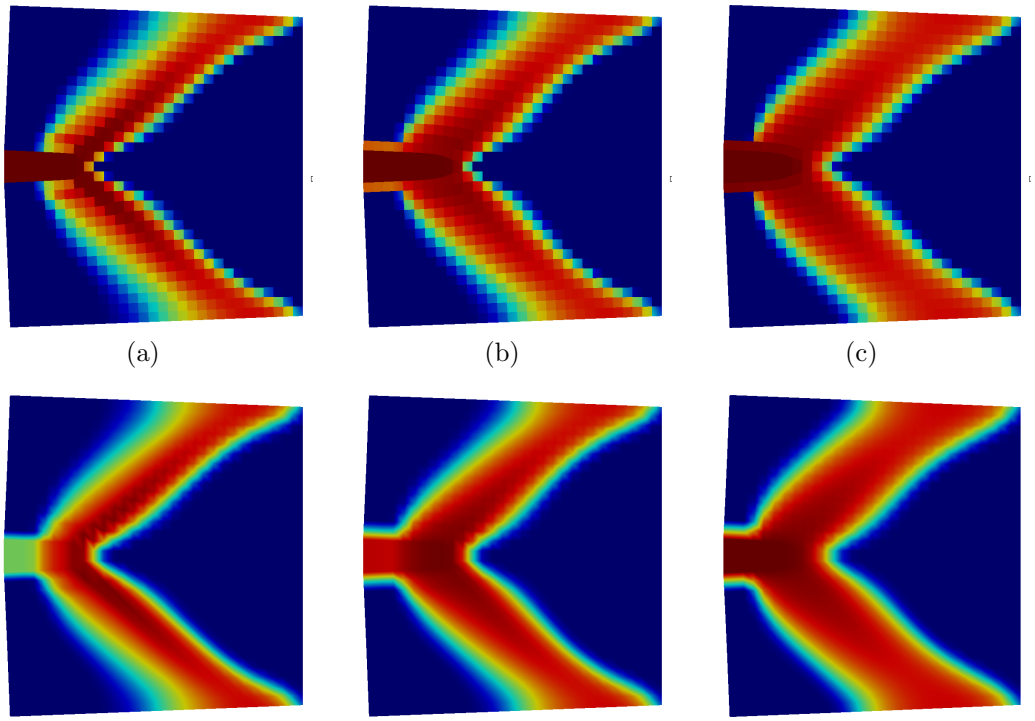

Figure 5.2: Damage field (first row) and smoothed damage field (second row) for values of characteristic length (a,d) ℓ=0, (b,e) ℓ=0.3 mm and (c,f) ℓ=3 mm.

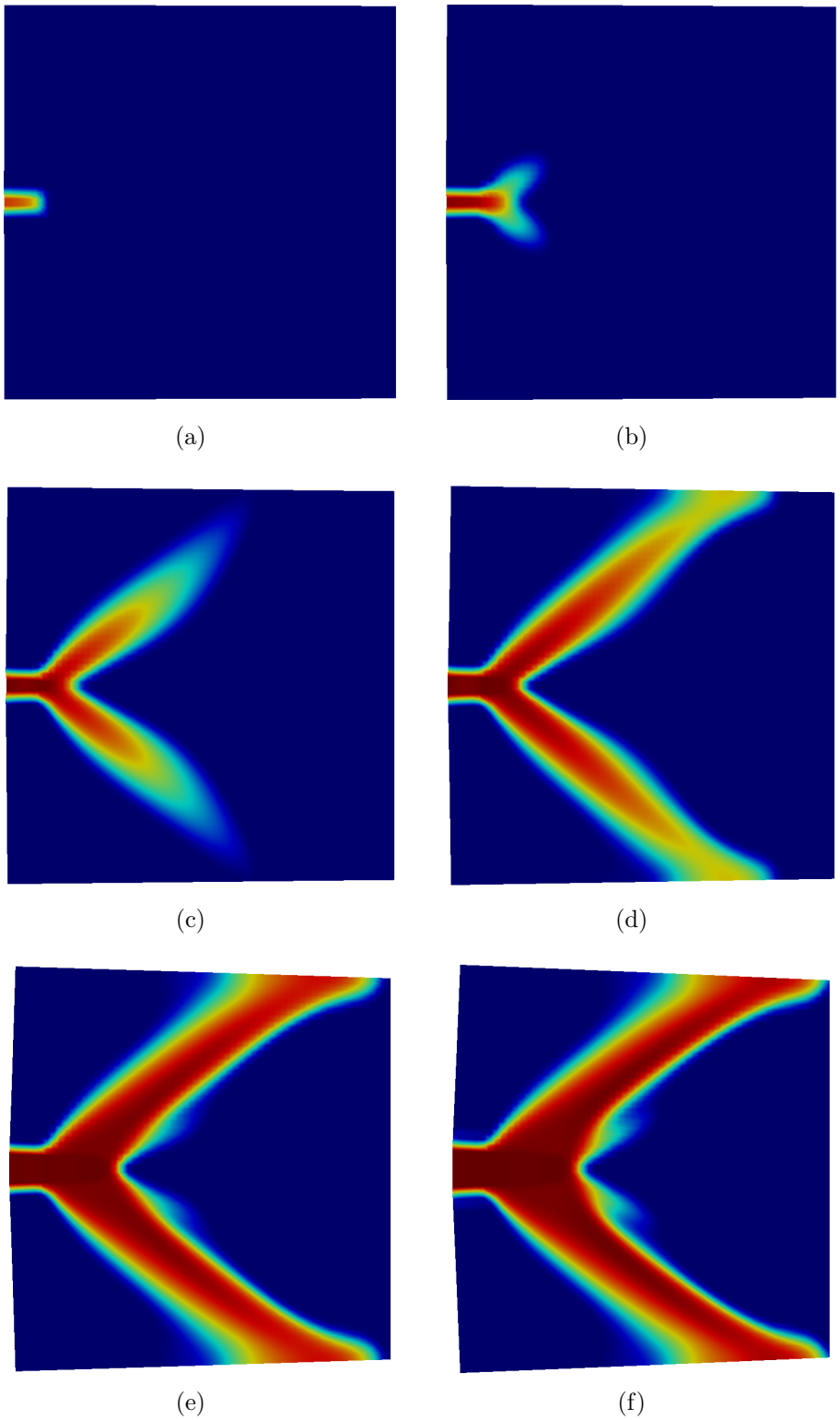

(a) (b) (c) (d) (e) (f)

Figure 5.3: Damage inception and evolution with a continuous approach. Visulisation with the deformed shape amplified.

5.5 Transition to discontinuous model

In the lasts stages of failure, when the damage field allows to identify a branched region highly damaged, a branched crack is introduced.

5.5.1 Medial axis

In order to identify the branched crack path the medial axis, in particular the θ-simplified medial axis ($\theta - SMA$) version is used. First the boundary of the damaged bulk is obtained from the isoline $D(\boldsymbol{x}) = D^*$, Figure 5.4(a). Then, the points of the medial axis of this damaged domain are computed, Figure 5.4(b), and the crack is located, Figure 5.4(c). The crack is considered to be a straight line in each element, thus leading to a piecewise linear path. From Figure 5.4 it must be stressed that the medial axis tool captures crack branching, i.e. it allows to obtain the path of a branched crack given a branched damage field.

Two parameters are important in the definition of the medial axis: (a) the isoline $D(\boldsymbol{x}) = D^*$ and (b) the separation angle θ.

The separation angle θ must not be low, in order to avoid the spurious branches that appear when computing the medial axis. If different angles are analysed, see Figure 5.5, it is observed that for separations angles higher than $\theta = 50°$, the spurious branches are removed. Thus, in this example the separation angle will be fixed to $\theta = 100°$.

The value of the isoline in this chapter has been set to $D^* = 0.9$. However other values could be used, since the sensitivity to the value of the isoline is very low. Due to the fact that the damage field is smooth enough, the same qualitative results are obtained with different values of D^*. If different values are assessed, the crack paths obtained for each one almost overlap. The only notable difference is the length of the predicted crack path, increasing when the damaged domain defined by the isoline $D(\boldsymbol{x}) = D^*$ increases —i.e. D^* is reduced—, as seen in Figure 5.6. Furthermore, the three predicted crack paths overlap in the element where branching occurs.

The value of the isoline has been set to $D^* = 0.9$ in order to introduce directly a branched crack when the branched damaged bulk is highly damaged. Note that although we have established a high damage value $D(\boldsymbol{x}) = D^*$, if all the elements crossed by the medial axis are cracked, some stiffness of the specimen is lost.

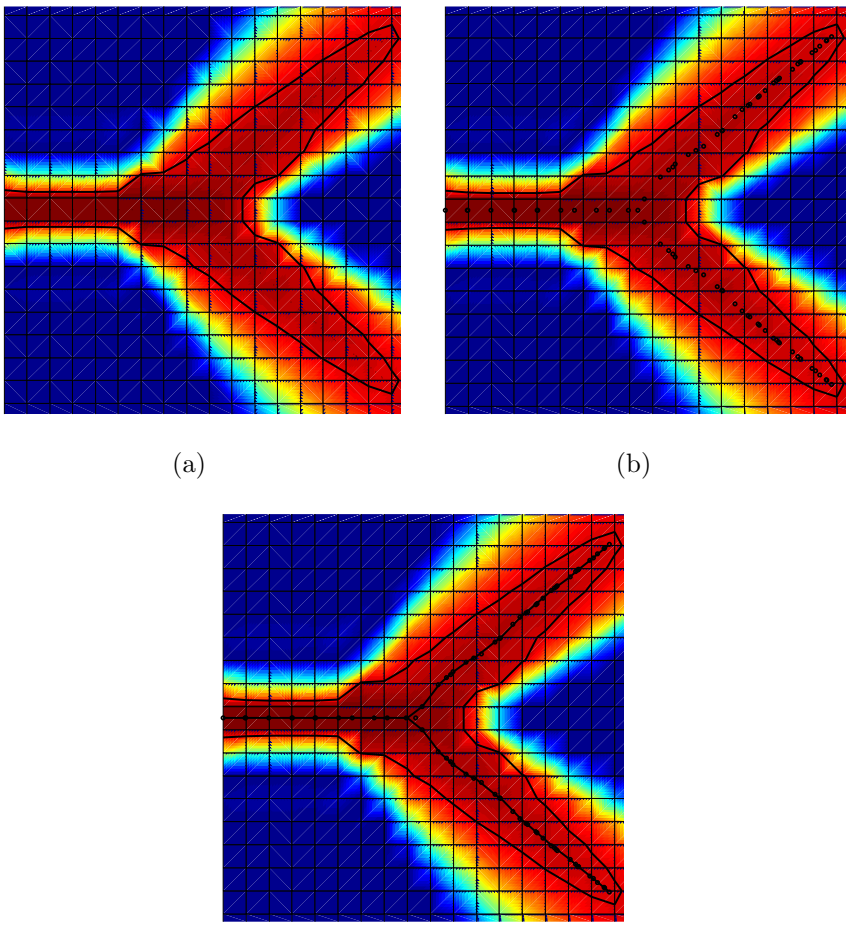

(a) (b)

(c)

Figure 5.4: Crack path obtained with medial axis. (a) Isoline, (b) points of medial axis and (c) crack path.

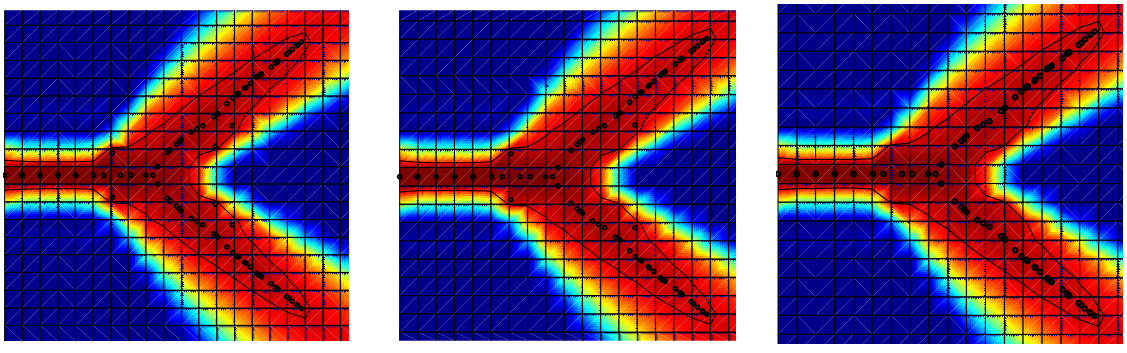

(a) (b) (c)

Figure 5.5: Points of the medial axis for different angles of separation: (a) $\theta = 10°$, (b) $\theta = 30°$ and (c) $\theta = 50°$.

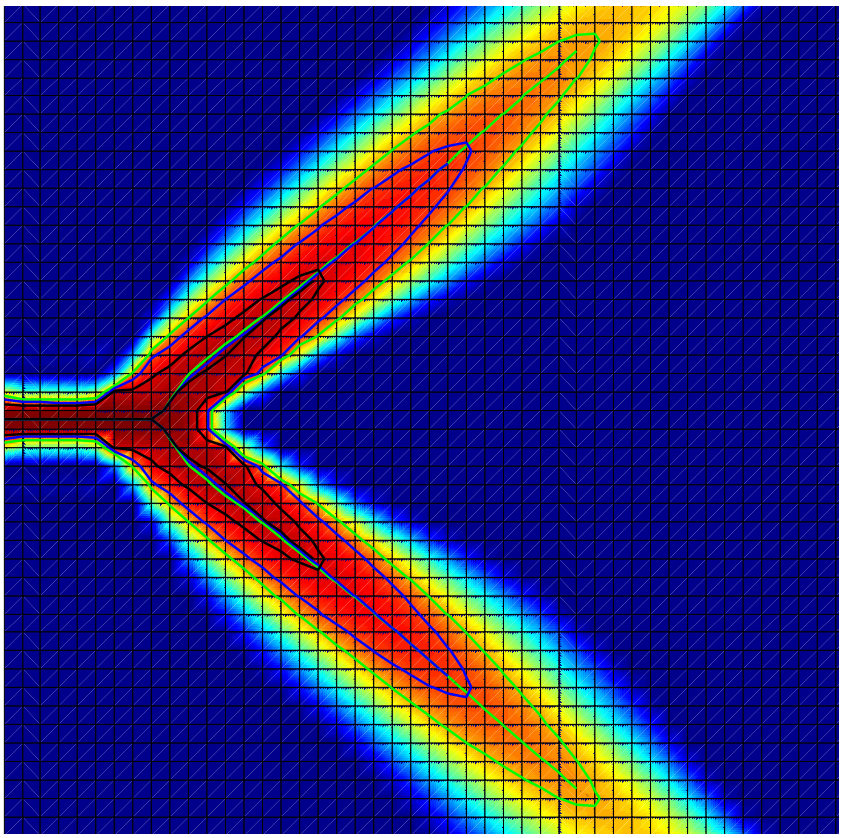

Figure 5.6: Crack path obtained with $D^* = 0.7$ (green), $D^* = 0.8$ (blue) and $D^* = 0.9$ (black).

5.5.2 Crack branching introduction

Once the crack path is identified with the medial axis, the branched crack is introduced according to X-FEM. Note that the medial axis has been computed with the isoline $D(\boldsymbol{x}) = 0.9$. Thus, the damage parameter in the cracked element will be within the range of values $0.9 < D(\boldsymbol{x}) < 1$, leading to a loss of energy when the crack is introduced, since the elements with damage $D(\boldsymbol{x}) < 1$ still have some stiffness. Due to the fact that we are following an incremental-iterative scheme, we cannot introduce the entire branched crack in one step, we have to switch from damaged elements to cracked elements incrementally. To do so, we have proposed the following process, defined in the force-displacement curve of Figure 5.7:

- We let the damage evolve enough (black line) to produce a branched damage bulk of material bounded by isoline $D(\boldsymbol{x}) = 0.9$; notice that softening is present

in the force-displacement curve. At this point, the specimen is entirely unloaded (green line). Notice that the unloading is linear and that stresses and strains decrease while damage remains constant during the unloading.

- When the specimen has been totally unloaded, the branched crack is introduced, and we load incrementally the specimen increasing the prescribed displacements (red line). This process is elastic (linear) and thus, the damage field remains constant while strains and stresses increase. However the elastic loading does not follow the elastic unloading path due to the fact that some stiffness of the specimen has been lost by introducing the crack in elements which still have some load-carrying capacity ($0.9 < D(\boldsymbol{x}) < 1$).

- After introducing the branched crack, the specimen is loaded up to a point where damage begins to increase and softening appears (blue line). Notice that the point where we unload (transition from black to green line) and the point where damage starts to increase after introducing the crack (transition from red to blue line) share the same displacement, but there is a loss of load-carrying capacity. This loss —i.e., the jump from one point to the other— is due to the introduction of a traction-free crack before damage reaches the value $D = 1$ on cracked elements. Note that with an incremental strategy we need to unload and load the specimen, otherwise we would not be able to represent this jump in the solution with only one load step. In order to avoid this jump, cohesive cracks may be introduced.

In order to introduce the branched crack, the elements are enriched as described in Chapter 3. The principal crack is considered to be the upper one, with the enriched nodes painted in pink in Figure 5.8. The secondary crack is the one that propagates towards the bottom of the domain, with the enriched nodes painted in green in Figure 5.8. The element where crack branching occurs has the nodes enhanced by both the principal and secondary crack, thus leading to 6 degrees of freedom in each node. Note that crack tips belong to an element edge whose nodes are not enriched. This is done to prevent crack opening at the crack tip, setting the displacement jump to zero. The discontinuity functions ψ_p and ψ_s are defined as in Figure 5.9, with $\psi_p = -1$ above the principal crack and $\psi_p = +1$ below (and analogously for the secondary crack).

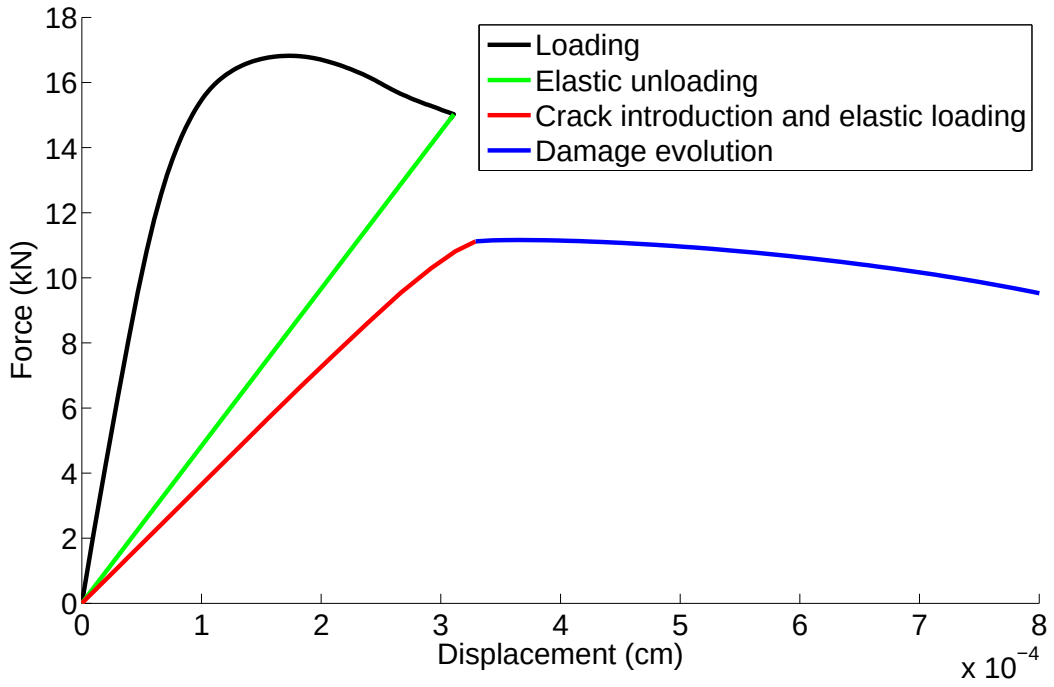

Figure 5.7: Force-displacement curve to introduce a traction-free branched crack.

The geometry of the crack and the X-FEM enrichment is introduced at the end of the last unload step. In the next load step the branched crack effectively opens. In Figure 5.10(b) the damage field is ploted on the deformed shape —with the displacement field amplified by 5000— of the specimen with crack branching. Note that the crack opens symmetrically, concluding that the hierarchy used in the X-FEM enrichment —i.e., making a distinction between the principal and the secondary crack— does not break symmetry and has no influence on the results.

Once the crack is introduced, the damage continues to increase in the following load steps, see Figure 5.11. This damage evolution is similar to the one obtained with a continuous model (Section 5.4), except by the arch of damage emerging from both crack tips.

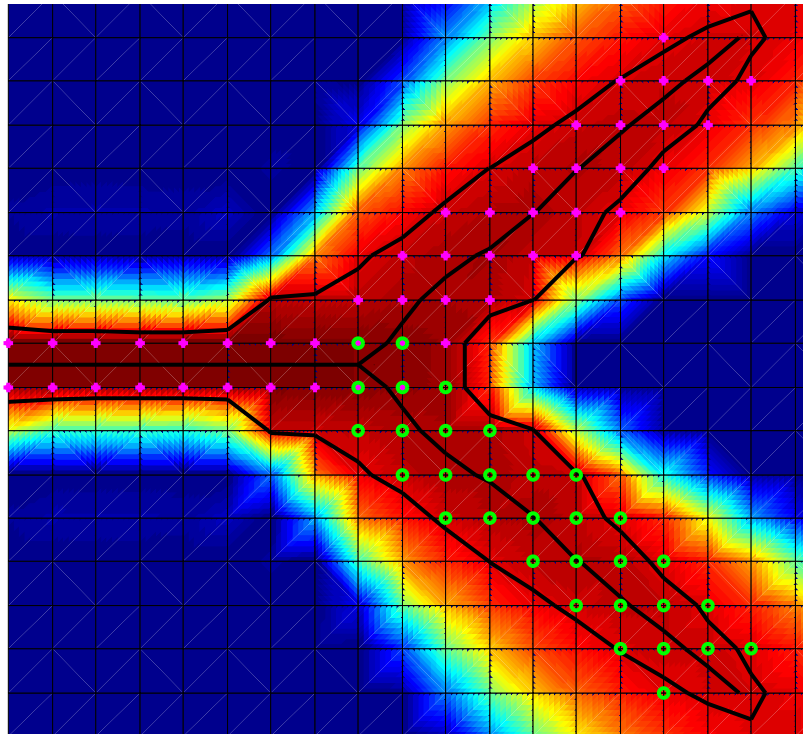

Figure 5.8: Enrich nodes for the principal crack (pink) and for the secondary crack (green).

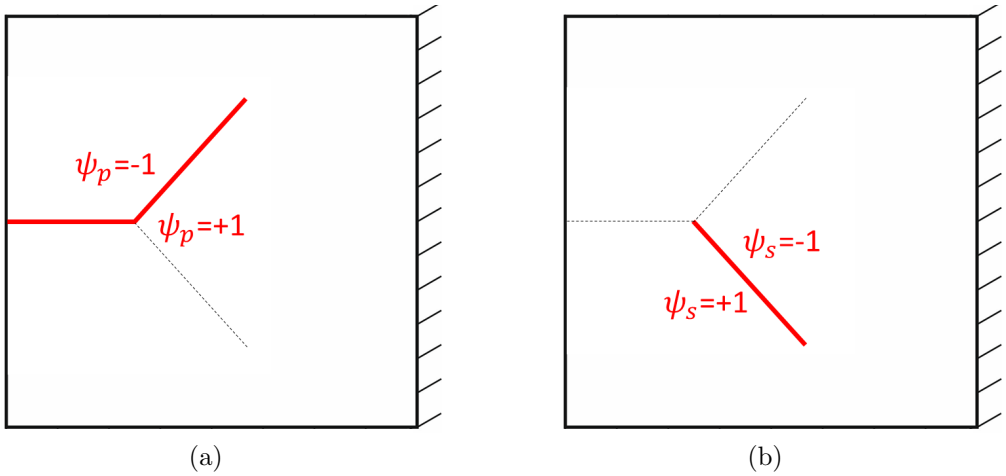

Figure 5.9: Definition of the sign functions (a) ψ_p and (b) ψ_s.

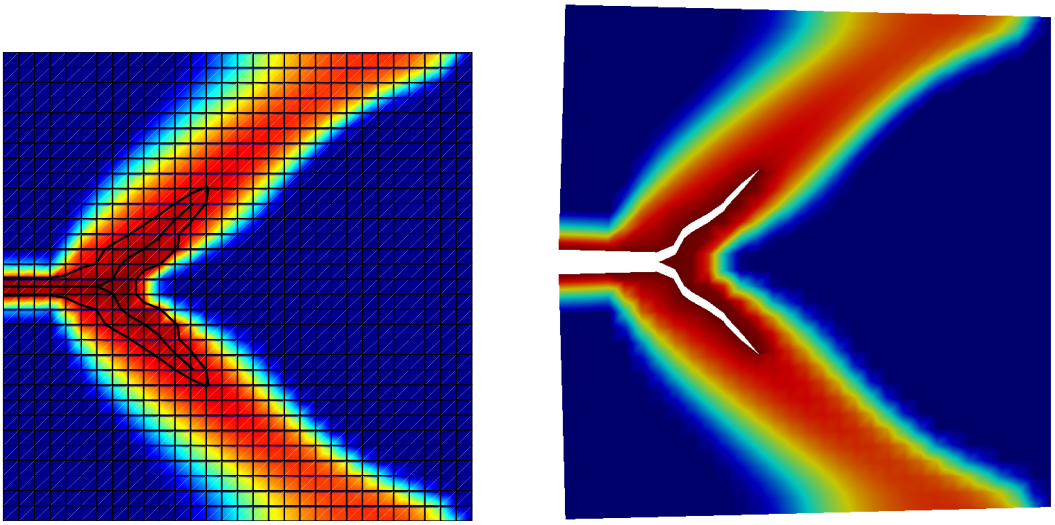

(a) (b)

Figure 5.10: (a) The crack geometry is computed by means of the $\theta-$SMA and (b) the branched crack opens in the following step. Amplification factor of 5000 in displacements.

5.5.3 Propagation of two cracks

As damage evolves with the prescribed displacements, so does the crack. In order to propagate the branched crack, the isoline $D(\boldsymbol{x}) = 0.9$ and the corresponding medial axis is computed at the end of each load step. If the crack tip defined by the medial axis moves forward, the new cracked elements are enriched. Note that in each step of the incremental-iterative scheme the crack length is fixed, invariant to each iteration of the full Newton-Raphson within the same load step. Crack propagation —similarly to crack introduction— only takes place at the end of each load step. In Figures 5.12 and 5.13 the propagation of both cracks tips is shown.

Note that the principal and secondary cracks propagate symmetrically up to a point where symmetry is broken and the secondary crack evolves while the principal crack path remains steady. This behaviour may occur in numerical analysis, where numerical errors can lead to a break of symmetry. Even if the geometry and the boundary conditions are symmetric, when solving numerically the problem we introduce some asymmetry.

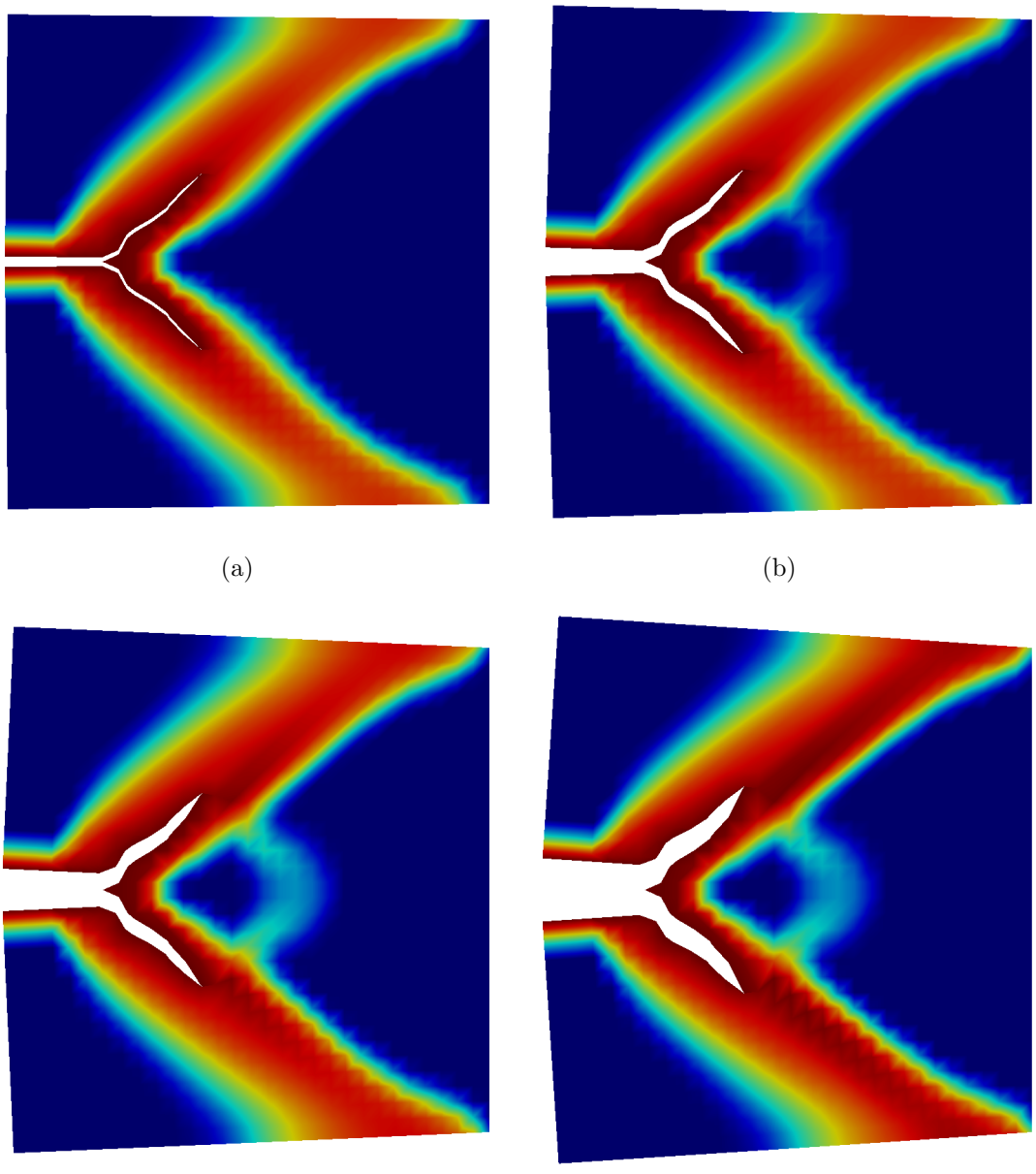

(a) (b)

(c) (d)

Figure 5.11: Evolution of damage and crack opening once the crack is introduced. Amplification factor of 100 in displacements.

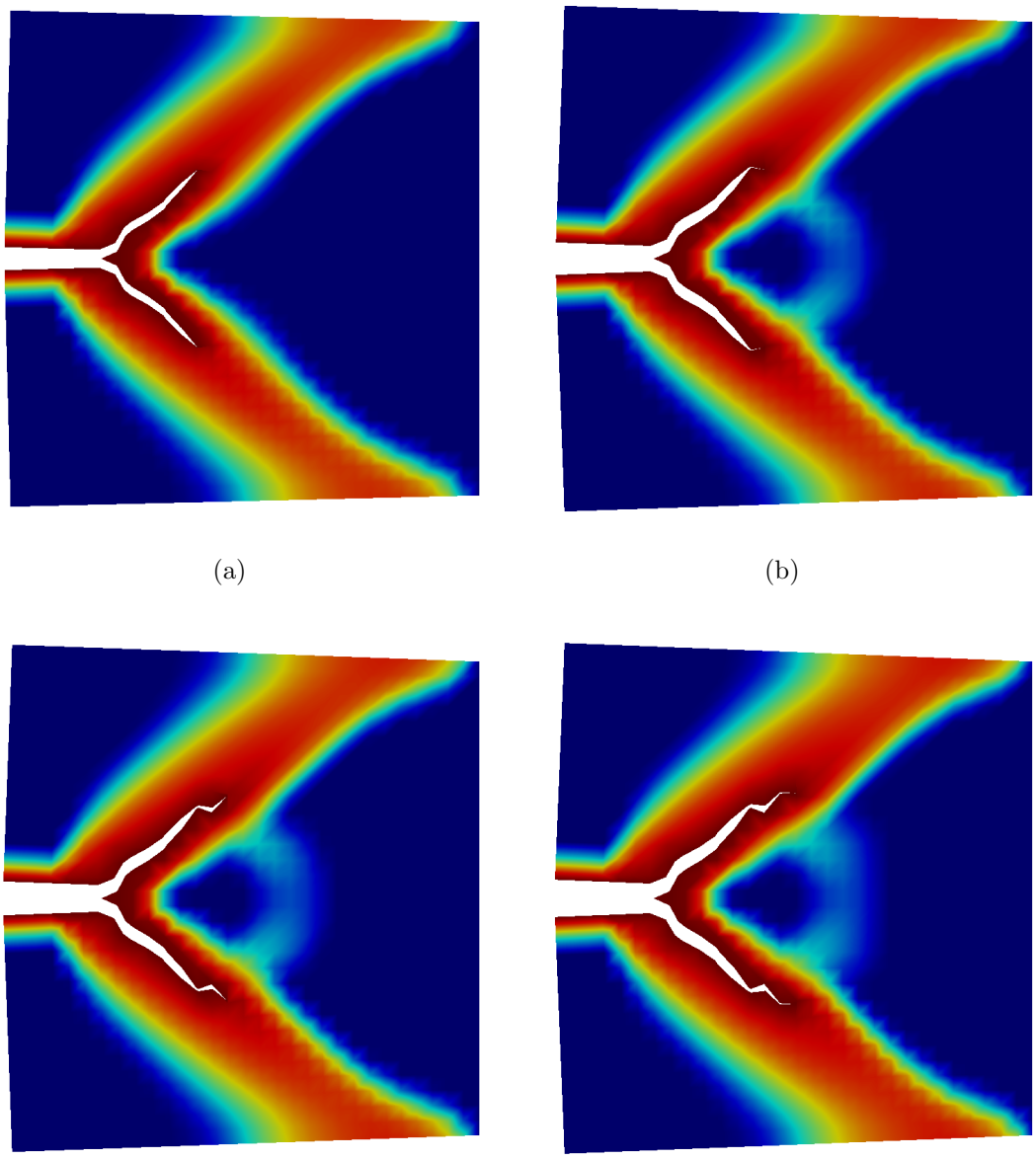

(a) (b)

(c) (d)

Figure 5.12: Crack propagation. Amplification factor of 100 in displacements.

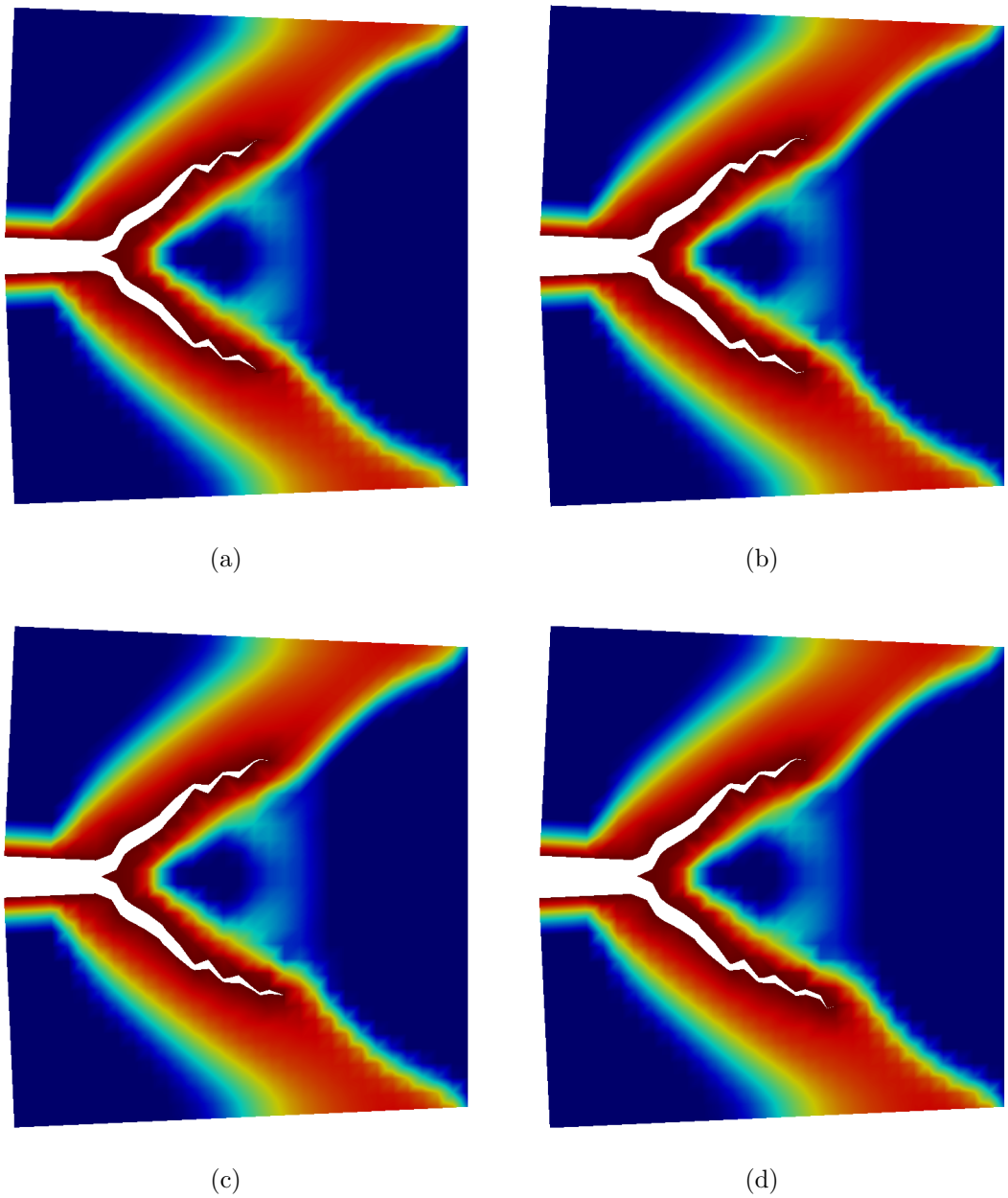

(a) (b)

(c) (d)

Figure 5.13: Crack propagation and break of symmetry (c, d) on the results. Amplification factor of 100 in displacements.

Chapter 6

Conclusions and future work

6.1 Conclusions and summary of results

The main purpose of this thesis was to develop a method for numerical simulation of crack branching in quasi-brittle failure. In civil engineering, crack branching is present in concrete structures and in rocks. The explicit modelling of crack geometry is necessary in some applications, such as hydrofracturing or fibre-reinforced concrete. To this end we make use of the eXtended Finite Element Method (X-FEM) to introduce discontinuities in the displacement field.

Numerical examples using an elastic material have shown the validity of the alternative X-FEM enrichment for crack branching proposed in this thesis. This enrichment enables branched strong discontinuities to occur in the displacement field, allowing to introduce a branched discontinuity or two non-intersecting discontinuities in a finite element.

The applicability of the continuous-discontinuous approach presented by Tamayo-Mas and Rodríguez-Ferran (2014) has been extended to include crack branching. The introduction of the secondary crack in the formulation leads to extra terms and equations in the system of equations to solve, increasing the size of the tangent matrix. Additionally, the consistent linearisation of equations is not lost with the introduction of crack branching and quadratic convergence is obtained with the full Newton-Raphson method.

We have carried out a numerical example to illustrate the capabilities of the

continuous-discontinuous approach with X-FEM for crack branching simulation. This approach allows to explicitly introduce a branched crack in a numerical simulation, validating the X-FEM enrichment proposed. Therefore, it is possible to perform full numerical tests in quasi-brittle failure when crack branching occurs, describing the first stages of failure —damage inception and damage propagation— with a continuous model and the last stages —introduction and propagation of a branched crack— with a discontinuous model. Additionally, with this numerical example, we have proved that the geometrical criterion used for crack path identification captures crack branching.

6.2 Future work

From the summary of results and the conlusions presented above several lines of further research are revealed:

- **Multiple intersecting cracks**. The continuous-discontinuous model used in this thesis could be extended to its use with multiple intersecting cracks instead of crack branching. To this end, the X-FEM enrichment used in this thesis should be verified for multiple intersecting cracks, making the adequate improvements if necessary.

- **Introduction of pressure in the cracks**. Once the crack is opened a pressure may be introduced in the faces of the crack, producing crack propagation. This fluid-structure interaction problem, where the fluid is represented by a pressure applied on the crack surface, may be used to simulate **hydraulic fracturing**, commonly known as fracking.

- **Addition of tip functions in the aproximating space for the displacement field**. The asymptotic near-tip field issued by Belytschko and Black (1999) can be used to enrich the finite element approximation. This would allow to suppress the assumption that the crack tip belongs to an element edge.

- **Introduction of cohesive cracks**. The method may be enriched with the addition of cohesive cracks such as done by Tamayo-Mas (2013). In Appendix B cohesive cracks are introduced in the formulation by adding an extra block matrix in the tangent matrix. However, numerical examples should be carried

out in order to verify that the introduction of a cohesive crack ensures an adequate transfer of energy, i.e. no loss of energy occurs when switching from a continuous model to a continuous-discontinuous model. This would allow to model crack branching in **steel-fibre reinforced concrete structures**. In steel-fibre reinforced concrete cracks are not traction-free, there is an existing interaction on the two faces of the cracks by means of tensile stress in the steel fibres.

- **Apply the approach developed in this thesis to other problems**. Other numerical examples with crack branching can be tested in order to verify the capabilities of the method presented in this thesis. For instance, some problems including crack branching can be found in crack propagation on heterogeneous materials or in dynamic crack propagation.

Appendix A

Variational formulation with smoothed displacements

In this appendix the variational formulation of the proposed model by Tamayo-Mas (2013) is presented: both the equilibrium and the regularisation equations with combined boundary conditions are expressed in a weak form. First, in Section A.1, the continuous model is reviewed, placing special attention on the way combined boundary conditions are prescribed. Second, in Section A.2, the continuous-discontinuous model is presented, extending its use to the insertion of two cracks (i.e. crack branching).

A.1 Continuous model

A.1.1 Equilibrium equation

The equilibrium equation without body forces reads as

$$\nabla \cdot \boldsymbol{\sigma} = \mathbf{0} \quad \text{in } \Omega \tag{A.1a}$$

$$\boldsymbol{\sigma} \cdot \boldsymbol{n} = \bar{\boldsymbol{t}} \quad \text{on } \Gamma_t \tag{A.1b}$$

$$\boldsymbol{u} = \boldsymbol{u}^* \quad \text{on } \Gamma_u \tag{A.1c}$$

where $\boldsymbol{\sigma}$ is the Cauchy stress tensor, $\boldsymbol{n}$ is the outward unit normal to the body, $\bar{\boldsymbol{t}}$ is the traction on the Neumann boundary and $\boldsymbol{u}^*$ is a prescribed displacement on the

Dirichlet boundary.

The space of trial local displacements is defined by the function $\boldsymbol{u}(\boldsymbol{x})$, where

$$\boldsymbol{u} \in \mathcal{U}_{\boldsymbol{u}} = \left\{ \boldsymbol{u} \,|\, \boldsymbol{u} \in H^1(\Omega) \text{ and } \boldsymbol{u}_{|\Gamma_u} = \boldsymbol{u}^* \right\} \tag{A.2}$$

with $H^1(\Omega)$ a Sobolev space.

Analogously, the space of admissible displacement variations is defined by the test function $\boldsymbol{\omega}(\boldsymbol{x})$ with

$$\boldsymbol{\omega} \in \mathcal{W}_{\boldsymbol{u},\mathbf{0}} = \left\{ \boldsymbol{\omega} \mid \boldsymbol{\omega} \in H^1(\Omega) \text{ and } \boldsymbol{\omega}_{|\Gamma_u} = \mathbf{0} \right\} \tag{A.3}$$

The equilibrium equation —Equation (A.1)— can be cast in the weak form

$$\int_\Omega \nabla^s \boldsymbol{\omega} : \boldsymbol{\sigma} \, \mathrm{d}\Omega = \int_{\Gamma_t} \boldsymbol{\omega} \cdot \bar{\boldsymbol{t}} \, \mathrm{d}\Gamma \qquad \forall \boldsymbol{\omega} \in H^1(\Omega) \tag{A.4}$$

A.1.2 Regularisation equation

Similarly to the equilibrium equation, the regularisation PDE

$$\widetilde{\boldsymbol{u}}(\boldsymbol{x}) - \ell^2 \nabla^2 \widetilde{\boldsymbol{u}}(\boldsymbol{x}) = \boldsymbol{u}(\boldsymbol{x}) \tag{A.5}$$

with combined boundary conditions is also expressed in a weak form.

Analogously to local displacements, the space of trial smoothed displacements is defined by the function $\widetilde{\boldsymbol{u}}(\boldsymbol{x})$ where

$$\widetilde{\boldsymbol{u}} \in \mathcal{U}_{\widetilde{\boldsymbol{u}}} = \left\{ \widetilde{\boldsymbol{u}} \,|\, \widetilde{\boldsymbol{u}} \in H^1(\Omega) \text{ and } \widetilde{\boldsymbol{u}} \cdot \boldsymbol{n} = \boldsymbol{u} \cdot \boldsymbol{n} \text{ on } \Gamma \right\} \tag{A.6}$$

The space of admissible smoothed displacement variations is defined by the test function $\widetilde{\boldsymbol{\omega}}(\boldsymbol{x})$ with

$$\widetilde{\boldsymbol{\omega}} \in \mathcal{W}_{\widetilde{\boldsymbol{u}},\mathbf{0}} = \left\{ \widetilde{\boldsymbol{\omega}} \mid \widetilde{\boldsymbol{\omega}} \in H^1(\Omega) \text{ and } \widetilde{\boldsymbol{\omega}} \cdot \boldsymbol{n} = \mathbf{0} \text{ on } \Gamma \right\} \tag{A.7}$$

The regularisation equation (A.5) is multiplied by the test function $\widetilde{\boldsymbol{\omega}}(\boldsymbol{x})$ and integrated over the domain Ω thus leading to

$$\int_\Omega \widetilde{\boldsymbol{\omega}} \cdot \widetilde{\boldsymbol{u}} \, \mathrm{d}\Omega + \ell^2 \int_\Omega \nabla \widetilde{\boldsymbol{\omega}} : \nabla \widetilde{\boldsymbol{u}} \, \mathrm{d}\Omega - \ell^2 \int_\Gamma \widetilde{\boldsymbol{\omega}} \cdot \nabla \widetilde{\boldsymbol{u}} \cdot \boldsymbol{n} \, \mathrm{d}\Gamma = \int_\Omega \widetilde{\boldsymbol{\omega}} \cdot \boldsymbol{u} \, \mathrm{d}\Omega \tag{A.8}$$

Considering the orthonormal basis of $\mathbb{R}^2$ formed by the normal vector $\boldsymbol{n}$ and the tangent vector $\boldsymbol{\tau}$, and taking into account that $\widetilde{\boldsymbol{\omega}} \cdot \boldsymbol{n} = \mathbf{0}$ on Γ, see Equation (A.7),

$$\begin{aligned}\int_\Gamma \widetilde{\boldsymbol{\omega}} \cdot \nabla \widetilde{\boldsymbol{u}} \cdot \boldsymbol{n} \, \mathrm{d}\Gamma &= \int_\Gamma (\widetilde{\boldsymbol{\omega}} \cdot \boldsymbol{\tau}) \cdot (\nabla (\widetilde{\boldsymbol{u}} \cdot \boldsymbol{\tau}) \cdot \boldsymbol{n}) \, \mathrm{d}\Gamma \\ &= \int_\Gamma (\widetilde{\boldsymbol{\omega}} \cdot \boldsymbol{\tau}) \cdot (\nabla (\boldsymbol{u} \cdot \boldsymbol{\tau}) \cdot \boldsymbol{n}) \, \mathrm{d}\Gamma \end{aligned} \tag{A.9}$$

where in the last equality, combined boundary conditions are prescribed. Hence, $\forall \widetilde{\boldsymbol{\omega}} \in H^1(\Omega)$, Equation (A.8) leads to

$$\begin{aligned}\int_\Omega \widetilde{\boldsymbol{\omega}} \cdot \widetilde{\boldsymbol{u}} \, \mathrm{d}\Omega &+ \ell^2 \int_\Omega \nabla \widetilde{\boldsymbol{\omega}} : \nabla \widetilde{\boldsymbol{u}} \, \mathrm{d}\Omega = \int_\Omega \widetilde{\boldsymbol{\omega}} \cdot \boldsymbol{u} \, \mathrm{d}\Omega + \\ &+ \ell^2 \int_\Gamma (\widetilde{\boldsymbol{\omega}} \cdot \boldsymbol{\tau}) \cdot (\nabla (\boldsymbol{u} \cdot \boldsymbol{\tau}) \cdot \boldsymbol{n}) \, \mathrm{d}\Gamma \end{aligned} \tag{A.10}$$

A.2 Continuous-discontinuous model

A.2.1 Equilibrium equation

Here, the equilibrium equation without body forces is

$$\nabla \cdot \boldsymbol{\sigma} = \mathbf{0} \quad \text{in } \Omega \tag{A.11a}$$

$$\boldsymbol{\sigma} \cdot \boldsymbol{n} = \bar{\boldsymbol{t}} \quad \text{on } \Gamma_t \tag{A.11b}$$

$$\boldsymbol{\sigma} \cdot \boldsymbol{n} = \bar{\boldsymbol{t}}_p \quad \text{on } \Gamma_p \tag{A.11c}$$

$$\boldsymbol{\sigma} \cdot \boldsymbol{n} = \bar{\boldsymbol{t}}_s \quad \text{on } \Gamma_s \tag{A.11d}$$

$$\boldsymbol{u} = \boldsymbol{u}^* \quad \text{on } \Gamma_u \tag{A.11e}$$

On the one hand, if traction-free cracks are considered $\bar{\boldsymbol{t}}_p = \mathbf{0}$ and $\bar{\boldsymbol{t}}_s = \mathbf{0}$, as done in Chapters 4 and 5. On the other hand, if cohesive cracks are taken into account

$$\dot{\bar{\boldsymbol{t}}}_p = \boldsymbol{f}\left(\llbracket \dot{\boldsymbol{u}} \rrbracket\right) \tag{A.12a}$$

$$\dot{\bar{\boldsymbol{t}}}_s = \boldsymbol{f}\left(\llbracket \dot{\boldsymbol{u}} \rrbracket\right) \tag{A.12b}$$

with $\boldsymbol{f}$ relating traction rates $\dot{\bar{\boldsymbol{t}}}_p$, $\dot{\bar{\boldsymbol{t}}}_s$ and displacement jump rate $\llbracket \dot{\boldsymbol{u}} \rrbracket$.

In a continuous-discontinuous model with crack branching, the space of trial local displacements is defined by the function

$$\boldsymbol{u}(\boldsymbol{x}) = \boldsymbol{u}_c(\boldsymbol{x}) + \psi_p(\boldsymbol{x})\, \boldsymbol{u}_p(\boldsymbol{x}) + \psi_s(\boldsymbol{x})\, \boldsymbol{u}_s(\boldsymbol{x}) \tag{A.13}$$

where ψ_p and ψ_s are the sign functions centred at the discontinuities Γ_p and Γ_s, and

$$\boldsymbol{u}_c \in \mathcal{U}_{\boldsymbol{u}} = \left\{\boldsymbol{u} \mid \boldsymbol{u} \in H^1(\Omega) \text{ and } \boldsymbol{u}_{|\Gamma_u} = \boldsymbol{u}^*\right\} \tag{A.14a}$$

$$\boldsymbol{u}_p, \boldsymbol{u}_s \in \mathcal{U}_{\boldsymbol{u},\boldsymbol{0}} = \left\{\boldsymbol{u} \mid \boldsymbol{u} \in H^1(\Omega) \text{ and } \boldsymbol{u}_{|\Gamma_u} = \boldsymbol{0}\right\} \tag{A.14b}$$

with $H^1(\Omega)$ a Sobolev space.

Analogously, the space of admissible displacement variations is defined by the test function $\boldsymbol{\omega}(\boldsymbol{x}) = \boldsymbol{\omega}_c(\boldsymbol{x}) + \psi_p(\boldsymbol{x})\boldsymbol{\omega}_p(\boldsymbol{x}) + \psi_s(\boldsymbol{x})\boldsymbol{\omega}_s(\boldsymbol{x})$ with

$$\boldsymbol{\omega}_c, \boldsymbol{\omega}_p, \boldsymbol{\omega}_s \in \mathcal{W}_{\boldsymbol{u},\boldsymbol{0}} = \left\{\boldsymbol{\omega} \mid \boldsymbol{\omega} \in H^1(\Omega) \text{ and } \boldsymbol{\omega}_{|\Gamma_u} = \boldsymbol{0}\right\} \tag{A.15}$$

Then, the weak form of Equation (A.11) reads as

$$\int_\Omega \nabla^s \boldsymbol{\omega}_c : \boldsymbol{\sigma}\, \mathrm{d}\Omega = \int_{\Gamma_t} \boldsymbol{\omega}_c \cdot \bar{\boldsymbol{t}}\, \mathrm{d}\Gamma \quad \forall \boldsymbol{\omega}_c \in H^1(\Omega) \tag{A.16a}$$

$$\int_\Omega \psi_p \nabla^s \boldsymbol{\omega}_p : \boldsymbol{\sigma}\, \mathrm{d}\Omega + 2\int_{\Gamma_p} \boldsymbol{\omega}_p \cdot \bar{\boldsymbol{t}}_d\, \mathrm{d}\Gamma = \int_{\Gamma_t} \psi_p \boldsymbol{\omega}_p \cdot \bar{\boldsymbol{t}}\, \mathrm{d}\Gamma \quad \forall \boldsymbol{\omega}_p \in H^1(\Omega) \tag{A.16b}$$

$$\int_\Omega \psi_s \nabla^s \boldsymbol{\omega}_s : \boldsymbol{\sigma}\, \mathrm{d}\Omega + 2\int_{\Gamma_s} \boldsymbol{\omega}_s \cdot \bar{\boldsymbol{t}}_s\, \mathrm{d}\Gamma = \int_{\Gamma_t} \psi_s \boldsymbol{\omega}_s \cdot \bar{\boldsymbol{t}}\, \mathrm{d}\Gamma \quad \forall \boldsymbol{\omega}_s \in H^1(\Omega) \tag{A.16c}$$

where $\bar{\boldsymbol{t}}_d \neq 0$ if the principal crack is cohesive and $\bar{\boldsymbol{t}}_s \neq 0$ if the secondary crack is cohesive. In our case, see Chapters 4 and 5, $\bar{\boldsymbol{t}}_d = 0$ and $\bar{\boldsymbol{t}}_s = 0$.

Note that equation (A.16a) is the standard weak form, see Equation (A.4), while equation (A.16b) and equation (A.16c) take into account the contribution of the principal and secondary cracks.

A.2.2 Regularisation equation

Analogously to local displacements, the space of trial smoothed displacements is defined by the function

$$\widetilde{\boldsymbol{u}}(\boldsymbol{x}) = \widetilde{\boldsymbol{u}}_c(\boldsymbol{x}) + \psi_p(\boldsymbol{x})\,\widetilde{\boldsymbol{u}}_p(\boldsymbol{x}) + \psi_s(\boldsymbol{x})\,\widetilde{\boldsymbol{u}}_s(\boldsymbol{x}) \tag{A.17}$$

where ψ_p and ψ_s are the sign functions centred at Γ_p and Γ_s and

$$\widetilde{\boldsymbol{u}}_c, \widetilde{\boldsymbol{u}}_p, \widetilde{\boldsymbol{u}}_s \in \mathcal{U}_{\widetilde{\boldsymbol{u}}} = \left\{\widetilde{\boldsymbol{u}} \mid \widetilde{\boldsymbol{u}} \in H^1(\Omega) \text{ and } \widetilde{\boldsymbol{u}} \cdot \boldsymbol{n} = \boldsymbol{u} \cdot \boldsymbol{n} \text{ on } \Gamma\right\} \tag{A.18}$$

The space of admissible smoothed displacement variations is defined by the test function

$$\widetilde{\boldsymbol{\omega}}(\boldsymbol{x}) = \widetilde{\boldsymbol{\omega}}_c(\boldsymbol{x}) + \psi_p(\boldsymbol{x})\,\widetilde{\boldsymbol{\omega}}_p(\boldsymbol{x}) + \psi_s(\boldsymbol{x})\,\widetilde{\boldsymbol{\omega}}_s(\boldsymbol{x}) \tag{A.19}$$

with

$$\widetilde{\boldsymbol{\omega}}_c, \widetilde{\boldsymbol{\omega}}_p, \widetilde{\boldsymbol{\omega}}_s \in \mathcal{W}_{\widetilde{\boldsymbol{u}},\mathbf{0}} = \left\{ \widetilde{\boldsymbol{\omega}} \mid \widetilde{\boldsymbol{\omega}} \in H^1(\Omega) \text{ and } \boldsymbol{\omega} \cdot \boldsymbol{n} = \mathbf{0} \text{ on } \Gamma \right\} \tag{A.20}$$

Taking first variations $\widetilde{\boldsymbol{\omega}}_c$ ($\widetilde{\boldsymbol{\omega}}_p = \mathbf{0}$ and $\widetilde{\boldsymbol{\omega}}_s = \mathbf{0}$), then variations $\widetilde{\boldsymbol{\omega}}_p$ ($\widetilde{\boldsymbol{\omega}}_c = \mathbf{0}$ and $\widetilde{\boldsymbol{\omega}}_s = \mathbf{0}$) and last variations $\widetilde{\boldsymbol{\omega}}_s$ ($\widetilde{\boldsymbol{\omega}}_c = \mathbf{0}$ and $\widetilde{\boldsymbol{\omega}}_p = \mathbf{0}$), the final form of the variational statement leads to

$$\begin{aligned} &\int_\Omega \widetilde{\boldsymbol{\omega}}_c \cdot \widetilde{\boldsymbol{u}} \, \mathrm{d}\Omega + \ell^2 \int_\Omega \nabla\widetilde{\boldsymbol{\omega}}_c : \left(\nabla\widetilde{\boldsymbol{u}}_c + \psi_p \nabla\widetilde{\boldsymbol{u}}_p + \psi_s \nabla\widetilde{\boldsymbol{u}}_s \right) \mathrm{d}\Omega = \int_\Omega \widetilde{\boldsymbol{\omega}}_c \cdot \boldsymbol{u} \, \mathrm{d}\Omega + \\ + \quad &\ell^2 \int_\Gamma (\widetilde{\boldsymbol{\omega}}_c \cdot \boldsymbol{\tau}) \cdot \left[\nabla (\boldsymbol{u}_c \cdot \boldsymbol{t}_1) \cdot \boldsymbol{n} + \psi_p \nabla \left(\boldsymbol{u}_p \cdot \boldsymbol{\tau} \right) \cdot \boldsymbol{n} + \psi_s \nabla (\boldsymbol{u}_s \cdot \boldsymbol{\tau}) \cdot \boldsymbol{n} \right] \mathrm{d}\Gamma \end{aligned} \tag{A.21a}$$

$$\begin{aligned} &\int_\Omega \psi_p \widetilde{\boldsymbol{\omega}}_p \cdot \widetilde{\boldsymbol{u}} \, \mathrm{d}\Omega + \ell^2 \int_\Omega \psi_p \nabla\widetilde{\boldsymbol{\omega}}_p : \left(\nabla\widetilde{\boldsymbol{u}}_c + \psi_p \nabla\widetilde{\boldsymbol{u}}_p + \psi_s \nabla\widetilde{\boldsymbol{u}}_s \right) \mathrm{d}\Omega = \int_\Omega \psi_p \widetilde{\boldsymbol{\omega}}_p \cdot \boldsymbol{u} \, \mathrm{d}\Omega + \\ + \quad &\ell^2 \int_\Gamma (\psi_p \widetilde{\boldsymbol{\omega}}_p \cdot \boldsymbol{\tau}) \cdot \left[\nabla (\boldsymbol{u}_c \cdot \boldsymbol{\tau}) \cdot \boldsymbol{n} + \psi_p \nabla \left(\boldsymbol{u}_p \cdot \boldsymbol{\tau} \right) \cdot \boldsymbol{n} + \psi_s \nabla (\boldsymbol{u}_s \cdot \boldsymbol{\tau}) \cdot \boldsymbol{n} \right] \mathrm{d}\Gamma \end{aligned} \tag{A.21b}$$

$$\begin{aligned} &\int_\Omega \psi_s \widetilde{\boldsymbol{\omega}}_s \cdot \widetilde{\boldsymbol{u}} \, \mathrm{d}\Omega + \ell^2 \int_\Omega \psi_s \nabla\widetilde{\boldsymbol{\omega}}_s : \left(\nabla\widetilde{\boldsymbol{u}}_c + \psi_p \nabla\widetilde{\boldsymbol{u}}_p + \psi_s \nabla\widetilde{\boldsymbol{u}}_s \right) \mathrm{d}\Omega = \int_\Omega \psi_s \widetilde{\boldsymbol{\omega}}_s \cdot \boldsymbol{u} \, \mathrm{d}\Omega + \\ + \quad &\ell^2 \int_\Gamma (\psi_s \widetilde{\boldsymbol{\omega}}_s \cdot \boldsymbol{\tau}) \cdot \left[\nabla (\boldsymbol{u}_c \cdot \boldsymbol{\tau}) \cdot \boldsymbol{n} + \psi_p \nabla \left(\boldsymbol{u}_p \cdot \boldsymbol{\tau} \right) \cdot \boldsymbol{n} + \psi_s \nabla (\boldsymbol{u}_s \cdot \boldsymbol{\tau}) \cdot \boldsymbol{n} \right] \mathrm{d}\Gamma \end{aligned} \tag{A.21c}$$

$\forall\widetilde{\boldsymbol{\omega}}_c, \forall\widetilde{\boldsymbol{\omega}}_p, \forall\widetilde{\boldsymbol{\omega}}_s \in H^1(\Omega)$.

Taking into account that $\psi_p\psi_p = +1$ and $\psi_s\psi_s = +1$ —due to the fact that the enrichment functions are the sign functions— and defining a new discontinuous function $\psi_b = \psi_p\psi_s$, see Figure A.1, Equation (A.21) can be rewritten as

$$\begin{aligned} &\int_\Omega \widetilde{\boldsymbol{\omega}}_c \cdot \widetilde{\boldsymbol{u}} \, \mathrm{d}\Omega + \ell^2 \int_\Omega \nabla\widetilde{\boldsymbol{\omega}}_c : \left(\nabla\widetilde{\boldsymbol{u}}_c + \psi_p \nabla\widetilde{\boldsymbol{u}}_p + \psi_s \nabla\widetilde{\boldsymbol{u}}_s \right) \mathrm{d}\Omega = \int_\Omega \widetilde{\boldsymbol{\omega}}_c \cdot \boldsymbol{u} \, \mathrm{d}\Omega + \\ + \quad &\ell^2 \int_\Gamma (\widetilde{\boldsymbol{\omega}}_c \cdot \boldsymbol{\tau}) \cdot \left[\nabla (\boldsymbol{u}_c \cdot \boldsymbol{t}_1) \cdot \boldsymbol{n} + \psi_p \nabla \left(\boldsymbol{u}_p \cdot \boldsymbol{\tau} \right) \cdot \boldsymbol{n} + \psi_s \nabla (\boldsymbol{u}_s \cdot \boldsymbol{\tau}) \cdot \boldsymbol{n} \right] \mathrm{d}\Gamma \end{aligned} \tag{A.22a}$$

$$\begin{aligned} &\int_\Omega \psi_p \widetilde{\boldsymbol{\omega}}_p \cdot \widetilde{\boldsymbol{u}} \, \mathrm{d}\Omega + \ell^2 \int_\Omega \nabla\widetilde{\boldsymbol{\omega}}_p : \left(\psi_p \nabla\widetilde{\boldsymbol{u}}_c + \nabla\widetilde{\boldsymbol{u}}_p + \psi_b \nabla\widetilde{\boldsymbol{u}}_s \right) \mathrm{d}\Omega = \int_\Omega \psi_p \widetilde{\boldsymbol{\omega}}_p \cdot \boldsymbol{u} \, \mathrm{d}\Omega + \\ + \quad &\ell^2 \int_\Gamma (\widetilde{\boldsymbol{\omega}}_p \cdot \boldsymbol{\tau}) \cdot \left[\psi_p \nabla (\boldsymbol{u}_c \cdot \boldsymbol{\tau}) \cdot \boldsymbol{n} + \nabla \left(\boldsymbol{u}_p \cdot \boldsymbol{\tau} \right) \cdot \boldsymbol{n} + \psi_b \nabla (\boldsymbol{u}_s \cdot \boldsymbol{\tau}) \cdot \boldsymbol{n} \right] \mathrm{d}\Gamma \end{aligned} \tag{A.22b}$$

$$\begin{aligned} &\int_\Omega \psi_s \widetilde{\boldsymbol{\omega}}_s \cdot \widetilde{\boldsymbol{u}} \, \mathrm{d}\Omega + \ell^2 \int_\Omega \nabla\widetilde{\boldsymbol{\omega}}_s : \left(\psi_s \nabla\widetilde{\boldsymbol{u}}_c + \psi_b \nabla\widetilde{\boldsymbol{u}}_p + \nabla\widetilde{\boldsymbol{u}}_s \right) \mathrm{d}\Omega = \int_\Omega \psi_s \widetilde{\boldsymbol{\omega}}_s \cdot \boldsymbol{u} \, \mathrm{d}\Omega + \\ + \quad &\ell^2 \int_\Gamma (\widetilde{\boldsymbol{\omega}}_s \cdot \boldsymbol{\tau}) \cdot \left[\psi_s \nabla (\boldsymbol{u}_c \cdot \boldsymbol{\tau}) \cdot \boldsymbol{n} + \psi_b \nabla \left(\boldsymbol{u}_p \cdot \boldsymbol{\tau} \right) \cdot \boldsymbol{n} + \nabla (\boldsymbol{u}_s \cdot \boldsymbol{\tau}) \cdot \boldsymbol{n} \right] \mathrm{d}\Gamma \end{aligned} \tag{A.22c}$$

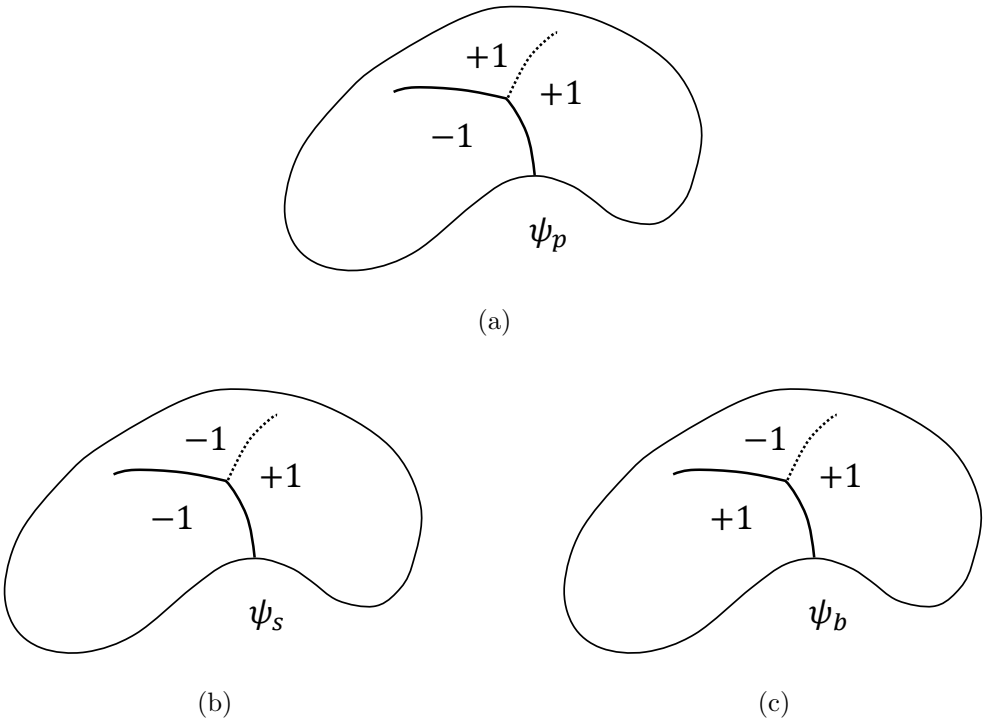

Figure A.1: Definition of (a) ψ_p, (b) ψ_s and (c) ψ_b on Ω.

Appendix B

Consistent linearisation of the equilibrium and regularisation equations

---

The non-local damage model based on smoothed displacements —derived by Rodríguez-Ferran et al. (2005)— used in this thesis is very attractive from a computational viewpoint due to the consistent tangent matrix obtained to achieve quadratic convergence in the Newton-Raphson method. In this appendix, the tangent matrix is obtained from the linearisation of the variational formulation presented in Appendix A. First, in Section B.1, the expression of the consistent tangent matrix of the continuous model is reviewed. Second, in Section B.2, the tangent matrix of the continuous-discontinuous model for crack branching is derived. The Lagrange multipliers technique used to prescribe boundary conditions is also taken into account in both sections.

B.1 Continuous model

Finite element discretisation of the weak form of the equilibrium and regularisation equations, see Equations (A.4) and (A.10), leads to the two discrete weak forms

$$\mathbf{r}_{\text{equi}}(\mathbf{u},\widetilde{\mathbf{u}}) := \mathbf{f}_{\text{int}}(\mathbf{u},\widetilde{\mathbf{u}}) - \mathbf{f}_{\text{ext}} = \mathbf{0} \tag{B.1a}$$

$$\mathbf{r}_{\text{reg}}(\mathbf{u},\widetilde{\mathbf{u}}) := -(\mathbf{M}+\ell^2\mathbf{K}_{\text{BC}})\mathbf{u} + (\mathbf{M}+\ell^2\mathbf{D})\widetilde{\mathbf{u}} = \mathbf{0} \tag{B.1b}$$

where

$$\mathbf{f}_{\text{int}} = \int_{\Omega} \mathbf{B}^T \boldsymbol{\sigma} \, \mathrm{d}\Omega \tag{B.2a}$$

$$\mathbf{f}_{\text{ext}} = \int_{\Gamma_t} \mathbf{N}^T \bar{\boldsymbol{t}} \, \mathrm{d}\Gamma \tag{B.2b}$$

$$\mathbf{M} = \int_{\Omega} \mathbf{N}^T \mathbf{N} \, \mathrm{d}\Omega \tag{B.2c}$$

$$\mathbf{D} = \int_{\Omega} \nabla \mathbf{N}^T \nabla \mathbf{N} \, \mathrm{d}\Omega \tag{B.2d}$$

$$\mathbf{K}_{\text{BC}} = \int_{\Gamma} \mathbf{N}^T \left(\boldsymbol{\tau}^T \boldsymbol{\tau} \right) \nabla \mathbf{N} \cdot \boldsymbol{n} \, \mathrm{d}\Gamma \tag{B.2e}$$

with $\mathbf{N}$ the matrix of shape functions, $\nabla \mathbf{N}$ the matrix of shape function gradients and $\mathbf{B}$ the matrix of shape function derivatives.

Linearisation of Equations (B.1) results in the tangent matrix

$$\mathbf{K}_{\text{tan}} = \begin{bmatrix} \mathbf{K}_{\mathbf{u},\mathbf{u}} & \mathbf{K}_{\mathbf{u},\tilde{\mathbf{u}}} \\ \mathbf{K}_{\tilde{\mathbf{u}},\mathbf{u}} & \mathbf{K}_{\tilde{\mathbf{u}},\tilde{\mathbf{u}}} \end{bmatrix} \tag{B.3}$$

with the matrices defined in Table B.1.

$\mathbf{K}_{\mathbf{u},\mathbf{u}} := \int_{\Omega} \mathbf{B}^T \boldsymbol{C} \mathbf{B} \, \mathrm{d}\Omega$	$\mathbf{K}_{\mathbf{u},\tilde{\mathbf{u}}} := -\int_{\Omega} \mathbf{B}^T \boldsymbol{C} \boldsymbol{\varepsilon} D'(\widetilde{Y}) \frac{\partial \widetilde{Y}}{\partial \widetilde{\boldsymbol{\varepsilon}}} \mathbf{B} \, \mathrm{d}\Omega$
$\mathbf{K}_{\tilde{\mathbf{u}},\mathbf{u}} := -(\mathbf{M} + \ell^2 \mathbf{K}_{\text{BC}})$	$\mathbf{K}_{\tilde{\mathbf{u}},\tilde{\mathbf{u}}} := \mathbf{M} + \ell^2 \mathbf{D}$

Table B.1: Block matrices of the continuous consistent tangent matrix.

Some remarks about the tangent matrix (B.3):

- Matrices $\mathbf{K}_{\mathbf{u},\mathbf{u}}$ and $\mathbf{K}_{\mathbf{u},\tilde{\mathbf{u}}}$ are the secant and the local tangent matrices already obtained by Rodríguez-Ferran et al. (2005).
- Matrices $\mathbf{M}$ and $\mathbf{D}$ are the mass and diffusivity matrices already obtained by Rodríguez-Ferran et al. (2005). They are both constant, due to the linearity of the regularisation equation.
- Matrix $\mathbf{K}_{\text{BC}}$ takes into account the combined boundary conditions and was already obtained by Tamayo-Mas (2013).

Lagrange multipliers are used to prescribe the linear constraints associated to Dirichlet boundary conditions for the local displacement field $\boldsymbol{u}$ and for the smoothed displacement field $\widetilde{\boldsymbol{u}}$. A Newton-Raphson iteration for solving Equations (B.1) for an increment of prescribed displacements and with the corresponding Dirichlet boundary conditions, reads

$$\begin{bmatrix} \mathbf{K}_{\mathbf{u},\mathbf{u}} & \mathbf{K}_{\mathbf{u},\tilde{\mathbf{u}}} & \mathbf{A}_{\text{equi}}^T & \mathbf{0} \\ \mathbf{K}_{\tilde{\mathbf{u}},\mathbf{u}} & \mathbf{K}_{\tilde{\mathbf{u}},\tilde{\mathbf{u}}} & \mathbf{0} & \mathbf{A}_{\text{reg}}^T \\ \mathbf{A}_{\text{equi}} & \mathbf{0} & \mathbf{0} & \mathbf{0} \\ \mathbf{A}_{\text{reg}} & -\mathbf{A}_{\text{reg}} & \mathbf{0} & \mathbf{0} \end{bmatrix} \cdot \begin{bmatrix} \delta\mathbf{u}_c \\ \delta\widetilde{\mathbf{u}}_c \\ \delta\boldsymbol{\lambda}_{\text{equi}} \\ \delta\boldsymbol{\lambda}_{\text{reg}} \end{bmatrix} = \begin{bmatrix} -\mathbf{r}_{\text{equi}} \\ \mathbf{0} \\ \mathbf{0} \\ \mathbf{0} \end{bmatrix} \tag{B.4}$$

where $\mathbf{A}_{\text{equi}}$ and $\mathbf{A}_{\text{reg}}$ represent the Dirichlet boundary conditions for the local displacement field $\boldsymbol{u}$ and for the smoothed displacement field $\widetilde{\boldsymbol{u}}$ respectively. Vectors $\delta\mathbf{u}_c, \delta\widetilde{\mathbf{u}}_c$ are the increments of the local displacements and smoothed displacements respectively, and $\delta\boldsymbol{\lambda}_{\text{equi}}, \delta\boldsymbol{\lambda}_{\text{reg}}$ are the increments of Lagrange multipliers (one per constraint) associated to the Dirichlet Boundary conditions for the local displacement field and the smoothed displacement field, respectively. Vector $\mathbf{r}_{\text{equi}}$ represents the residual forces associated to the weak form of the equilibrium equations of the previous Newton-Raphson iteration.

B.2 Continuous-discontinuous model

Finite element discretisation of the weak form of the equilibrium and regularisation equations, see Equations (A.16) and (A.22), leads to the six discrete weak equations

$$\mathbf{r}_{\text{equi},\mathbf{u}_c}(\mathbf{u},\widetilde{\mathbf{u}}) := \mathbf{f}_{\text{int},\mathbf{u}_c}(\mathbf{u},\widetilde{\mathbf{u}}) - \mathbf{f}_{\text{ext},\mathbf{u}_c} = \mathbf{0} \tag{B.5a}$$

$$\mathbf{r}_{\text{equi},\mathbf{u}_p}(\mathbf{u},\widetilde{\mathbf{u}}) := \mathbf{f}_{\text{int},\mathbf{u}_p}(\mathbf{u},\widetilde{\mathbf{u}}) - \mathbf{f}_{\text{ext},\mathbf{u}_p} = \mathbf{0} \tag{B.5b}$$

$$\mathbf{r}_{\text{equi},\mathbf{u}_s}(\mathbf{u},\widetilde{\mathbf{u}}) := \mathbf{f}_{\text{int},\mathbf{u}_s}(\mathbf{u},\widetilde{\mathbf{u}}) - \mathbf{f}_{\text{ext},\mathbf{u}_s} = \mathbf{0} \tag{B.5c}$$

$$\begin{aligned}\mathbf{r}_{\text{reg},\mathbf{u}_c} &:= -(\mathbf{M}+\ell^2\mathbf{K}_{\text{BC}})\mathbf{u}_c - (\mathbf{M}_{\psi_p}+\ell^2\mathbf{K}_{\psi_p,\text{BC}})\mathbf{u}_p - (\mathbf{M}_{\psi_s}+\ell^2\mathbf{K}_{\psi_s,\text{BC}})\mathbf{u}_s + \\ &+ (\mathbf{M}+\ell^2\mathbf{D})\widetilde{\mathbf{u}}_c + (\mathbf{M}_{\psi_p}+\ell^2\mathbf{D}_{\psi_p})\widetilde{\mathbf{u}}_p + (\mathbf{M}_{\psi_s}+\ell^2\mathbf{D}_{\psi_s})\widetilde{\mathbf{u}}_s = \mathbf{0}\end{aligned} \tag{B.5d}$$

$$\begin{aligned}\mathbf{r}_{\text{reg},\mathbf{u}_p} &:= -(\mathbf{M}_{\psi_p}+\ell^2\mathbf{K}_{\psi_p,\text{BC}})\mathbf{u}_c - (\mathbf{M}+\ell^2\mathbf{K}_{\text{BC}})\mathbf{u}_p - (\mathbf{M}_{\psi_b}+\ell^2\mathbf{K}_{\psi_b,\text{BC}})\mathbf{u}_s + \\ &+ (\mathbf{M}_{\psi_p}+\ell^2\mathbf{D}_{\psi_p})\widetilde{\mathbf{u}}_c + (\mathbf{M}+\ell^2\mathbf{D})\widetilde{\mathbf{u}}_p + (\mathbf{M}_{\psi_b}+\ell^2\mathbf{D}_{\psi_b})\widetilde{\mathbf{u}}_s = \mathbf{0}\end{aligned} \tag{B.5e}$$

$$\begin{aligned}\mathbf{r}_{\text{reg},\mathbf{u}_s} &:= -(\mathbf{M}_{\psi_s}+\ell^2\mathbf{K}_{\psi_s,\text{BC}})\mathbf{u}_c - (\mathbf{M}_{\psi_b}+\ell^2\mathbf{K}_{\psi_b,\text{BC}})\mathbf{u}_p - (\mathbf{M}+\ell^2\mathbf{K}_{\text{BC}})\mathbf{u}_s + \\ &+ (\mathbf{M}_{\psi_s}+\ell^2\mathbf{D}_{\psi_s})\widetilde{\mathbf{u}}_c + (\mathbf{M}_{\psi_b}+\ell^2\mathbf{D}_{\psi_b})\widetilde{\mathbf{u}}_p + (\mathbf{M}+\ell^2\mathbf{D})\widetilde{\mathbf{u}}_s = \mathbf{0}\end{aligned} \tag{B.5f}$$

where $\mathbf{f}_{\text{int},\mathbf{u}_c}$ and $\mathbf{f}_{\text{ext},\mathbf{u}_c}$ are the internal and external forces defined in Equations (B.2a) and (B.2b) respectively, $\mathbf{M}$ is the standard mass matrix, see Equation (B.2c), $\mathbf{D}$ is the standard diffusivity matrix, see Equation (B.2d), and $\mathbf{K}_{\text{BC}}$ is the matrix that takes into account the combined boundary conditions, see Equation (B.2e), whereas the new terms due to the principal and secondary cracks are

$$\mathbf{f}_{\text{int},\mathbf{u}_p} = \int_\Omega \psi_p \mathbf{B}^T \boldsymbol{\sigma} \,\mathrm{d}\Omega + 2\int_{\Gamma_p} \mathbf{N}^T \bar{\boldsymbol{t}}_d \,\mathrm{d}\Gamma \tag{B.6a}$$

$$\mathbf{f}_{\text{int},\mathbf{u}_s} = \int_\Omega \psi_s \mathbf{B}^T \boldsymbol{\sigma} \,\mathrm{d}\Omega + 2\int_{\Gamma_s} \mathbf{N}^T \bar{\boldsymbol{t}}_s \,\mathrm{d}\Gamma \tag{B.6b}$$

$$\mathbf{f}_{\text{ext},\mathbf{u}_p} = \int_{\Gamma_t} \psi_p \mathbf{N}^T \bar{\boldsymbol{t}} \,\mathrm{d}\Gamma \tag{B.6c}$$

$$\mathbf{f}_{\text{ext},\mathbf{u}_s} = \int_{\Gamma_t} \psi_s \mathbf{N}^T \bar{\boldsymbol{t}} \,\mathrm{d}\Gamma \tag{B.6d}$$

$$\mathbf{M}_{\psi_p} = \int_\Omega \psi_p \mathbf{N}^T \mathbf{N} \,\mathrm{d}\Omega \tag{B.6e}$$

$$\mathbf{M}_{\psi_s} = \int_\Omega \psi_s \mathbf{N}^T \mathbf{N} \,\mathrm{d}\Omega \tag{B.6f}$$

$$\mathbf{M}_{\psi_b} = \int_\Omega \psi_b \mathbf{N}^T \mathbf{N} \,\mathrm{d}\Omega \tag{B.6g}$$

$$\mathbf{D}_{\psi_p} = \int_\Omega \psi_p \nabla\mathbf{N}^T \nabla\mathbf{N} \,\mathrm{d}\Omega \tag{B.6h}$$

$$\mathbf{D}_{\psi_s} = \int_\Omega \psi_s \nabla\mathbf{N}^T \nabla\mathbf{N} \,\mathrm{d}\Omega \tag{B.6i}$$

$$\mathbf{D}_{\psi_b} = \int_\Omega \psi_b \nabla\mathbf{N}^T \nabla\mathbf{N} \,\mathrm{d}\Omega \tag{B.6j}$$

$$\mathbf{K}_{\psi_p,\text{BC}} = \int_\Gamma \psi_p \mathbf{N}^T \left(\boldsymbol{\tau}^T \boldsymbol{\tau}\right) \nabla\mathbf{N} \cdot \boldsymbol{n} \,\mathrm{d}\Gamma \tag{B.6k}$$

$$\mathbf{K}_{\psi_s,\text{BC}} = \int_\Gamma \psi_s \mathbf{N}^T \left(\boldsymbol{\tau}^T \boldsymbol{\tau}\right) \nabla\mathbf{N} \cdot \boldsymbol{n} \,\mathrm{d}\Gamma \tag{B.6l}$$

$$\mathbf{K}_{\psi_b,\text{BC}} = \int_\Gamma \psi_b \mathbf{N}^T \left(\boldsymbol{\tau}^T \boldsymbol{\tau}\right) \nabla\mathbf{N} \cdot \boldsymbol{n} \,\mathrm{d}\Gamma \tag{B.6m}$$

Note that if traction-free cracks are considered, as done in Chapters 4 and 5, $\bar{\boldsymbol{t}}_d = \mathbf{0}$ and $\bar{\boldsymbol{t}}_s = \mathbf{0}$, thus leading to $\mathbf{f}_{\text{int},\mathbf{u}_p} = \int_\Omega \psi_p \mathbf{B}^T \boldsymbol{\sigma} \,\mathrm{d}\Omega$ and $\mathbf{f}_{\text{int},\mathbf{u}_s} = \int_\Omega \psi_s \mathbf{B}^T \boldsymbol{\sigma} \,\mathrm{d}\Omega$.

Linearisation of Equations (B.5) results in the tangent matrix

$$\mathbf{K}_{\text{tan}} = \begin{bmatrix} \mathbf{K}_{\mathbf{u}_c,\mathbf{u}_c} & \mathbf{K}_{\mathbf{u}_c,\mathbf{u}_p} & \mathbf{K}_{\mathbf{u}_c,\mathbf{u}_s} & \mathbf{K}_{\mathbf{u}_c,\widetilde{\mathbf{u}}_c} & \mathbf{K}_{\mathbf{u}_c,\widetilde{\mathbf{u}}_p} & \mathbf{K}_{\mathbf{u}_c,\widetilde{\mathbf{u}}_s} \\ \mathbf{K}_{\mathbf{u}_p,\mathbf{u}_c} & \mathbf{K}_{\mathbf{u}_p,\mathbf{u}_p} & \mathbf{K}_{\mathbf{u}_p,\mathbf{u}_s} & \mathbf{K}_{\mathbf{u}_p,\widetilde{\mathbf{u}}_c} & \mathbf{K}_{\mathbf{u}_p,\widetilde{\mathbf{u}}_p} & \mathbf{K}_{\mathbf{u}_p,\widetilde{\mathbf{u}}_s} \\ \mathbf{K}_{\mathbf{u}_s,\mathbf{u}_c} & \mathbf{K}_{\mathbf{u}_s,\mathbf{u}_p} & \mathbf{K}_{\mathbf{u}_s,\mathbf{u}_s} & \mathbf{K}_{\mathbf{u}_s,\widetilde{\mathbf{u}}_c} & \mathbf{K}_{\mathbf{u}_s,\widetilde{\mathbf{u}}_p} & \mathbf{K}_{\mathbf{u}_s,\widetilde{\mathbf{u}}_s} \\ \mathbf{K}_{\widetilde{\mathbf{u}}_c,\mathbf{u}_c} & \mathbf{K}_{\widetilde{\mathbf{u}}_c,\mathbf{u}_p} & \mathbf{K}_{\widetilde{\mathbf{u}}_c,\mathbf{u}_s} & \mathbf{K}_{\widetilde{\mathbf{u}}_c,\widetilde{\mathbf{u}}_c} & \mathbf{K}_{\widetilde{\mathbf{u}}_c,\widetilde{\mathbf{u}}_p} & \mathbf{K}_{\widetilde{\mathbf{u}}_c,\widetilde{\mathbf{u}}_s} \\ \mathbf{K}_{\widetilde{\mathbf{u}}_p,\mathbf{u}_c} & \mathbf{K}_{\widetilde{\mathbf{u}}_p,\mathbf{u}_p} & \mathbf{K}_{\widetilde{\mathbf{u}}_p,\mathbf{u}_s} & \mathbf{K}_{\widetilde{\mathbf{u}}_p,\widetilde{\mathbf{u}}_c} & \mathbf{K}_{\widetilde{\mathbf{u}}_p,\widetilde{\mathbf{u}}_p} & \mathbf{K}_{\widetilde{\mathbf{u}}_p,\widetilde{\mathbf{u}}_s} \\ \mathbf{K}_{\widetilde{\mathbf{u}}_s,\mathbf{u}_c} & \mathbf{K}_{\widetilde{\mathbf{u}}_s,\mathbf{u}_p} & \mathbf{K}_{\widetilde{\mathbf{u}}_s,\mathbf{u}_s} & \mathbf{K}_{\widetilde{\mathbf{u}}_s,\widetilde{\mathbf{u}}_c} & \mathbf{K}_{\widetilde{\mathbf{u}}_s,\widetilde{\mathbf{u}}_p} & \mathbf{K}_{\widetilde{\mathbf{u}}_s,\widetilde{\mathbf{u}}_s} \end{bmatrix} \tag{B.7}$$

with the matrices defined in Table B.2.

Some remarks about the tangent matrix (B.7):

- Matrix $\mathbf{K}_{\mathbf{u}_c,\mathbf{u}_c}$ and the first term in matrix $\mathbf{K}_{\mathbf{u}_p,\mathbf{u}_p}$ and in matrix $\mathbf{K}_{\mathbf{u}_s,\mathbf{u}_s}$ are the secant tangent matrices already obtained in the continuous model. Matrices $\mathbf{K}_{\mathbf{u}_c,\mathbf{u}_p}$, $\mathbf{K}_{\mathbf{u}_p,\mathbf{u}_c}$, $\mathbf{K}_{\mathbf{u}_c,\mathbf{u}_s}$, $\mathbf{K}_{\mathbf{u}_p,\mathbf{u}_s}$, $\mathbf{K}_{\mathbf{u}_s,\mathbf{u}_p}$ and $\mathbf{K}_{\mathbf{u}_s,\mathbf{u}_c}$ may be understood as enriched secant tangent matrices, since the expression is the same, except for the enrichment function.

- Matrices $\mathbf{K}_{\mathbf{u}_c,\widetilde{\mathbf{u}}_c}$, $\mathbf{K}_{\mathbf{u}_p,\widetilde{\mathbf{u}}_p}$ and $\mathbf{K}_{\mathbf{u}_s,\widetilde{\mathbf{u}}_s}$ are the local tangent matrices. Analogously to secant matrix, matrices $\mathbf{K}_{\mathbf{u}_c,\widetilde{\mathbf{u}}_p}$, $\mathbf{K}_{\mathbf{u}_p,\widetilde{\mathbf{u}}_c}$, $\mathbf{K}_{\mathbf{u}_c,\widetilde{\mathbf{u}}_s}$, $\mathbf{K}_{\mathbf{u}_p,\widetilde{\mathbf{u}}_s}$, $\mathbf{K}_{\mathbf{u}_s,\widetilde{\mathbf{u}}_c}$ and $\mathbf{K}_{\mathbf{u}_s,\widetilde{\mathbf{u}}_p}$ can be understood as enriched local tangent matrices.

- Matrices $\mathbf{M}$ and $\mathbf{D}$ are the mass and diffusivity matrices already obtained in the continuous model. They are both constant. Matrices $\mathbf{M}_{\psi_p}$, $\mathbf{M}_{\psi_s}$, $\mathbf{M}_{\psi_b}$, $\mathbf{D}_{\psi_p}$, $\mathbf{D}_{\psi_s}$ and $\mathbf{D}_{\psi_b}$ can be understood as enriched mass and enriched diffusivity matrices.

- Matrices $\mathbf{K}_{\mathrm{BC}}$, $\mathbf{K}_{\psi_p,\mathrm{BC}}$, $\mathbf{K}_{\psi_s,\mathrm{BC}}$ and $\mathbf{K}_{\psi_b,\mathrm{BC}}$ take into account the combined boundary conditions.

- It must be stressed that Equation (4.16) is a compact way to express the finite element approximation of the local and non-local displacements after the introduction of the discontinuity. Indeed, let I denote the set of all nodes in the finite element mesh, J the set of nodes of elements crossed by the principal crack and K the set of nodes of elements crossed by the secondary crack (denoted here as $n_{\text{std.}}$, $n_{\text{enr.p}}$ and $n_{\text{enr.s}}$ respectively). Then, Equation (4.16) can also be expressed as

$$\begin{aligned}\boldsymbol{u}(\boldsymbol{x}) \simeq \boldsymbol{u}^h(\boldsymbol{x}) = \sum_{i\in I} \mathbf{N}_i(\boldsymbol{x})\,\mathbf{u}_i^c \;&+\; \sum_{j\in J} \psi_p(\boldsymbol{x})\,\mathbf{N}_j(\boldsymbol{x})\,\mathbf{u}_j^p + \\ &+\; \sum_{k\in K} \psi_s(\boldsymbol{x})\,\mathbf{N}_k(\boldsymbol{x})\,\mathbf{u}_k^s \qquad \text{(B.8a)}\\ \widetilde{\boldsymbol{u}}(\boldsymbol{x}) \simeq \widetilde{\boldsymbol{u}}^h(\boldsymbol{x}) = \sum_{i\in I} \mathbf{N}_i(\boldsymbol{x})\,\widetilde{\mathbf{u}}_i^c \;&+\; \sum_{j\in J} \psi_p(\boldsymbol{x})\,\mathbf{N}_j(\boldsymbol{x})\,\widetilde{\mathbf{u}}_j^p + \\ &+\; \sum_{k\in K} \psi_s(\boldsymbol{x})\,\mathbf{N}_k(\boldsymbol{x})\,\widetilde{\mathbf{u}}_k^s \qquad \text{(B.8b)}\end{aligned}$$

where ψ_p and ψ_s are sign functions and $\mathbf{N}_i = N_i\mathbf{I}_2$, with N_i the standard bilinear shape function associated with node i and $\mathbf{I}_2$ the identity matrix of size 2. Thus, in Equation (4.16), $\mathbf{N}$ denotes the array that multiplies the standard nodal degrees of freedom $\mathbf{u}_c$ and $\widetilde{\mathbf{u}}_c$ —of dimension $n_{\text{dof}} \times n_{\text{dof}}$, with n_{dof} the number of standard degrees of freedom ($n_{\text{dof}} = 2 \times n_{\text{std.}}$)—, the array that multiplies the enriched nodal degrees of freedom for the principal crack $\mathbf{u}_p$ and $\widetilde{\mathbf{u}}_p$ —of dimension $n_{\text{dof}_p^*} \times n_{\text{dof}_p^*}$, with $n_{\text{dof}_p^*}$ the number of enriched degrees of freedom ($n_{\text{dof}_p^*} = 2 \times n_{\text{enr.p}}$)—and the array that multiplies the enriched nodal degrees of freedom for the secondary crack $\mathbf{u}_s$ and $\widetilde{\mathbf{u}}_s$ —of dimension $n_{\text{dof}_s^*} \times n_{\text{dof}_s^*}$, with $n_{\text{dof}_s^*}$ the number of enriched degrees of freedom ($n_{\text{dof}_s^*} = 2 \times n_{\text{enr.s}}$).

Analogous comments apply for the array $\mathbf{B}$. It denotes both the array that multiplies the standard $\mathbf{u}_c$, $\widetilde{\mathbf{u}}_c$ and the enriched $\mathbf{u}_p$, $\widetilde{\mathbf{u}}_p$, $\mathbf{u}_s$, $\widetilde{\mathbf{u}}_s$ nodal degrees of freedom.

Therefore, due to this abuse of notation, the mass matrix in $\mathbf{K}_{\widetilde{\mathbf{u}}_c,\mathbf{u}_c}$, for instance, has dimension $n_{\text{dof}} \times n_{\text{dof}}$, while the mass matrix in $\mathbf{K}_{\widetilde{\mathbf{u}}_p,\mathbf{u}_p}$ has dimension $n_{\text{dof}_p^*} \times n_{\text{dof}_p^*}$ and the mass matrix in $\mathbf{K}_{\widetilde{\mathbf{u}}_s,\mathbf{u}_s}$ has dimension $n_{\text{dof}_s^*} \times n_{\text{dof}_s^*}$.

- The dimensions of all the enriched matrices change during the numerical simulation, since the number of enriched nodes ($n_{\text{enr.p}}$, $n_{\text{enr.s}}$) varies during the computation. In particular, $\mathbf{M}_{\psi_p}$, $\mathbf{D}_{\psi_p}$, $\mathbf{K}_{\psi_p,\text{BC}}$, $\mathbf{M}_{\psi_s}$, $\mathbf{D}_{\psi_s}$, $\mathbf{K}_{\psi_s,\text{BC}}$, $\mathbf{M}_{\psi_b}$, $\mathbf{D}_{\psi_b}$ and $\mathbf{K}_{\psi_b,\text{BC}}$ are affected by this change of dimensions. Nevertheless, they change only in those steps where the crack propagates.

- As discussed in Appendix A we have used the following three properties: $\psi_p\psi_p = +1$, $\psi_s\psi_s = +1$ and $\psi_p\psi_s = \psi_b$. Due to these properties we can simplify some matrices. Indeed, if we consider the mass matrices of $\mathbf{K}_{\widetilde{\mathbf{u}}_p,\widetilde{\mathbf{u}}_p}$, $\mathbf{K}_{\widetilde{\mathbf{u}}_s,\widetilde{\mathbf{u}}_s}$ and $\mathbf{K}_{\widetilde{\mathbf{u}}_p,\widetilde{\mathbf{u}}_s}$:

$$\int_\Omega \psi_p\mathbf{N}^T\psi_p\mathbf{N}\,\mathrm{d}\Omega = \int_\Omega \mathbf{N}^T\mathbf{N}\,\mathrm{d}\Omega \tag{B.9a}$$

$$\int_\Omega \psi_s\mathbf{N}^T\psi_s\mathbf{N}\,\mathrm{d}\Omega = \int_\Omega \mathbf{N}^T\mathbf{N}\,\mathrm{d}\Omega \tag{B.9b}$$

$$\int_\Omega \psi_s\mathbf{N}^T\psi_p\mathbf{N}\,\mathrm{d}\Omega = \int_\Omega \psi_b\mathbf{N}^T\mathbf{N}\,\mathrm{d}\Omega \tag{B.9c}$$

- Matrix $\mathbf{K}_{\text{cohesion}}$ takes into account the cohesive law of the crack. On the one hand, if traction-free cracks are considered such as done in this thesis,

$\mathbf{K}_{\text{cohesion}} = \mathbf{0}$. On the other hand, if cohesive laws are considered, the traction rate at the discontinuity

$$\dot{\boldsymbol{t}}_p = \mathbf{T}_{\text{p}} [\![\dot{\mathbf{u}}]\!] = \mathbf{T}_{\text{p}} \left(\mathbf{N}\dot{\mathbf{u}}_p\right)_{|\Gamma_p} \tag{B.10a}$$

$$\dot{\boldsymbol{t}}_s = \mathbf{T}_{\text{s}} [\![\dot{\mathbf{u}}]\!] = \mathbf{T}_{\text{s}} \left(\mathbf{N}\dot{\mathbf{u}}_s\right)_{|\Gamma_s} \tag{B.10b}$$

is introduced, where $\mathbf{T}_p$ and $\mathbf{T}_s$ relate traction rate $\dot{\boldsymbol{t}}_p$ and $\dot{\boldsymbol{t}}_s$ and displacement jump rate $[\![\dot{\mathbf{u}}]\!]$. Therefore, if a linear cohesive law is considered,

$$\mathbf{K}_{\text{cohesion,p}} = 2 \int_{\Gamma_p} \mathbf{N}^T \mathbf{T}_{\text{p}} \mathbf{N} \, \mathrm{d}\Gamma \tag{B.11a}$$

$$\mathbf{K}_{\text{cohesion,s}} = 2 \int_{\Gamma_s} \mathbf{N}^T \mathbf{T}_{\text{s}} \mathbf{N} \, \mathrm{d}\Gamma \tag{B.11b}$$

Analogously to the continuous model the Lagrange multipliers technique is used to impose Dirichlet boundary conditions of both equilibrium and regularisation equations. Considering that only the principal crack exists, a Newton-Raphson iteration of the system of equations solved for an increment of applied displacements, is

$$\mathbf{A} \cdot \boldsymbol{x} = \boldsymbol{b} \tag{B.12}$$

with

$$\mathbf{A} = \begin{bmatrix}
\mathbf{K}_{\mathbf{u}_c,\mathbf{u}_c} & \mathbf{K}_{\mathbf{u}_c,\mathbf{u}_p} & \mathbf{K}_{\mathbf{u}_c,\widetilde{\mathbf{u}}_c} & \mathbf{K}_{\mathbf{u}_c,\widetilde{\mathbf{u}}_p} & \mathbf{A}^T_{\text{equi}} & \mathbf{0} & \mathbf{0} & \mathbf{0} \\
\mathbf{K}_{\mathbf{u}_p,\mathbf{u}_c} & \mathbf{K}_{\mathbf{u}_p,\mathbf{u}_p} & \mathbf{K}_{\mathbf{u}_p,\widetilde{\mathbf{u}}_c} & \mathbf{K}_{\mathbf{u}_p,\widetilde{\mathbf{u}}_p} & \mathbf{A}^T_{\text{equi,B}} & \mathbf{0} & \mathbf{0} & \mathbf{0} \\
\mathbf{K}_{\widetilde{\mathbf{u}}_c,\mathbf{u}_c} & \mathbf{K}_{\widetilde{\mathbf{u}}_c,\mathbf{u}_p} & \mathbf{K}_{\widetilde{\mathbf{u}}_c,\widetilde{\mathbf{u}}_c} & \mathbf{K}_{\widetilde{\mathbf{u}}_c,\widetilde{\mathbf{u}}_p} & \mathbf{0} & \mathbf{A}^T_{\text{reg,c}} & \mathbf{A}^T_{\text{regC,c}} & \mathbf{0} \\
\mathbf{K}_{\widetilde{\mathbf{u}}_p,\mathbf{u}_c} & \mathbf{K}_{\widetilde{\mathbf{u}}_p,\mathbf{u}_p} & \mathbf{K}_{\widetilde{\mathbf{u}}_p,\widetilde{\mathbf{u}}_c} & \mathbf{K}_{\widetilde{\mathbf{u}}_p,\widetilde{\mathbf{u}}_p} & \mathbf{0} & \mathbf{A}^T_{\text{reg,p}} & \mathbf{0} & \mathbf{A}^T_{\text{regC,p}} \\
\mathbf{A}_{\text{equi,c}} & \mathbf{A}_{\text{equi,p}} & \mathbf{0} & \mathbf{0} & \mathbf{0} & \mathbf{0} & \mathbf{0} & \mathbf{0} \\
\mathbf{A}_{\text{reg,c}} & \mathbf{A}_{\text{reg,p}} & -\mathbf{A}_{\text{reg}} & -\mathbf{A}_{\text{regD}} & \mathbf{0} & \mathbf{0} & \mathbf{0} & \mathbf{0} \\
\mathbf{A}_{\text{regC,c}} & \mathbf{0} & -\mathbf{A}_{\text{regC,c}} & \mathbf{0} & \mathbf{0} & \mathbf{0} & \mathbf{0} & \mathbf{0} \\
\mathbf{0} & \mathbf{A}_{\text{regC,p}} & \mathbf{0} & -\mathbf{A}_{\text{regC,p}} & \mathbf{0} & \mathbf{0} & \mathbf{0} & \mathbf{0}
\end{bmatrix} \tag{B.13}$$

$$\mathbf{x} = \begin{bmatrix}
\delta\mathbf{u}_c \\ \delta\mathbf{u}_p \\ \delta\widetilde{\mathbf{u}}_c \\ \delta\widetilde{\mathbf{u}}_p \\ \delta\boldsymbol{\lambda}_{\text{equi}} \\ \delta\boldsymbol{\lambda}_{\text{reg}} \\ \delta\boldsymbol{\lambda}_{\text{regC,c}} \\ \delta\boldsymbol{\lambda}_{\text{regC,p}}
\end{bmatrix} \quad \text{and} \quad \mathbf{b} = \begin{bmatrix}
-\mathbf{r}_{\text{equi,c}} \\ -\mathbf{r}_{\text{equi,p}} \\ \mathbf{0} \\ \mathbf{0} \\ \mathbf{0} \\ \mathbf{0} \\ \mathbf{0} \\ \mathbf{0}
\end{bmatrix} \tag{B.14}$$

If two cracks are considered (principal and secondary crack), a Newton-Raphson iteration for solving Equation (B.5f) for an increment of prescribed displacements and with the corresponding Dirichlet boundary conditions, reads as

$$\mathbf{A} = \begin{bmatrix} \mathbf{A}_{11} & \mathbf{A}_{12} \\ \mathbf{A}_{21} & \mathbf{0} \end{bmatrix} \tag{B.15}$$

where $\mathbf{A}_{11} = \mathbf{K}_{\text{tan}}$, Equation (B.7), and

$$\mathbf{A}_{12} = \begin{bmatrix} \mathbf{A}_{\text{equi,c}}^T & \mathbf{0} & \mathbf{0} & \mathbf{0} & \mathbf{0} \\ \mathbf{A}_{\text{equi,p}}^T & \mathbf{0} & \mathbf{0} & \mathbf{0} & \mathbf{0} \\ \mathbf{A}_{\text{equi,s}}^T & \mathbf{0} & \mathbf{0} & \mathbf{0} & \mathbf{0} \\ \mathbf{0} & \mathbf{A}_{\text{reg,c}}^T & \mathbf{A}_{\text{regC,c}}^T & \mathbf{0} & \mathbf{0} \\ \mathbf{0} & \mathbf{A}_{\text{reg,p}}^T & \mathbf{0} & \mathbf{A}_{\text{regC,p}}^T & \mathbf{0} \\ \mathbf{0} & \mathbf{A}_{\text{reg,s}}^T & \mathbf{0} & \mathbf{0} & \mathbf{A}_{\text{regC,s}} \end{bmatrix} \tag{B.16}$$

$$\mathbf{A}_{21} = \begin{bmatrix} \mathbf{A}_{\text{equi,c}} & \mathbf{A}_{\text{equi,p}} & \mathbf{A}_{\text{equi,s}} & \mathbf{0} & \mathbf{0} & \mathbf{0} \\ \mathbf{A}_{\text{reg,c}} & \mathbf{A}_{\text{reg,p}} & \mathbf{A}_{\text{reg,s}} & -\mathbf{A}_{\text{reg,c}} & -\mathbf{A}_{\text{reg,p}} & -\mathbf{A}_{\text{reg,s}} \\ \mathbf{A}_{\text{regC,c}} & \mathbf{0} & \mathbf{0} & -\mathbf{A}_{\text{regC,c}} & \mathbf{0} & \mathbf{0} \\ \mathbf{0} & \mathbf{A}_{\text{regC,p}} & \mathbf{0} & \mathbf{0} & -\mathbf{A}_{\text{regC,p}} & \mathbf{0} \\ \mathbf{0} & \mathbf{0} & \mathbf{A}_{\text{regC,s}} & \mathbf{0} & \mathbf{0} & -\mathbf{A}_{\text{regC,s}} \end{bmatrix} \tag{B.17}$$

$$\mathbf{x} = \begin{bmatrix} \delta\mathbf{u}_c \\ \delta\mathbf{u}_p \\ \delta\mathbf{u}_s \\ \delta\widetilde{\mathbf{u}}_c \\ \delta\widetilde{\mathbf{u}}_p \\ \delta\widetilde{\mathbf{u}}_s \\ \delta\boldsymbol{\lambda}_{\text{equi}} \\ \delta\boldsymbol{\lambda}_{\text{reg}} \\ \delta\boldsymbol{\lambda}_{\text{regC,c}} \\ \delta\boldsymbol{\lambda}_{\text{regC,p}} \\ \delta\boldsymbol{\lambda}_{\text{regC,s}} \end{bmatrix} \quad \text{and} \quad \mathbf{b} = \begin{bmatrix} -\mathbf{r}_{\text{equi,c}} \\ -\mathbf{r}_{\text{equi,p}} \\ -\mathbf{r}_{\text{equi,s}} \\ \mathbf{0} \\ \mathbf{0} \\ \mathbf{0} \\ \mathbf{0} \\ \mathbf{0} \\ \mathbf{0} \\ \mathbf{0} \\ \mathbf{0} \end{bmatrix} \tag{B.18}$$

Some remarks about the system (B.12):

- Lagrange multipliers are used to prescribe the linear constraints associated to Dirichlet boundary conditions for the local displacement field ($\mathbf{u}_c$, $\mathbf{u}_p$ and $\mathbf{u}_s$) and for the smoothed displacement field ($\widetilde{\mathbf{u}}_c$, $\widetilde{\mathbf{u}}_p$ and $\widetilde{\mathbf{u}}_s$).

- Matrices $\boldsymbol{A}_{\text{equi,c}}$, $\boldsymbol{A}_{\text{equi,p}}$ and $\boldsymbol{A}_{\text{equi,s}}$ represent the restrictions imposed by the Dirichlet boundary conditions on the weak form of the equilibrium equations.

- Matrices $\boldsymbol{A}_{\text{reg,c}}$, $\boldsymbol{A}_{\text{reg,p}}$ and $\boldsymbol{A}_{\text{reg,s}}$ represent the restrictions imposed by the Dirichlet boundary conditions on the weak form of the regularisation equations that are applied on the contour of the body, excluding crack surfaces.

- Matrices $\boldsymbol{A}_{\text{regC,c}}$, $\boldsymbol{A}_{\text{regC,p}}$ and $\boldsymbol{A}_{\text{regC,s}}$ represent the restrictions imposed by the Dirichlet boundary conditions on the weak form of the regularisation equations that are applied only on the crack surfaces.

- $\boldsymbol{r}_{\text{equi,c}}$, $\boldsymbol{r}_{\text{equi,p}}$ and $\boldsymbol{r}_{\text{equi,s}}$ are the residual forces associated to the weak form of the equilibrium equations.

- $\boldsymbol{\delta\lambda}_{\text{equi}}$, $\boldsymbol{\delta\lambda}_{\text{reg}}$, $\boldsymbol{\delta\lambda}_{\text{regC,c}}$, $\boldsymbol{\delta\lambda}_{\text{regC,p}}$ and $\boldsymbol{\delta\lambda}_{\text{regC,s}}$ are the increments of Lagrange multipliers (one per constraint).

$\mathbf{K}_{\mathbf{u}_c,\mathbf{u}_c} := \int_\Omega \mathbf{B}^T \boldsymbol{C} \mathbf{B} \, \mathrm{d}\Omega$	$\mathbf{K}_{\mathbf{u}_c,\mathbf{u}_p} := \int_\Omega \psi_p \mathbf{B}^T \boldsymbol{C} \mathbf{B} \, \mathrm{d}\Omega$
$\mathbf{K}_{\mathbf{u}_c,\tilde{\mathbf{u}}_c} := -\int_\Omega \mathbf{B}^T \boldsymbol{C} \boldsymbol{\varepsilon} D'(\widetilde{Y}) \frac{\partial \widetilde{Y}}{\partial \widetilde{\boldsymbol{\varepsilon}}} \mathbf{B} \, \mathrm{d}\Omega$	$\mathbf{K}_{\mathbf{u}_c,\tilde{\mathbf{u}}_p} := -\int_\Omega \psi_p \mathbf{B}^T \boldsymbol{C} \boldsymbol{\varepsilon} D'(\widetilde{Y}) \frac{\partial \widetilde{Y}}{\partial \widetilde{\boldsymbol{\varepsilon}}} \mathbf{B} \, \mathrm{d}\Omega$
$\mathbf{K}_{\mathbf{u}_c,\mathbf{u}_s} := \int_\Omega \psi_s \mathbf{B}^T \boldsymbol{C} \mathbf{B} \, \mathrm{d}\Omega$	$\mathbf{K}_{\mathbf{u}_c,\tilde{\mathbf{u}}_s} := -\int_\Omega \psi_s \mathbf{B}^T \boldsymbol{C} \boldsymbol{\varepsilon} D'(\widetilde{Y}) \frac{\partial \widetilde{Y}}{\partial \widetilde{\boldsymbol{\varepsilon}}} \mathbf{B} \, \mathrm{d}\Omega$
$\mathbf{K}_{\mathbf{u}_p,\mathbf{u}_c} := \int_\Omega \psi_p \mathbf{B}^T \boldsymbol{C} \mathbf{B} \, \mathrm{d}\Omega$	$\mathbf{K}_{\mathbf{u}_p,\mathbf{u}_p} := \int_\Omega \mathbf{B}^T \boldsymbol{C} \mathbf{B} \, \mathrm{d}\Omega + \mathbf{K}_{\mathrm{cohesion},p}$
$\mathbf{K}_{\mathbf{u}_p,\tilde{\mathbf{u}}_c} := -\int_\Omega \psi_p \mathbf{B}^T \boldsymbol{C} \boldsymbol{\varepsilon} D'(\widetilde{Y}) \frac{\partial \widetilde{Y}}{\partial \widetilde{\boldsymbol{\varepsilon}}} \mathbf{B} \, \mathrm{d}\Omega$	$\mathbf{K}_{\mathbf{u}_p,\tilde{\mathbf{u}}_p} := -\int_\Omega \mathbf{B}^T \boldsymbol{C} \boldsymbol{\varepsilon} D'(\widetilde{Y}) \frac{\partial \widetilde{Y}}{\partial \widetilde{\boldsymbol{\varepsilon}}} \mathbf{B} \, \mathrm{d}\Omega$
$\mathbf{K}_{\mathbf{u}_p,\mathbf{u}_s} := \int_\Omega \psi_b \mathbf{B}^T \boldsymbol{C} \mathbf{B} \, \mathrm{d}\Omega$	$\mathbf{K}_{\mathbf{u}_p,\tilde{\mathbf{u}}_s} := -\int_\Omega \psi_b \mathbf{B}^T \boldsymbol{C} \boldsymbol{\varepsilon} D'(\widetilde{Y}) \frac{\partial \widetilde{Y}}{\partial \widetilde{\boldsymbol{\varepsilon}}} \mathbf{B} \, \mathrm{d}\Omega$
$\mathbf{K}_{\mathbf{u}_s,\mathbf{u}_c} := \int_\Omega \psi_s \mathbf{B}^T \boldsymbol{C} \mathbf{B} \, \mathrm{d}\Omega$	$\mathbf{K}_{\mathbf{u}_s,\mathbf{u}_p} := \int_\Omega \psi_b \mathbf{B}^T \boldsymbol{C} \mathbf{B} \, \mathrm{d}\Omega$
$\mathbf{K}_{\mathbf{u}_s,\tilde{\mathbf{u}}_c} := -\int_\Omega \psi_s \mathbf{B}^T \boldsymbol{C} \boldsymbol{\varepsilon} D'(\widetilde{Y}) \frac{\partial \widetilde{Y}}{\partial \widetilde{\boldsymbol{\varepsilon}}} \mathbf{B} \, \mathrm{d}\Omega$	$\mathbf{K}_{\mathbf{u}_s,\tilde{\mathbf{u}}_p} := -\int_\Omega \psi_b \mathbf{B}^T \boldsymbol{C} \boldsymbol{\varepsilon} D'(\widetilde{Y}) \frac{\partial \widetilde{Y}}{\partial \widetilde{\boldsymbol{\varepsilon}}} \mathbf{B} \, \mathrm{d}\Omega$
$\mathbf{K}_{\mathbf{u}_s,\mathbf{u}_s} := \int_\Omega \mathbf{B}^T \boldsymbol{C} \mathbf{B} \, \mathrm{d}\Omega + \mathbf{K}_{\mathrm{cohesion},s}$	$\mathbf{K}_{\mathbf{u}_s,\tilde{\mathbf{u}}_s} := -\int_\Omega \mathbf{B}^T \boldsymbol{C} \boldsymbol{\varepsilon} D'(\widetilde{Y}) \frac{\partial \widetilde{Y}}{\partial \widetilde{\boldsymbol{\varepsilon}}} \mathbf{B} \, \mathrm{d}\Omega$
$\mathbf{K}_{\tilde{\mathbf{u}}_c,\mathbf{u}_c} := -(\mathbf{M} + \ell^2 \mathbf{K}_{\mathrm{BC}})$	$\mathbf{K}_{\tilde{\mathbf{u}}_c,\mathbf{u}_p} := -(\mathbf{M}_{\psi_p} + \ell^2 \mathbf{K}_{\psi_p,\mathrm{BC}})$
$\mathbf{K}_{\tilde{\mathbf{u}}_c,\tilde{\mathbf{u}}_c} := \mathbf{M} + \ell^2 \mathbf{D}$	$\mathbf{K}_{\tilde{\mathbf{u}}_c,\tilde{\mathbf{u}}_p} := \mathbf{M}_{\psi_p} + \ell^2 \mathbf{D}_{\psi_p}$
$\mathbf{K}_{\tilde{\mathbf{u}}_c,\mathbf{u}_s} := -(\mathbf{M}_{\psi_s} + \ell^2 \mathbf{K}_{\psi_s,\mathrm{BC}})$	$\mathbf{K}_{\tilde{\mathbf{u}}_c,\tilde{\mathbf{u}}_s} := \mathbf{M}_{\psi_s} + \ell^2 \mathbf{D}_{\psi_s}$
$\mathbf{K}_{\tilde{\mathbf{u}}_p,\mathbf{u}_c} := -(\mathbf{M}_{\psi_p} + \ell^2 \mathbf{K}_{\psi_p,\mathrm{BC}})$	$\mathbf{K}_{\tilde{\mathbf{u}}_p,\mathbf{u}_p} := -(\mathbf{M} + \ell^2 \mathbf{K}_{\mathrm{BC}})$
$\mathbf{K}_{\tilde{\mathbf{u}}_p,\tilde{\mathbf{u}}_c} := \mathbf{M}_{\psi_p} + \ell^2 \mathbf{D}_{\psi_p}$	$\mathbf{K}_{\tilde{\mathbf{u}}_p,\tilde{\mathbf{u}}_p} := \mathbf{M} + \ell^2 \mathbf{D}$
$\mathbf{K}_{\tilde{\mathbf{u}}_p,\mathbf{u}_s} := -(\mathbf{M}_{\psi_b} + \ell^2 \mathbf{K}_{\psi_b \mathrm{BC}})$	$\mathbf{K}_{\tilde{\mathbf{u}}_p,\tilde{\mathbf{u}}_s} := \mathbf{M}_{\psi_b} + \ell^2 \mathbf{D}_{\psi_b}$
$\mathbf{K}_{\tilde{\mathbf{u}}_s,\mathbf{u}_c} := -(\mathbf{M}_{\psi_s} + \ell^2 \mathbf{K}_{\psi_s,\mathrm{BC}})$	$\mathbf{K}_{\tilde{\mathbf{u}}_s,\mathbf{u}_p} := -(\mathbf{M}_{\psi_b} + \ell^2 \mathbf{K}_{\psi_b,\mathrm{BC}})$
$\mathbf{K}_{\tilde{\mathbf{u}}_s,\mathbf{u}_s} := -(\mathbf{M} + \ell^2 \mathbf{K}_{\mathrm{BC}})$	$\mathbf{K}_{\tilde{\mathbf{u}}_s,\tilde{\mathbf{u}}_c} := \mathbf{M}_{\psi_s} + \ell^2 \mathbf{D}_{\psi_s}$
$\mathbf{K}_{\tilde{\mathbf{u}}_s,\tilde{\mathbf{u}}_p} := \mathbf{M}_{\psi_b} + \ell^2 \mathbf{D}_{\psi_b}$	$\mathbf{K}_{\tilde{\mathbf{u}}_s,\tilde{\mathbf{u}}_s} := \mathbf{M} + \ell^2 \mathbf{D}$

Table B.2: Block matrices of the continuous-discontinuous consistent tangent matrix.

Appendix C

Numerical integration in X-FEM

An important issue when using the X-FEM is the numerical integration of the weak form. In the standard finite element method, the evaluation of the terms of the weak form requires the quadrature of functions that are polynomials, which can be easily accomplished with low order Gauss quadratures. However, these traditional quadrature rules fail to integrate discontinuous functions, leading to inaccuracy and poor convergence. Therefore, for elements crossed by the crack, alternative integration rules should be used. Many approaches can be found in literature, such as high order gauss quadratures or subdomain quadrature, see Belytschko et al. (2009) for a detailed review of these methods. One of these alternative methods, subdomain quadrature, consists of subdividing the cracked element into quadrature subdomains with boundaries aligned with the discontinuity where a fixed order Gauss quadrature is used, see Moës et al. (1999). In this appendix, this integration scheme is reviewed, specifically the two-dimensional scheme for quadrilateral elements. For illustrative purposes, the numerical integration of the mass matrix in cracked quadrilaterals is analysed in detail in Section C.1.1.

C.1 Quadrature in cracked quadrilaterals

Let us assume a quadrilateral element and a set of points Q_i $(i = 1 \dots N)$ belonging to the simplified medial axis of the isoline $D(\boldsymbol{x}) = D^*$, see Figure C.1(a). Applying first the standard bilinear transformation —from the actual geometry to the reference

element— the set of points $P_i = \Phi(Q_i)$ belonging to the bilinear quadrilateral reference element are obtained, see Figure C.1(b). Then the crack is introduced in the element as a straight line. Therefore, the crack introduced in the domain is assumed to be piecewise linear.

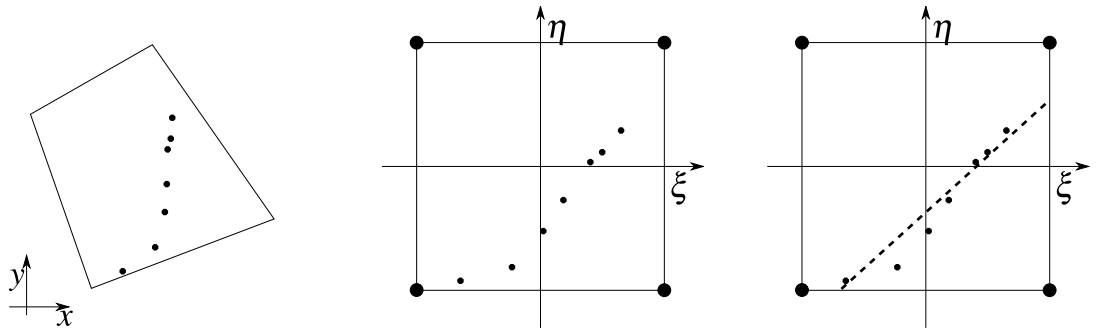

(a) (b) (c)

Figure C.1: (a) The quadrilateral element and the set of points Q_i that belong to the $\theta-$SMA of the isoline $D(\boldsymbol{x}) = D^*$ (b) are mapped to the bilinear reference element. (c) Then, the propagating discontinuity is obtained. Source: Tamayo-Mas (2013).

Once the crack is located in the element, as proposed by Moës et al. (1999), the cracked quadrilateral is decomposed into subelements whose boundaries align with the discontinuity, see Figure C.2(a). In this work, the cracked quadrilateral element is decomposed into two subelements that are further triangulated, see Figure C.2(b). If the quadrilateral element is crossed by two cracks (crack branching element) it is decomposed into three subelements that are further triangulated. Then, each triangular subdomain is mapped to the triangular reference element over which a standard Gauss quadrature is considered, due to the fact that the functions to be integrated are continuous inside the triangles, see Figure C.2(c).

C.1.1 Numerical integration of the mass matrix

As discussed in Appendix B, smoothed displacements are attractive from a computational viewpoint due to the consistent tangent matrix obtained to achieve quadratic convergence in the Newton-Raphson method, see Equation (B.7). Regarding the finite element discretisation of the regularisation equation, the mass and the diffusivity matrices —both the standard and the enriched— need to be exactly computed. In order to verify that the mass matrix is exactly computed the shape functions must

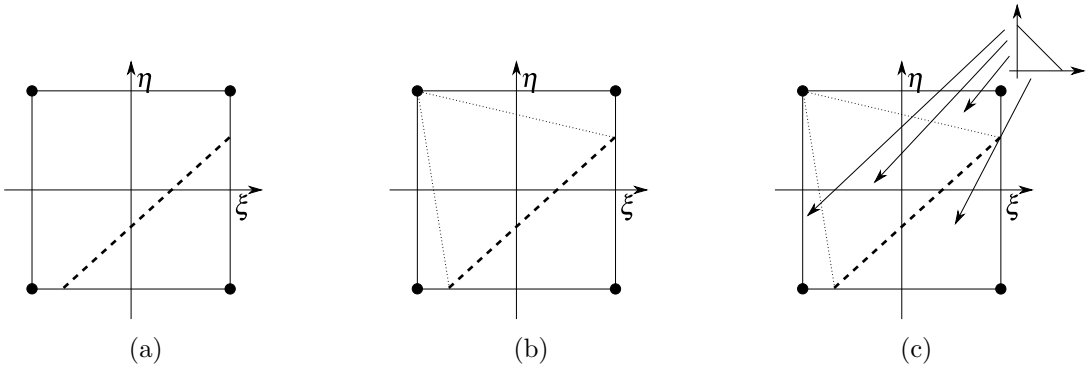

(a) (b) (c)

Figure C.2: (a) The straight crack cuts the reference element into a triangle and a pentagon, (b) which is further divided into triangles. (c) Then, each triangular subdomain is mapped to a parent unit triangle. Source: Tamayo-Mas (2013).

be exactly integrated. If the shape functions are exactly integrated the shape function gradients are also exactly integrated, thus leading to the exact integration of the diffusivity matrix. Hence, the number of Gauss points needed in each triangular subdomain for the exact integration of all the terms in the tangent matrix will be established by the mass matrix. For illustrative purposes, the integration of the mass matrix is analysed in detail.

To compute the mass matrix, we need to integrate

$$I := \int_{\Omega} f(x,y)\,\mathrm{d}x\,\mathrm{d}y \tag{C.1}$$

where $f(x,y) = N_i(x,y)N_j(x,y)$.

Applying the first transformation —from the actual geometry to the reference element— we obtain

$$I := \int_{\Omega} f(x,y)\,\mathrm{d}x\,\mathrm{d}y = \int_{-1}^{1}\int_{-1}^{1} f_*(\xi,\eta)\cdot|J(\xi,\eta)|\,\mathrm{d}\xi\,\mathrm{d}\eta \tag{C.2}$$

where $f_*(\xi,\eta) = f(\Phi_\xi(\xi,\eta),\Phi_\eta(\xi,\eta))$ and J is the determinant of the Jacobian matrix of this first transformation.

Applying the second transformation —from each triangular subdomain to the parent unit triangle— we obtain

$$I := \sum_{i=1}^{\mathrm{S}} g(\hat{\xi},\hat{\eta}) \tag{C.3}$$

where S is the number of triangular subdomains and

$$g(\hat{\xi},\hat{\eta}) = \int_0^1 \int_0^{1-\hat{\eta}} f_{**}(\hat{\xi},\hat{\eta}) \cdot |J(\hat{\Phi}_{\hat{\xi}}(\hat{\xi},\hat{\eta}),\hat{\Phi}_{\hat{\eta}}(\hat{\xi},\hat{\eta}))| \cdot |\hat{J}(\hat{\xi},\hat{\eta})| \,\mathrm{d}\hat{\xi}\,\mathrm{d}\hat{\eta} \tag{C.4}$$

where $f_{**}(\hat{\xi},\hat{\eta}) = f_*(\hat{\Phi}_{\hat{\xi}}(\hat{\xi},\hat{\eta}),\hat{\Phi}_{\hat{\eta}}(\hat{\xi},\hat{\eta}))$ and $\hat{J}$ is the determinant of the Jacobian matrix of the second transformation.

The second transformation is linear and therefore $|\hat{J}(\hat{\xi},\hat{\eta})|$ is a constant. The first transformation is bilinear and thus leading to the following maximum degree of the monomial to be exactly integrated:

$$\begin{array}{rcc} N_i N_j & \rightarrow & \xi^2\eta^2 \\ |J(\xi,\eta)| & \rightarrow & \xi,\eta \\ \hline & & \xi^3\eta^2, \xi^2\eta^3 \end{array}$$

If the monomials of maximum degree to be exactly integrated are $\xi^3\eta^2, \xi^2\eta^3$, a quadrature of degree 5 for triangles is necessary. For instance a quadrature with $N_g = 7$ points may be used.

Bibliography

Bažant, Z. and M. Jirásek (2002). Nonlocal Integral Formulations of Plasticity and Damage: Survey of Progress. *Journal of Engineering Mechanics 128*(11), 1119–1149. doi: 10.1061/(ASCE)0733-9399(2002)128:11(1119).

Belytschko, T. and T. Black (1999). Elastic crack growth in finite elements with minimal remeshing. *International Journal for Numerical Methods in Engineering 45*(5), 601–620. doi: 10.1002/(SICI)1097-0207(19990620)45:5<601::AID-NME598>3.0.CO;2-S.

Belytschko, T., R. Gracie, and G. Ventura (2009). A review of extended/generalized finite element methods for material modeling. *Modelling and Simulation in Materials Science and Engineering 17*(4), 043001. doi: 10.1088/0965-0393/17/4/043001.

Belytschko, T., N. Moës, S. Usui, and C. Parimi (2001). Arbitrary discontinuities in finite elements. *International Journal for Numerical Methods in Engineering 50*, 993–1013. doi: 10.1002/1097-0207(20010210)50:4¡993::AID-NME164¿3.0.CO;2-M.

Bordas, S., T. Rabczuk, and G. Zi (2008). Three-dimensional crack initiation, propagation, branching and junction in non-linear materials by an extended meshfree method without asymptotic enrichment. *Engineering Fracture Mechanics 75*, 943–960. doi: 10.1016/j.engfracmech.2007.05.010.

Daux, C., N. Moës, J. Dolbow, N. Sukumar, and T. Belytschko (2000). Arbitrary branched and intersecting cracks with the extended finite element method. *International Journal for Numerical Methods in Engineering 48*(12), 1741–1760. doi: 10.1002/1097-0207(20000830)48:12<1741::AID-NME956>3.0.CO;2-L.

de Borst, R. and C. V. Verhoosel (2016). Gradient damage vs phase-field approaches for fracture: Similarities and differences. doi: 10.1016/j.cma.2016.05.015.

Duarte, C. A., L. G. Reno, and A. Simone (2007). A high-order generalizedfem for through-the-thickness branched cracks. *International Journal for Numerical Methods in Engineering 72*, 325–351. doi: 10.1002/nme.2012.

Foskey, M., M. C. Lin, and D. Manocha (2003). Efficient computation of a simplified medial axis. In *Proceedings of the eighth ACM symposium on Solid modeling and applications*, SM '03, New York, NY, USA, pp. 96–107. ACM. doi: 10.1145/781606.781623.

Fries, T. P. and T. Belytschko (2010). The extended/generalized finite element method: An overview of the method and its applications. *International Journal for Numerical Methods in Engineering 84*(3), 253–304. doi: 10.1002/nme.2914.

Jirásek, M. (2000). Comparative study on finite elements with embedded discontinuities. *Computer Methods in Applied Mechanics and Engineering 188*(1-3), 307–330. doi: 10.1016/S0045-7825(99)00154-1.

Jirásek, M. and M. Bauer (2012). Numerical aspects of the crack band approach. *Computers and Structures 110–111*, 60–78. doi: 10.1016/j.compstruc.2012.06.006.

Jirásek, M. and T. Zimmermann (2001). Embedded crack model. Part II: combination with smeared cracks. *International Journal for Numerical Methods in Engineering 50*(6), 1291–1305. doi: 10.1002/1097-0207(20010228)50:6<1291::AID-NME12>3.0.CO;2-Q.

Linder, C. and F. Armero (2009). Finite elements with embedded branching. *Finite Elements in Analysis and Design 45*(4), 280–293. doi: 10.1016/j.finel.2008.10.012.

Marji, M. F. (2014). Numerical analysis of quasi-static crack branching in brittle solids by a modified displacement discontinuity method. *International Journal of Solids and Structures 51*, 1716–1736. doi: 10.1016/j.ijsolstr.2014.01.022.

Mazars, J. (1986). A description of micro- and macroscale damage of concrete structures. *Engineering Fracture Mechanics 25*(5–6), 729–737. doi: 10.1016/0013-7944(86)90036-6.

Melenk, J. and I. Babuška (1996). The partition of unity finite element method: Basic theory and applications. *Computational Mehtods in Applied Mechanics and Engineering 139*, 289–314. doi: 10.1016/S0045-7825(96)01087-0.

Moës, N., J. Dolbow, and T. Belytschko (1999). A finite element method for crack growth without remeshing. *International Journal for Numerical Methods in Engineering 46*(1), 131–150. doi: 10.1002/(SICI)1097-0207(19990910)46:1<131::AID-NME726>3.0.CO;2-J.

Mousavi, S. E., E. Grinspun, and N. Sukumar (2011). Higher-order extended finite elements with harmonic enrichment functions for complex crack problems. *International Journal for Numerical Methods in Engineering 86*, 560–574. doi: 10.1002/nme.3098.

Peerlings, R. H. J., M. G. D. Geers, R. de Borst, and W. A. M. Brekelmans (2001). A critical comparison of nonlocal and gradient-enhanced softening continua. *International Journal of Solids and Structures 38*(44–45), 7723–7746. doi: 10.1016/S0020-7683(01)00087-7.

Rabczuk, T., S. Bordas, and G. Zi (2010). On three-dimensional modelling of crack growth using partition of unity methods. *Computers and Structures 88*, 1391–1411. doi: 10.1016/j.compstruc.2008.08.010.

Rodríguez-Ferran, A., I. Morata, and A. Huerta (2005). A new damage model based on non-local displacements. *International Journal for Numerical and Analytical Methods in Geomechanics 29*(5), 473–493. doi: 10.1002/nag.422.

Roth, S., P. Léger, and A. Soulaïmani (2015). A combined xfem-damage mechanics approach for concrete crack propagation. *Computer Methods in Applied Mechanics and Engineering 283*, 923–955. doi: 10.1016/j.cma.2014.10.043.

Sheng, M., S. Shah, A. Lamb, and P. Bordas (2015). Enriched finite elements for branching cracks in deformable porous media. *Engineering Analysis with Boundary Elements 50*, 435–446. doi: 10.1016/j.enganabound.2014.09.010.

Simone, A., G. N. Wells, and L. J. Sluys (2003). From continuous to discontinuous failure in a gradient-enhanced continuum damage model. *Computer Methods in Applied Mechanics and Engineering 192*(41–42), 4581–4607. doi: 10.1016/S0045-7825(03)00428-6.

Strouboulis, T., K. Copps, and I. Babuška (2000). The generalized finite element method: an example of its implementation and illustration of its performance. *International Journal for Numerical Methods in Engineering 47*, 1401–1417. doi: 10.1002/(SICI)1097-0207(20000320)47:8¡1401::AID-NME835¿3.0.CO;2-8.

Sukumar, N., J. E. Dolbow, and N. Moës (2015). Extended finite element method in computational fracture mechanics: a retrospective examination. *International Journal of Fracture 196*, 189–206. doi: 10.1007/s10704-015-0064-8.

Tamayo-Mas, E. (2013). *Continuous-discontinuous modelling for quasi-brittle failure: propagating cracks in a regularised bulk*. Ph. D. thesis, Universitat Politècnica de Catalunya. URL:http://hdl.handle.net/10803/134803.

Tamayo-Mas, E. and A. Rodríguez-Ferran (2012). Condiciones de contorno en modelos de gradiente con desplazamientos suavizados. *Revista Internacional de Métodos Numéricos para Cálculo y Diseño en Ingeniería 28*(3), 170–176. doi: 10.1016/j.rimni.2012.03.006.

Tamayo-Mas, E. and A. Rodríguez-Ferran (2014). A new continuous-discontinuous damage model: Cohesive cracks via an accurate energy-transfer process. *Theoretical and Applied Fracture Mechanics 69*, 90–101. doi: 10.1016/j.tafmec.2013.11.009.

Tamayo-Mas, E. and A. Rodríguez-Ferran (2015). A medial-axis-based model for propagating cracks in a regularised bulk. *International Journal for Numerical Methods in Engineering 101*, 489–520. doi: 10.1002/nme.4757.

Yang, Y. F., G. Li, Z. Z. Liang, and C. A. Tang (2015). Numerical investigation on crack branching during collision for rock-like material. *Theoretical and Applied Fracture Mechanics 76*, 35–49. doi: 10.1016/j.tafmec.2014.12.010.

Zhuang, X., J. Chun, and H. Zhu (2014). A comparative study on unfilled and filled crack propagation for rock-like brittle material. *Theoretical and Applied Fracture Mechanics 72*, 110–120. doi: 10.1016/j.tafmec.2014.04.004.

Zlotnik, S. and P. Díez (2009). Hierarchical X-FEM for n-phase flow (n $>$ 2). *Computer Methods in Applied Mechanics and Engineering 198*(30–32), 2329–2338. doi: 10.1016/j.cma.2009.02.025.